

CARRIER-ENVELOPE PHASE STABILIZATION OF  
GRATING-BASED CHIRPED-PULSE AMPLIFIERS

by

ERIC WAYNE MOON

B.S., Baker University, 2003

AN ABSTRACT OF A DISSERTATION

submitted in partial fulfillment of the requirements for the degree

DOCTOR OF PHILOSOPHY

Department of Physics  
College of Arts and Sciences

KANSAS STATE UNIVERSITY  
Manhattan, Kansas

2009

## Abstract

In this research, the carrier-envelope phase (CE phase) evolution of the pulse train from a Kerr-lens mode-locked chirped-mirror dispersion compensated Ti:Sapphire laser oscillator was stabilized. The offset frequency corresponding to the rate of change of the CE phase was obtained by spectrally broadening the oscillator pulses in a photonic crystal fiber and interfering the  $f$  and  $2f$  components. An offset frequency linewidth of 100 mHz was obtained and could be locked over several hours. The effect of path length drift in the interferometer used for CE phase stabilization of the laser oscillator was investigated. By stabilizing the path length drift, the interferometer noise was reduced by several orders of magnitude.

The CE phase drift through a grating-based chirped-pulse multi-pass amplifier was investigated. Varying the grating separation by  $1\mu\text{m}$  in the stretcher was found to cause a shift of  $3.7 \pm 1.2$  rad of the CE phase. The CE phase could be stabilized to within 160 mrad rms error by feedback controlling the grating separation. By locking the path length in the  $f$ -to- $2f$  interferometer used to stabilize the CE phase of the oscillator pulses, the fast ( $>3$  Hz) CE phase drift of the amplified laser pulses was reduced from 79 to 48 mrad.

It was also found that the CE phase could be shifted and set to any value within a  $2\pi$  range by changing the grating separation. Also, the CE phase could be continuously modulated within a  $2\pi$  range while maintaining a relative phase error of 171 mrad. The CE phase shift of a grating-based compressor was found to be stabilized to 230 mrad rms.

The effect of laser power fluctuation on the CE phase measurement was also investigated. It was found that a 1% fluctuation of the laser energy caused a 160 mrad error in the CE phase measurement. A two-step model is proposed to explain the phase-energy coupling in the CE phase measurement. The model explains the experimentally observed dependence of the group delay between the  $f$  and  $2f$  pulses on the laser energy.

Few-cycle pulses were CE phase stabilized to 134 mrad rms and were used to perform above-threshold ionization and high harmonic generation.

CARRIER-ENVELOPE PHASE STABILIZATION OF  
GRATING-BASED CHIRPED-PULSE AMPLIFIERS

by

ERIC WAYNE MOON

B.S., Baker University, 2003

A DISSERTATION

submitted in partial fulfillment of the requirements for the degree

DOCTOR OF PHILOSOPHY

Department of Physics  
College of Arts and Sciences

KANSAS STATE UNIVERSITY  
Manhattan, Kansas

2009

Approved by:

Major Professor  
Dr. Zenghu Chang

## Abstract

In this research, the carrier-envelope phase (CE phase) evolution of the pulse train from a Kerr-lens mode-locked chirped-mirror dispersion compensated Ti:Sapphire laser oscillator was stabilized. The offset frequency corresponding to the rate of change of the CE phase was obtained by spectrally broadening the oscillator pulses in a photonic crystal fiber and interfering the  $f$  and  $2f$  components. An offset frequency linewidth of 100 mHz was obtained and could be locked over several hours. The effect of path length drift in the interferometer used for CE phase stabilization of the laser oscillator was investigated. By stabilizing the path length drift, the interferometer noise was reduced by several orders of magnitude. This reduced CE phase noise.

The CE phase drift through a grating-based chirped-pulse multi-pass amplifier was investigated. Varying the grating separation by  $1\mu\text{m}$  in the stretcher was found to cause a shift of  $3.7 \pm 1.2$  rad of the CE phase. The CE phase could be stabilized to within 160 mrad rms error by feedback controlling the grating separation. By locking the path length in the  $f$ -to- $2f$  interferometer used to stabilize the CE phase of the oscillator pulses, the fast ( $>3$  Hz) CE phase drift of the amplified laser pulses was reduced from 79 to 48 mrad.

It was also found that the CE phase could be shifted and set to any value within a  $2\pi$  range by changing the grating separation. Also, the CE phase could be continuously modulated within a  $2\pi$  range while maintaining a relative phase error of 171 mrad. The CE phase shift of a grating-based compressor was found to be stabilized to 230 mrad rms.

The effect of laser power fluctuation on the CE phase measurement was also investigated. It was found that a 1% fluctuation of the laser energy caused a 160 mrad error in the CE phase measurement. A two-step model is proposed to explain the phase-energy coupling in the CE phase measurement. The model explains the experimentally observed dependence of the group delay between the  $f$  and  $2f$  pulses on the laser energy.

Few-cycle pulses were CE phase stabilized to 134 mrad rms and were used to perform above-threshold ionization and high harmonic generation.

## Table of Contents

List of Figures .....	vii
List of Tables .....	xii
Acknowledgements .....	xiii
Dedication .....	xiv
CHAPTER 1 - Introduction .....	1
CHAPTER 2 - CE Phase and the CE Phase Offset Frequency.....	4
2.1 Definition of CE Phase .....	4
2.2 Origin of the CE Phase in Ti:Sapphire Laser Oscillators .....	7
2.2a Mode-Locking and Cavity Modes .....	7
2.2b CE Phase Offset Frequency .....	11
2.3 Stabilization of the CE Phase.....	17
2.3a Review of the Technology .....	17
2.3b f-to-2f Self-Referencing.....	18
2.3c Locking the Offset Frequency.....	19
CHAPTER 3 - Stabilization of the CE Phase of the KLSI Oscillator.....	21
3.1 The KLSI Laser Oscillator.....	21
3.2 Self-Referencing Setup.....	24
3.2a PCF Setup.....	24
3.2b Spectral Broadening with the PCF.....	25
3.2c f-to-2f Setup .....	27
3.3 Phase-Locking Loop.....	32
3.4 Results and Discussion .....	37
3.5 Noise of the Oscillator CE Phase Locking Interferometer .....	43
CHAPTER 4 - CE Phase Stabilization of Amplified Laser Pulses .....	49
4.1 Background.....	49
4.2 Experimental Methods.....	50
4.2a Chirped-Pulse Amplification .....	50
4.2b CE Phase and Few-Cycle Pulses.....	52

4.2c $f$ -to- $2f$ Spectral Interferometry .....	54
CHAPTER 5 - Stabilization and Control of the CE Phase using the KLS Amplifier .....	60
5.1 The KLS Amplifier .....	60
5.2 Measurement of the CE Phase Drift .....	63
5.3 Previous Work .....	67
5.4 Grating Control Feedback Method .....	68
5.5 Stabilization of the CE Phase Drift .....	71
5.6 Control of the Relative CEP .....	77
5.7 Path Length Drift Stabilization and CE Phase Stability .....	83
5.8 CE Phase Stabilization using the Compressor Gratings in the KLSII Amplifier .....	84
CHAPTER 6 - Amplifier Power Stability and $f$ -to- $2f$ Measurement Error .....	90
6.1 Out-loop $f$ -to- $2f$ .....	90
6.2 Power Locking and In-loop and Out-loop Measurements .....	90
6.3 Phase-Energy Coupling .....	92
6.4 Coupling Mechanism .....	96
CHAPTER 7 - Few-Cycle Pulses and CE Phase .....	100
7.1 CE Phase Measurement using Few-Cycle Pulses .....	100
7.2 Measurement of CE Phase Error from the Fiber .....	105
CHAPTER 8 - Applications .....	107
8.1 Stereo-Above-Threshold Ionization Detection of the CE Phase .....	107
8.2 XUV Attosecond Pulses .....	109
CHAPTER 9 - Conclusions .....	111
References .....	113
Appendix A - Code for Stabilizing the Amplifier CE Phase .....	119

## List of Figures

Figure 2.1 Laser pulse displaying the CE Phase: Electric field (solid curve) and Pulse Envelope (dashed curve).....	4
Figure 2.2 Four pulses with different CE phase values.....	5
Figure 2.3 Electric fields in the time domain of a few-cycle and multi-cycle pulse: a) 7 fs pulse, b) 20 fs pulse.....	6
Figure 2.4 Laser Cavity: OC: output coupler.....	8
Figure 2.5 Cavity modes.....	9
Figure 2.6 Mode structure and laser gain spectrum. The dashed arrow represents a large increase in frequency in order to show DC on the same scale.....	9
Figure 2.7 Theoretical plot for the CE phase shift through fused silica at 800 nm central wavelength.....	14
Figure 2.8 Shifted frequency comb. The dashed arrow represents a large increase in frequency in order to show DC on the same axis.....	16
Figure 2.9 $f$ -to- $2f$ self-referencing.....	18
Figure 3.1 The KLSI Laser Oscillator. M1-M8: cavity mirrors, AOM: acousto-optic modulator, OC: output coupler, CP: compensating plate.....	21
Figure 3.2 Kansas Light Source Oscillator Spectrum.....	23
Figure 3.3 PCF setup for spectral broadening.....	25
Figure 3.4 PCF output spectra: a) low wavelength portion of the spectrum, b) spectrum measured with a $>700$ nm filter.....	26
Figure 3.5 PCF output at lower power: a) 6 mW output power, b) 18 mW output power.....	27
Figure 3.6 $f$ -to- $2f$ Interferometer for self-referencing; $\lambda/2$ : half-waveplate, AL: aspheric lens, PCF: photonic crystal fiber, MO: microscope objective, DBS: dichroic beamsplitter, L: lens, PPKTP: periodically-poled KTP, PBS: polarizing beamsplitter cube, F: filter, S: slit, APD: avalanche photodiode.....	28
Figure 3.7 Reflected and transmitted spectra from the dichroic beamsplitter: a) reflected spectrum, b) transmitted spectrum.....	29

Figure 3.8 Spectrum focused into the APD. ....	31
Figure 3.9 Signal obtained from the $f$ -to- $2f$ interferometer.....	32
Figure 3.10 Phase-locking system. ....	33
Figure 3.11 Schematic of the phase-locking loop.....	34
Figure 3.12 Phase detector output.....	35
Figure 3.13 PI controller circuit diagram.....	36
Figure 3.14 AOM, $\theta_B$ : Bragg angle .....	37
Figure 3.15 Linewidth of the offset frequency when the phase-locking loop was engaged.....	37
Figure 3.16 Offset frequency amplitude vs. time. ....	39
Figure 3.17 a) AOM control voltage, b) Phase detector output.....	40
Figure 3.18 Phase detector output stability.....	41
Figure 3.19 PSD of the phase detector signal (black curve) and integrated phase error (blue curve). ....	42
Figure 3.20 $f$ -to- $2f$ with a HeNe laser. CL: cylindrical-lens, PD: photodiode, CCD: camera. ....	45
Figure 3.21 HeNe fringes. Left) unlocked, Right) locked. ....	45
Figure 3.22 Top) The power spectrum of the interferometer phase noise and the integrated phase error. Bottom) Comparison of phase noise measurements when the optical table was floated and unfloatd.....	47
Figure 4.1 CPA laser system.....	51
Figure 4.2 Laser system for generating high-intensity, few-cycle, CE phase stable pulses. ....	53
Figure 4.3 $f$ -to- $2f$ interferometry for the amplified laser pulses.....	55
Figure 4.4 Spectral interferometry signal. ....	56
Figure 4.5 Example of an experimental interferogram. ....	56
Figure 4.6 FFT Peak from the spectral interferometry signal.....	57
Figure 4.7 FTSI Schematic .....	58
Figure 5.1 KLS Amplifier: BS: beamsplitter, AOM: acousto-optic modulator, PC: Pockel's cell, FM: focusing mirror, PZT: piezo-electronic transducer, G: grating.....	60
Figure 5.2 Spectrum of the amplified pulses. ....	61
Figure 5.3 KLS laser timing. ....	62
Figure 5.4 $f$ -to- $2f$ for measuring CE phase drift: NDF: neutral density filter, SP: sapphire plate, BBO: SHG-crystal, P: polarizer, $\tau$ : delay.....	63



Figure 5.5 Spectrum from the sapphire-plate at different energies. ....	64
Figure 5.6 1 ms integration time interference fringes.....	66
Figure 5.7 50 ms integration time interference fringes.....	66
Figure 5.8 100 ms integration time interference fringes.....	67
Figure 5.9 Material-based CPA with CE phase drift feedback to the oscillator locking electronics. ....	68
Figure 5.10 Grating-based stretchers for CE phase stabilization of the amplified laser pulses: $\gamma_s$ : angle of incidence, $\theta_s$ : angle between the incident and diffracted rays, $l_{eff}$ : effective grating separation, $f$ : focal length, FM1 and FM2 are the focusing mirrors, M is a retroreflecting mirror, PZT: piezoelectronic transducer, $G_s$ : perpendicular distance between the gratings, G1 and G2 are the gratings, G1': image of G1, $l$ : is the distance between the gratings.....	69
Figure 5.11 KLS with CE Phase drift stabilization and measurement.....	71
Figure 5.12 Effect of changing the grating separation on the CE phase drift: a) 60 V <sub>p-p</sub> voltage applied, b) DC voltage applied. ....	72
Figure 5.13 Measured CE phase drift when the feedback control was disengaged.....	73
Figure 5.14 Feedback control engaged. ....	74
Figure 5.15 Stabilized CE phase drift. ....	75
Figure 5.16 a) temporal evolution of the relative CE phase. A, B, and C represent the three kinds of error spikes. b) the relative CE phase and the displacement of the PZT in the first 32 minutes in a).....	76
Figure 5.17 Precisely controlling the CE phase of the amplified laser pulses. Top, the temporal evolution of the interference fringes. Bottom, the effect of changing the locking set-point on the measured relative CE phase. ....	78
Figure 5.18 a) The error signal for the slow feedback stabilization, b) the displacement of the PZT when the set-point was shifted.....	79
Figure 5.19 Top, temporal evolution of the interference fringes. Bottom, swept relative CE phase vs. time.....	80
Figure 5.20 Top, CE phase error during the modulation. Bottom, displacement of the PZT.....	81
Figure 5.21 Long-term sweeping stability.....	82

Figure 5.22 a) The relative CE phase measured by the collinear f-to-2f interferometer. b) The fast jitter of the CE phase obtained by applying a high-pass filter to the spectra in a).....	83
Figure 5.23 Experimental setup for controlling the CE phase of the amplified laser pulses. PC: Pockels cell, BS: beamsplitter.....	85
Figure 5.24 Configuration of a double-pass grating compressor. G: grating separation, d: grating constant, $\beta$ : diffraction angle, M: retro-reflection mirror.....	86
Figure 5.25 The frequency response of the PZT mounted grating. ....	87
Figure 5.26 The frequency response of the retrieved CE phase shift when the PZT was driven at different frequencies. ....	88
Figure 5.27 a) The evolution of the free drifted (dotted line) and stabilized (solid line) CE phase drift. b) The fast Fourier transform of the CE phase drift under the free running (dotted line) and stabilized conditions (solid line). ....	89
Figure 6.1. Out-loop <i>f-to-2f</i> .....	90
Figure 6.2 Power locked. a) Out-loop measured CE phase, b) In-loop measured CE phase. ....	91
Figure 6.3 Power unlocked. a) Out-loop measured CE phase, b) In-loop measured CE phase. .	92
Figure 6.4 Setup for measuring the CE phase-energy coupling coefficient. ....	93
Figure 6.5 Temporal evolution of the measured phase and laser energy. a) Modulated in-loop pulse energy, b) measured out-loop phase, c) the in-loop phase and out-loop pulse energy.	94
Figure 6.6 Retrieved experimental results versus the laser energy. a) Relative CE phase, b) delay time, c) the residual intercept after the subtraction of the CE phase.....	95
Figure 7.1 Setup for Measuring CE phase stability of few-cycle pulses. ....	100
Figure 7.2 Top: Input and output spectra. Bottom: Measured pulse duration. ....	101
Figure 7.3 a) CE phase fringes and phase drift of the pulses before the fiber. b) CE phase fringes and phase drift of the pulses after the fiber. The power was locked to 0.6% before the fiber. ....	102
Figure 7.4 a) CE phase fringes and phase drift of the pulses before the fiber. b) CE phase fringes and phase drift of the pulses after the fiber. The power stability was 1.5% before the fiber. ....	103
Figure 7.5 a) CE phase fringes and phase drift of the pulses before the fiber. b) CE phase fringes and phase drift of the pulses after the fiber. The power stability was 0.6% before the fiber. ....	104

Figure 8.1 Experimental setup for determining the CE phase of few-cycle pulses.....	107
Figure 8.2 Left) CE phase drift before the hollow-core fiber. Right) Phase meter results.....	108
Figure 8.3 Effects of CE phase on HHG spectra obtained using DOG. ....	109
Figure A.1 Front Panel. 1) The fringe pattern, 2) the FFT peak obtained from the fringe pattern, 3) the range of integration of the fringe pattern and the integration time.....	119
Figure A.2 Code for obtaining the FFT peak.....	120
Figure A.3 Sub VI for calculating the unwrapped CE phase.....	121
Figure A.4 CE Phase code schematic. ....	121

## List of Tables

Table 5-1 Comparison of the set-point, average relative CE phase, and corresponding standard deviation of the CE phase error.....	79
---	----

## **Acknowledgements**

I would like to acknowledge several people in this section for their help, patience, and friendship.

I am indebted to my advisor, Dr. Zenghu Chang, for giving me the opportunity to study ultrafast science and for his aid in starting my career as a scientist. This research would not have been possible without his comments, encouragement, and assistance in and out of the lab. I will be forever proud and grateful to have had the opportunity to be his student.

I would like to thank my committee members: Dr. Larry Weaver, Dr. Brett Esry, Dr. Itzik Ben-Itzhak, and Dr. Shuting Lei for their helpful comments, time, and patience during this research. I would also like to thank Dr. Anil Pahwa for serving as my committee chairperson.

I would like to thank the JRML staff and faculty for help in the lab and out of the lab. I would especially like to thank Al Rankin for helping with the CE phase setup and Vince Needham for assisting with computers.

And especially, thank you to all current and former KLS members. I would like to give a HUGE thanks to Chengquan Li for his help and expertise in pursuing this CE phase project.

## **Dedication**

I would like to thank my family and friends for all your support and patience during this research. And especially, I dedicate this to Cristina Williams. Thank you for your love and support.

## CHAPTER 1 - Introduction

As the width of a laser pulse approaches few or single cycles in duration, the electric field amplitude changes rapidly within half of the cycle. The fast variation of the electric field within the pulse envelope is the origin of carrier-envelope (CE) phase effects in a variety of high field processes such as above-threshold ionization (ATI) and high order harmonic generation (HHG) [1, 2]. The CE phase can affect the high order harmonic generation process even when the excitation laser is long. [3]

Other processes are susceptible to the CE phase. For example, CE phase effects have been predicted in the dissociation of molecules [4] and in electron emission from metal surfaces. [5] CE phase even played a role in terahertz-emission spectroscopy with few-cycle pulses. [6] Advances in CE phase control have allowed researchers access to controlling such processes as injected photocurrents in semiconductors [7] and in sub-single-cycle pulse trains generated with Raman sidebands. [8]

The repetition rate of femtosecond oscillators is on the order of 80 MHz, which is set by the cavity length. The spacing of the pulse train is  $\sim 12$  ns, which matches the opening time of most Pockels cell pulse pickers. Chirped pulse amplifiers run at kilohertz or even lower repetition rates. Currently, commercially available Ti:Sapphire laser oscillators can produce  $<10$  fs pulses. [9] The durations of amplified laser pulses are around 30 fs, due to gain narrowing, which can be shortened to  $\sim 5$  fs in hollow-core fiber /chirped-mirror compressors [10-12] or filamentation setups. [13,14] Also, adaptive phase modulation in conjunction with spectral broadening in a hollow-core fiber filled with neon gas has been shown to produce high power two-cycle pulses. [15]

In order to study processes susceptible to the CE phase, the CE phase of the laser oscillator must be locked and any CE phase drift through the amplification process must be corrected. Furthermore, the CE phase drift during the nonlinear spectral broadening followed by pulse compression must be corrected. The stabilization of the laser oscillator CE phase and the measurement of the phase drift of the amplified laser pulses is well-established. [16] However, those systems employed material-based stretchers and compressors which could not be scaled up to several mJ in energy. The CE phase stabilization of the amplifiers was accomplished by feeding back to the oscillator locking electronics, which added extra stress to the CE phase stabilization. The effects of power fluctuation on the CE phase measurement of the amplified laser pulses had not been fully investigated. [16] Finally, no CE phase effects in strong field atomic physics studies had been researched using CE phase stabilized grating-based chirped pulse amplifiers (CPA).

In this work, those issues were addressed. The CE phase of the Ti:Sapphire laser oscillator used to seed a grating-based CPA laser system was stabilized. The effects of path length drift, which previously had not been addressed, in the  $f$ -to- $2f$  used to detect the offset frequency for CE phase stabilization were studied. Path length drift was found to impart extra CE phase noise on the pulses leaving the laser oscillator. [17]

The CE phase stable pulses were amplified to several mJ in the CPA and the CE phase drift was corrected by changing the stretcher grating separation. [18] This separated the oscillator CE phase stabilization and the amplifier CE phase stabilization which increased the time over which the oscillator could be locked. In a second CPA laser, the compressor grating separation was used to correct the CE phase drift. [19] This work showed that either the stretcher or compressor could be used to stabilize the CE phase drift.



The measurement of the CE phase drift of the amplified laser pulses was found to be susceptible to energy fluctuation. [20] Previously, the power fluctuation issue had only been partially investigated. [16] A two-step model was proposed for explaining the coupling between the laser energy and CE phase. [21] Furthermore, the CE phase drift of few-cycle pulses obtained from a hollow-core fiber chirped-mirror compressor was stabilized. The nonlinear interaction in the fiber for spectral broadening was found to be susceptible to energy fluctuations. [11] Previous work had not addressed this issue.

The CE phase stabilized pulses from the grating-based CPA were used to perform stereo above-threshold ionization [18] and high-harmonic generation. [22] The results indicated the high CE phase stability of the laser system.

## CHAPTER 2 - CE Phase and the CE Phase Offset Frequency

### 2.1 Definition of CE Phase

The electric field of a transform limited laser pulse at a fixed point in space can be mathematically represented as  $E(t) = E_0(t) \cos(\omega_c t + \phi_{CE})$ , where  $E_0(t)$  is the temporal pulse amplitude,  $\omega_c$  is the carrier-frequency, and  $\phi_{CE}$  is the CE phase. The CE phase, or absolute phase, of the laser pulse denotes the offset between the peak of the electric field oscillation with respect to the pulse envelope at  $t = 0$ . The situation is depicted in Figure 2.1.

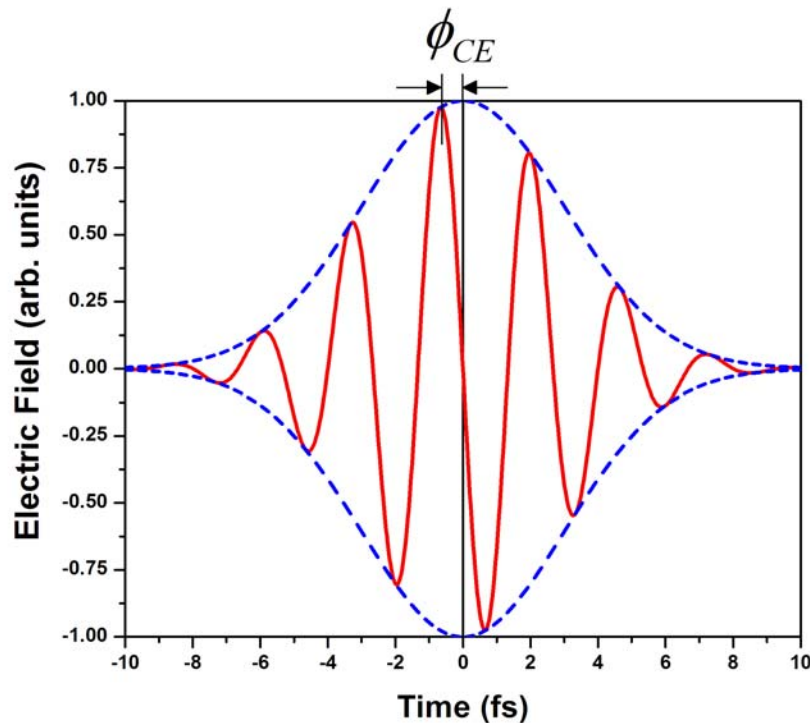


**Figure 2.1 Laser pulse displaying the CE Phase: Electric field (solid curve) and Pulse Envelope (dashed curve).**

In Figure 2.1, the peak of the carrier-wave oscillation is offset from the peak of the pulse envelope. For this particular pulse, the CE phase was  $\pi/2$ . Also, the figure was created by assuming a Gaussian pulse envelope and is 5 fs in duration.

To further demonstrate the CE phase, four pulses whose CE phase values change by  $\pi/2$  are shown in Figure 2.

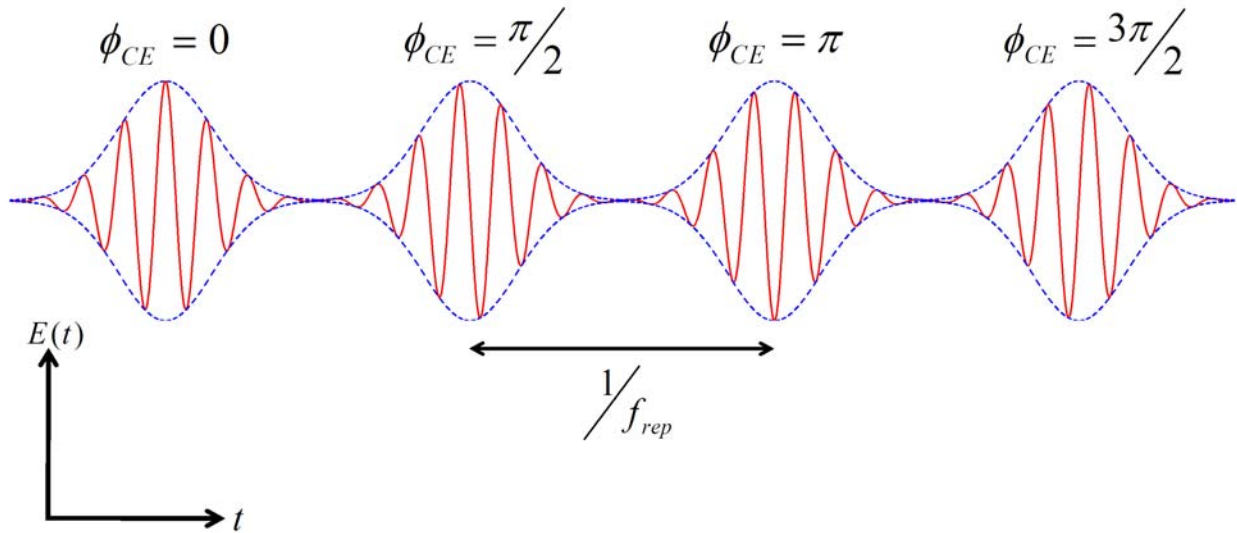


**Figure 2.2 Four pulses with different CE phase values.**

The above figure shows the electric field plotted as a function of time for a laser pulse train with a varying CE phase. The pulses in Figure 2.2 are similar to the pulse train that would be emitted by a CE phase stabilized Ti:Sapphire laser oscillator. In the figure,  $f_{rep}$  is the repetition rate of the pulse train (pulses/second) and the inverse of that value is the time between pulses. If you view the electric field peak in the first pulse ( $\phi_{CE} = 0$ ) as the phase is changed from 0 to  $3\pi/2$  in  $\pi/2$  steps, the electric field appears to advance towards the leading edge of the pulse. The field can be thought of “slipping” through the leading edge as the CE phase increases in value.

Researchers in the ultrafast field often refer to pulses with  $\phi_{CE} = 0$  as “cosine-like” and pulses with  $\phi_{CE} = 3\pi/2$  as “sine-like.” [1] The intermediate CE phase values are also important. In Figures 2.1 and 2.2, the pulses used for demonstration of the CE phase were only a few-cycles of oscillation of the carrier-wave in duration in order to allow the CE phase shift to be clearly seen. However, as the laser pulse duration increases, many cycles of the carrier-wave occur underneath the pulse envelope. The cycle time of the carrier-wave is calculated as  $T_{cycle} = 2\pi/\omega_c$ . For a Ti:Sapphire laser with an 800 nm central wavelength, the cycle time is 2.67 fs. A few-cycle pulse and a multi-cycle pulse are shown in Figure 2.3.

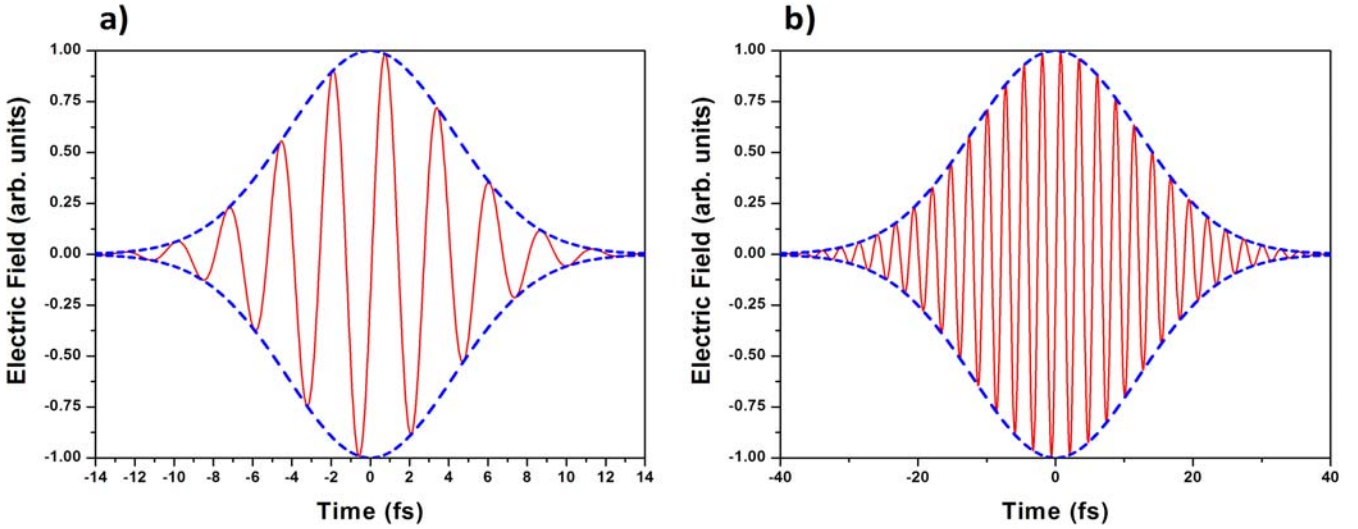


**Figure 2.3 Electric fields in the time domain of a few-cycle and multi-cycle pulse: a) 7 fs pulse, b) 20 fs pulse**

In the figure, the pulse on the left is 7 fs in duration and the pulse on the right is 20 fs in duration. The pulses were given a CE phase value of  $3\pi/2$ . For the 7 fs pulse,  $\sim 2.5$  oscillations of the electric field occur near the envelope maximum. Alternately, for the 20 fs pulse,  $\sim 7.4$  oscillations of the field occur near the envelope maximum. As can be seen from the figure, the difference in amplitude between adjacent electric field peaks near the envelope maximum is shown to decrease as the laser pulse duration increases. In the simulation for the 20 fs pulse, the

ratio between the highest electric field peak and the adjacent peak was  $\sim 0.98$ . For the 7 fs pulse, the ratio was  $\sim 0.90$ . The ratio will be different, though, for other values of the CE phase.

Thus, no matter how long a pulse is, one peak of the carrier-wave is always higher in amplitude than the adjacent peaks near the envelope maximum. The CE phase can always be defined. However, even though the CE phase can be defined for a laser pulse composed of a large number of cycles of oscillation of the carrier-wave, it becomes irrelevant for time-domain applications since the difference in electric field peak amplitudes becomes very small. The pulse-to-pulse CE phase shift, though, is important in the frequency domain, due to the frequency comb property of a mode-locked laser, even if the laser pulse is long and will be discussed in the next section.

## **2.2 Origin of the CE Phase in Ti:Sapphire Laser Oscillators**

### ***2.2a Mode-Locking and Cavity Modes***

Mode-locked Ti:Sapphire lasers provide periodic trains of laser pulses with durations on the femtosecond level. Laser oscillators producing 6 fs pulses even exist. [9] The CE phase is a direct consequence of the mode-locking process as it is the interplay between the laser pulses and the dispersion in the cavity which lead to the CE phase. Mode-locking is the process by which the longitudinal modes of the laser cavity oscillate in phase, interfering constructively and destructively along the longitudinal axis. This leads to the production of a regular train of pulses whose properties depend on the number of modes locked in phase, laser cavity length, dispersion, and gain bandwidth of the laser crystal. In this section, a brief theory of mode-locking in Ti:Sapphire lasers is discussed. [23]

A typical Ti:Sapphire laser cavity is shown in Figure 2.4. The cavity consists of a laser crystal, focusing mirrors, and a highly reflective output coupler. The pump is focused into the laser crystal to create a population inversion, which starts the lasing process.

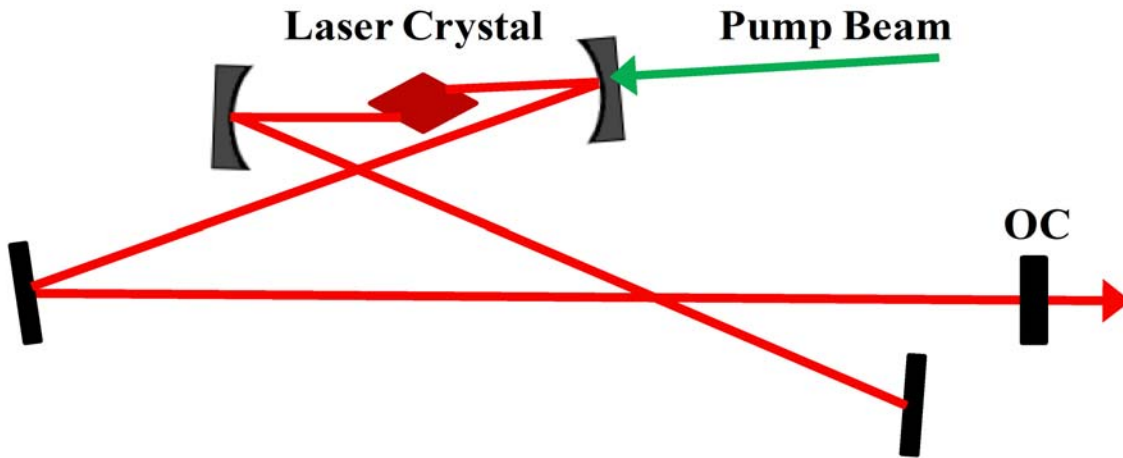


**Figure 2.4 Laser Cavity: OC: output coupler**

The cavity, though, can only support integer multiples of the cavity frequencies, which is a consequence of electromagnetic theory. By solving Maxwell's equations in the cavity, the cavity modes are given by  $f_m = mc/2nL$ , where  $c$  is the speed of light,  $n$  is the average index of refraction of the cavity,  $L$  is the cavity length, and  $m$  is the mode index. The quantity  $nL$  represents the total optical path length through the cavity. For the sake of this section, the index of refraction is assumed to be constant across the laser gain bandwidth. The case of dispersion, which gives the CE phase, will be discussed in the next section. The difference between two modes is given by:

$$f_{m+1} - f_m = c/2nL \quad (2.1)$$

The quantity  $2nL/c$  gives the time for a pulse to traverse the cavity. The inverse of that quantity is then the repetition rate,  $f_{rep}$  of the laser. [23]

Since the modes are evenly spaced, a regular comb of lines arises in the frequency domain. This kind of structure is called a frequency comb. The situation is shown in Figure 2.5.

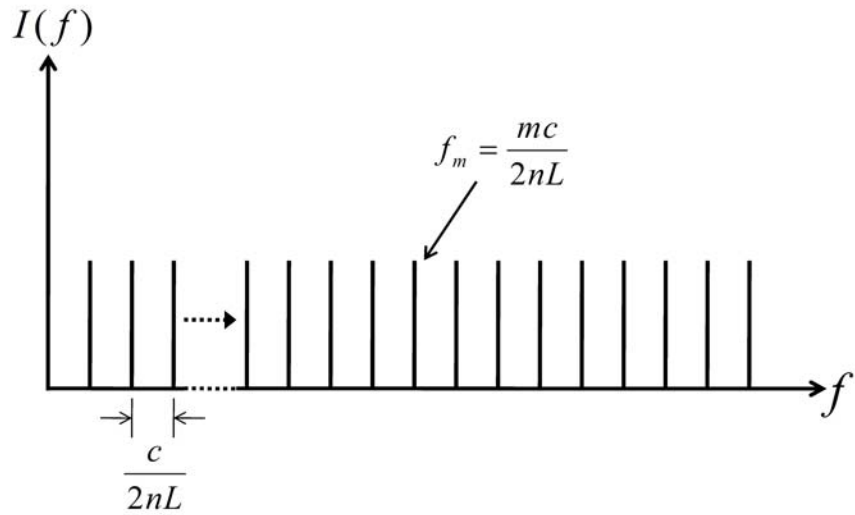


**Figure 2.5 Cavity modes**

For most mode-locked lasers, the spacing between the modes is usually tens of MHz up to GHz. The width of the modes is given by the cavity finesse. [24]

However, when lasing occurs, only the modes underneath the gain spectrum of the laser crystal will be excited. The emitted radiation does not extend to all possible frequencies supported by the cavity. For optical frequencies, the mode index  $m$  is on the order of  $10^6$ . For Ti:Sapphire, the gain bandwidth is  $\sim 120$  THz ( $10^{12}$  Hz). [25]

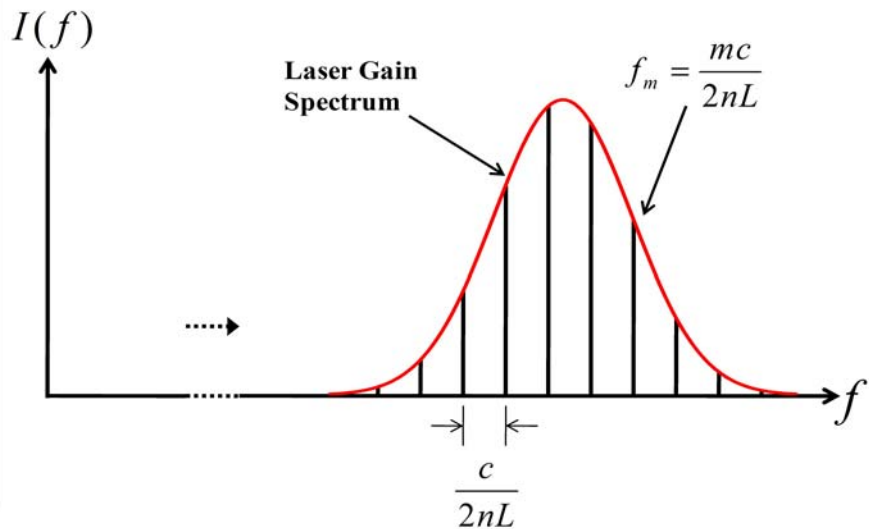


**Figure 2.6 Mode structure and laser gain spectrum. The dashed arrow represents a large increase in frequency in order to show DC on the same scale.**

The large numbers of modes excited when the laser crystal is pumped do not necessarily oscillate in phase. Also, the excited modes do not all have the same amplitude. In this case, the oscillations average out in the time domain, leading to a continuous-mode (CW). For Ti:Sapphire, the CW mode is an oscillation occurring around  $\sim 800$  nm. It should be reiterated here that the phase of the modes is not the same concept as the CE phase. The two are separate concepts, with the CE phase only being valid when the laser is in the pulsed mode (mode-locked).

To understand this further, consider a fixed point in the cavity. The electric field of  $M$  oscillating modes is a superposition given by:

$$E(t) = \exp[i\omega_c t] \sum_{m=0}^{M-1} E_m \exp[i(2\pi m f_{rep} t + \varphi_m)], \quad (2.2)$$

where  $E_m$  is the temporal amplitude of each individual mode and  $\varphi_m$  is the phase of each mode. To simplify, each mode can be assumed to have the same amplitude. Then,  $E_m = E_0$ . The amplitude of the modes is not so important. The phase is the important parameter as it determines whether or not the electric fields interfere destructively and constructively. When the phases,  $\varphi_m$  of each mode are different, the fields do not oscillate in phase. [26]

However, once mode-locking has been achieved, the phases of the modes can be taken to be a constant value and the same for each mode. The resulting sum is a geometric series and can be summed as:

$$E(t) = E_0 \exp[i\varphi_0] \exp[i\omega_c t] \sum_{m=0}^{M-1} \exp[i2\pi m f_{rep} t] = \frac{\exp[iM 2\pi f_{rep} t] - 1}{\exp[i2\pi f_{rep} t] - 1} \exp[i(\omega_c t + \varphi_0)] \quad (2.3)$$

where  $\varphi_0$  is the constant mode phase value. The intensity of the resultant field is then given by:

$$I(t) = |E(t)|^2 = \frac{\sin^2\left(\frac{M 2\pi f_{rep} t}{2}\right)}{\sin^2\left(\frac{2\pi f_{rep} t}{2}\right)}. \quad (2.4)$$

The expression shows that locking the modes of the laser leads to a regular train of pulses separated by the cavity mode spacing.

The pulse duration can also be estimated from the previous derivation. Since the pulse duration depends on the available spectral bandwidth, the number of modes locked together will



determine the spectral bandwidth. The pulse duration can be estimated as  $\tau_p \approx \frac{1}{Mf_{rep}}$ . As the number of modes contributing to the spectral bandwidth increases, the pulse duration decreases. [26]

The shortening of the pulse duration is important when discussing the physical mechanism producing the mode-locking. In a Ti:Sapphire laser, the physical mechanism used is the Kerr Effect. The Kerr Effect is the self-focusing of light in a medium due to an intensity dependent refractive index. For a material, the refractive index can be written as  $n(t) = n_0 + n_2 I(t)$ , where  $n_0$  is the linear refractive index,  $n_2$  is the non-linear index, and  $I(t)$  is the laser intensity. For Ti:Sapphire,  $n_2 = 10.5 \times 10^{-16} \text{ cm}^2/\text{W}$ . [25]

As the light is focused into the laser crystal, the intensity profile of the light causes the index of refraction to be higher for the high intensity portions of the light and lower for the low intensity portions. Thus, the material effectively becomes a converging lens. The high intensity portions of the light are focused more strongly and are amplified more than the low intensity portions. As the light circulates the cavity, the low intensity portions experience a higher loss and are suppressed. This leads to a shortening of the pulse. Since shorter pulse durations (higher intensity) are favored by the Kerr Lens, more modes contribute to the bandwidth of the pulse to shorten the duration. This causes the modes to oscillate in phase.

An important point here is that the second order (group-velocity dispersion) and higher-order dispersions must be controlled in order to keep the pulse duration short enough to facilitate the Kerr-Lens mode-locking (KLM). This is usually accomplished by using a pair of prisms or by using chirped mirrors. The interplay of all of the effects, the Kerr Lens, the dispersion, and cavity losses leads to the formation of a soliton-like pulse. [23]

Another important point is that the mode-locking process for a Ti:Sapphire laser is not self-starting. The CW mode is preferred. In order to start the mode-locking, an intensity fluctuation must be applied to the laser to create the Kerr Lens. This is usually accomplished by rapidly moving a cavity mirror or by shaking the table on which the laser is mounted. [23]

## ***2.2b CE Phase Offset Frequency***

In the previous section, the mode-structure of a laser cavity and the process of mode-locking were discussed. This led to an equally spaced frequency comb where the spacing was

given by  $c/2nL$ . However, in a real laser cavity, the refractive index varies with frequency. In this case, the phase and group velocities of a pulse traveling through the cavity are different. This is the origin of the CE phase and is discussed in this section.

As a laser pulse travels, the carrier-wave travels at the phase velocity and the envelope travels at the group velocity. The phase velocity is given by  $v_p = \omega/k$  and the group velocity is given by  $v_g = (d\omega/dk)_{\omega_c}$ . If the medium does not possess a frequency dependent refractive index, then  $v_p = v_g$ . However, this is only true in vacuum and only approximately true in air.

If you consider a single laser pulse in the pulse train emitted by the mode-locked laser, it can be written as:

$$E(t) = E_0(t) \exp(i\omega_c t) \quad (2.5)$$

where  $E_0(t)$  is the envelope of the field. When the group and phase velocities are equal, the electric field of the pulse train can be expressed as:

$$E_{PT}(t) = E_0(t) \exp(i\omega_c t) \otimes \sum_{m=-\infty}^{m=+\infty} \delta(t - m\tau_{RT}) \quad (2.6)$$

where  $m$  is the pulse index,  $\tau_{RT} = 1/f_{rep}$ , and the summation is a comb function. The pulse train is simply the convolution of a single pulse with a comb function, which gives pulses separated by the repetition rate of the laser.

In the frequency domain, the pulse train is mathematically described as:

$$\tilde{E}_{PT}(f) = \tilde{E}_0(f - \omega_c/2\pi) \sum_{m=-\infty}^{m=+\infty} \delta(f - mf_{rep}), \quad (2.7)$$

where  $m$  is now the mode index as previously defined and the summation is also a comb function. This description gives the comb of mode orders underneath the laser spectrum. This is exactly what is described by Figure 2.6. [27]

Now, in the case where the group and phase velocities are different, a CE phase shift will arise in the pulse and will be different for each pulse in the pulse train. The CE phase shift of a pulse as it travels through a medium can be derived by starting with the following expression:

$$\Delta\phi_{CE} = kL(n_g - n) \quad (2.8)$$

where  $k = \frac{\omega}{c}$ ,  $L$  is the length of the medium,  $n_g$  is the group index of refraction, and  $n$  is the index of refraction. Note that the group index of refraction is defined as  $n_g = \frac{c}{v_g}$ . Equation

2.8 can further simplified as:

$$\Delta\phi_{CE} = \omega L \left( \frac{1}{v_g} - \frac{1}{v_p} \right) \quad (2.9)$$

By making the substitution:

$$\frac{1}{v_g} = \frac{n + \omega \frac{dn}{d\omega}}{c}, \quad (2.10)$$

Equation 2.9 becomes:

$$\Delta\phi_{CE} = \frac{\omega^2 L}{c} \frac{dn}{d\omega}. \quad (2.11)$$

This is the expression using frequency. However, experimentalists typically work with wavelengths. In this case, by the making the substitution:

$$\frac{dn}{d\omega} = \frac{dn}{d\lambda} \frac{d\lambda}{d\omega} = \frac{-2\pi c}{\omega^3} \frac{dn}{d\lambda}, \quad (2.12)$$

Equation 2.11 becomes:

$$\Delta\phi_{CE} = -2\pi L \frac{dn}{d\lambda} \quad (2.13)$$

Equation 2.13 is the simplest expression to use for calculations since the  $\frac{dn}{d\lambda}$  are tabulated for materials at different wavelengths. Also, note that all of the expressions assume evaluation of the derivatives and values at the central wavelength (central frequency). For example, fused silica has  $\frac{dn}{d\lambda} = -0.017288 \mu\text{m}^{-1}$  at 800 nm central wavelength. A theoretical plot is shown in

Figure 2.7. [27]

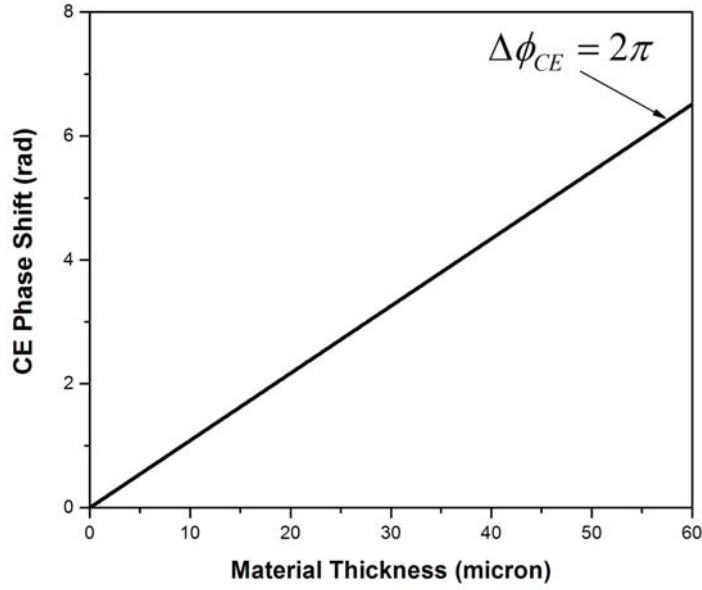


**Figure 2.7 Theoretical plot for the CE phase shift through fused silica at 800 nm central wavelength.**

The plot shows that for roughly 58 micron of fused silica, the CE phase will shift by  $2\pi$  radians. Thus, a small amount of material will impart a large CE phase shift. Considering that the crystal in the laser cavity is a few mm in length, the CE phase will shift by a large amount as it travels through the cavity.

If you take  $L$  to be the length of the laser cavity and account for all of the dispersive elements, Equations 2.11 and 2.13 will give the total CE phase shift through the cavity. Thus, for the  $j^{\text{th}}$  pulse exiting the cavity, the total CE phase can be written as  $\phi_{CE} = \phi_0 + j\Delta\phi_{CE}$ , where  $\phi_0$  is the CE phase of the  $0^{\text{th}}$  pulse. The next step is to derive the frequency domain expression, similar to Equation 2.7, for the case where dispersion exists.

The electric field of the pulse train, including the CE phase shift, can be expressed as:

$$E_{PT}(t) = \sum_{j=-\infty}^{j=+\infty} E(t - j\tau_{RT}) \exp[i(\omega_c t + j(\Delta\phi_{CE} - \omega_c \tau_{RT})) + \phi_0] \quad (2.14)$$

The Fourier transform of Equation 2.14 is given by:

$$\tilde{E}_{PT}(\omega) = \sum_{j=-\infty}^{j=+\infty} \exp[i(j(\Delta\phi_{CE} - \omega_c \tau_{RT}) + \phi_0)] \int E(t - j\tau_{RT}) \exp[-i(\omega - \omega_c)t] dt \quad (2.15)$$

Let  $\tilde{E}(\omega) = \int E(t) \exp(-i\omega t) dt$ . Also, using the Fourier shift theorem given by:

$$\int f(x - g) \exp(-i\alpha x) dx = \exp(-i\alpha g) \int f(x) \exp(-i\alpha x) dx \quad (2.16)$$

Equation 2.15 becomes:

$$\tilde{E}(\omega) = \exp(i\phi_0) \tilde{E}(\omega - \omega_c) \sum_{j=-\infty}^{j=+\infty} \exp[i(j\Delta\phi_{CE} - j\omega\tau_{RT})] \quad (2.17)$$

Finally, after applying the Poisson Summation Formula, Equation 2.17 becomes:

$$\tilde{E}(\omega) = \exp(i\phi_0) \tilde{E}(\omega - \omega_c) \sum_{m=-\infty}^{m=+\infty} \delta(\Delta\phi_{CE} - \omega\tau_{RT} - 2\pi m) \quad (2.18)$$

Equation 2.18 shows that the frequency comb, by adding a pulse to pulse CE phase shift, becomes translated. The frequencies of the comb are then given by:

$$f_m = \frac{m}{\tau_{RT}} - \frac{\Delta\phi_{CE}}{2\pi\tau_{RT}} \quad (2.19)$$

Equation 2.19 can be further simplified to:

$$f_m = mf_{rep} + f_0 \quad (2.20)$$

where  $f_0 = -\frac{\Delta\phi_{CE} f_{rep}}{2\pi}$ . The negative sign is dropped by convention as long as the sign of the

CE phase shift is changed as well, which is not so important. The offset frequency  $f_0$  is physically a positive number. The shifted frequency comb is shown in Figure 2.8. [27]

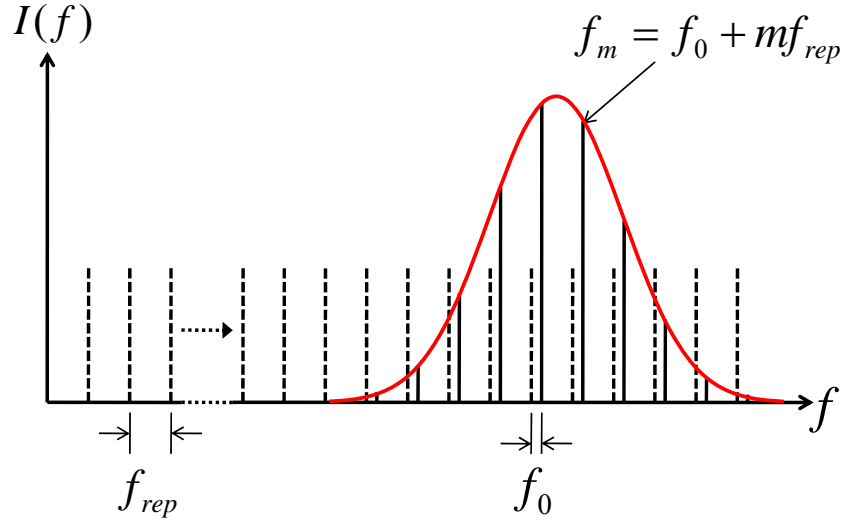


**Figure 2.8 Shifted frequency comb. The dashed arrow represents a large increase in frequency in order to show DC on the same axis.**

In the figure, the dashed lines represent the modes of the laser when the phase and group velocities of the pulse are equal. The solid lines represent the shifted modes of the laser underneath the gain spectrum in the presence of dispersion. In this case, the frequencies are given by Equation 2.20.

Thus, as the CE phase changes from pulse-to-pulse in the emitted laser pulse train, the mode spectrum is shifted as shown in Figure 2.8. In fact, the offset frequency is also defined as:

$$f_0 = \frac{1}{2\pi} \frac{d\phi_{CE}}{dt} = \frac{\Delta\phi_{CE} f_{rep}}{2\pi} \quad (2.21)$$

The offset frequency, though, does not maintain a constant value in the laser cavity due to fluctuations of the dispersion. The optical mounts in the cavity can shift, causing the path length to change and thereby changing the dispersion. Also, temperature shifts and air pressure changes can affect the dispersion encountered by the pulse circulating through the cavity. Thus, the CE phase changes as the offset frequency shifts. Since the pulse-to-pulse CE phase shift is related to the frequency domain, methods can be employed to lock the offset frequency to a set value and thus stabilize the phase shift between pulses in the pulse train to a known value.

## 2.3 Stabilization of the CE Phase

### 2.3a Review of the Technology

CE phase technology has been around for almost 12 years. With the development of KLM Ti:Sapphire laser oscillators, few-cycle pulses were available to researchers. Measurement of the CE phase or absolute phase of the pulses from such a laser was and still is to this day a major goal of researchers. Thus far, no group has managed to definitively measure the absolute phase of a pulse. The first attempt at measuring the pulse-to-pulse CE phase shift from a Ti:Sapphire laser oscillator was made in 1996. [28] In the experiment, the group used a Michelson interferometer to perform an interferometric cross-correlation of pulses from a sub-10 fs Ti:Sapphire laser in order to measure the relative phase shift between the pulses. The group used a pair of intracavity fused-silica wedges to introduce a CE phase shift. The investigation identified the main sources of CE phase noise in the laser and suggested that the intracavity pulse energy be used as a feedback mechanism for stabilizing the CE phase drift. [28]

A major paper on the subject was published in 1999. [29] In this paper, the methods for obtaining the offset frequency  $f_0$  were outlined and investigated. The methods investigated all involved comparing different parts of the laser spectrum using nonlinear processes or external oscillators. The group also investigated the bandwidth requirements and the number of nonlinear steps involved in obtaining the offset frequency. It was deduced that comparing comb orders through difference frequency generation (DFG) or second harmonic generation (SHG) would be the simplest since the method would involve only one nonlinear process. However, in order to implement either SHG or DFG, the laser spectrum would have to cover an octave. Such octave spanning spectra were not available at the time. The research group, though, was able to observe, but not lock, the offset frequency using a frequency interval bisection scheme. The offset frequency was found to arise in the MHz range. This paved the way for future research. [29]

Shortly after, in 2000, microstructure fibers with zero-dispersion points in the near infrared were introduced as a technology. [30] It was shown that an octave-spanning could be produced through the nonlinear processes induced through focusing a Ti:Sapphire laser into the small core. Then, using the new fiber technology, researchers were able to generate the offset frequency by frequency doubling the low frequency components of the octave-spanning spectrum and heterodyne beating them with the overlapping high frequency portions. [31,32]

This method is called  $f$ -to- $2f$  self-referencing and is the method used by most groups. Once the researchers had generated the offset frequency, they were able to lock it to a known value and thus stabilize the CE phase shift of the pulse-train.

Since that time, the CE phase stabilization of Ti:Sapphire laser oscillators has advanced rapidly. The state of the art is obtaining the offset frequency from octave-spanning [33] or near octave-spanning lasers [9] The popular method of  $f$ -to- $2f$  self-referencing will be discussed in the next section.

### 2.3b $f$ -to- $2f$ Self-Referencing

The  $f$ -to- $2f$  self-referencing method is a very simple scheme for obtaining the offset frequency. It requires only one nonlinear process in conjunction with spectral broadening of the laser spectrum over an octave. The nonlinear process used is SHG. Thus, the comb orders to be compared have a ratio of 2:1 or  $\frac{f_{2m}}{f_m} = 2$ , where  $m$  is the comb order. [29] Once an octave-spanning is obtained, the low frequency is doubled and the high frequency,  $f_{2m}$  interferes with the frequency-doubled low-frequency component,  $f_m$ . Mathematically, the interference between the two comb orders is represented as:

$$2f_m - f_{2m} = 2(mf_{rep} + f_0) - (2mf_{rep} + f_0) = f_0 \quad (2.22)$$

Figure 2.9 displays the process graphically.

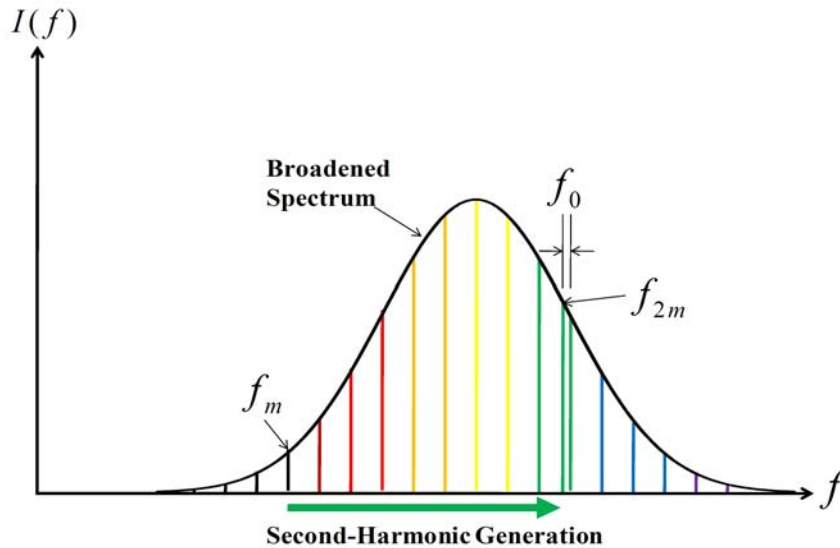


Figure 2.9  $f$ -to- $2f$  self-referencing



From the process, the offset frequency is obtained and appears in the tens of MHz range. [29] In this range, it is easy to track using spectrum analyzers. The next section discusses ways to lock the phase.

### ***2.3c Locking the Offset Frequency***

The offset frequency, which is directly related to the CE phase shift, can be locked and manipulated by several methods. First, the most popular method is to lock the offset frequency to a fraction of the repetition rate of the laser oscillator. In this case, the CE phase shift evolves linearly from pulse-to-pulse. By Equation 2.21, that evolution is known. Second, the offset frequency can be locked to an external reference, such as an RF oscillator. [34] This method is used by many in the frequency metrology community. Yet, another method, which was shown in 2005 [35] locked the offset frequency to zero frequency, which made the CE phase shift the same for every pulse in the pulse-train emitted by the laser.

The offset frequency, though, is susceptible to fluctuations of the laser parameters and to the environment in which the laser is housed. For example, the offset frequency was found to sweep through 100 MHz in the time period of milliseconds when the laser was on an open table. [29] This was due to air pressure and temperature variations of the cavity. The offset frequency is also susceptible to intracavity laser energy variations and to vibrations of the laser cavity. Ti:Sapphire lasers with intracavity prisms for dispersion compensation are especially susceptible to vibrations due to optical path length change. Thus, in order to accomplish CE phase stabilization, the laser used should be passively stable.

Two methods are commonly employed to lock the offset frequency to a value. The first involves quickly tilting a mirror in the cavity to change the optical path length of the pulse. This method only works in lasers utilizing prisms for dispersion compensation. By changing the path length, the amount of dispersion experienced by the pulse is varied, which causes the offset frequency to change. [36] The second method involves varying the pump power. By varying the pump power, the nonlinearity in the Ti:Sapphire crystal is changed. A pulse traveling through the crystal will experience a different amount of dispersion and thus vary the offset frequency. This can be understood by the Kerr effect. The dispersion in the Ti:Sapphire crystal is given by  $n(I) = n_0 + n_2 I$ . As the pump power is modulated, the intensity in the crystal changes thereby

changing the dispersion. Varying the pump power is the only way to lock the offset frequency in lasers using chirped mirrors for dispersion compensation. [37,38] The next chapter discusses the experimental details of the CE phase stabilization of the Kansas Light Source oscillator.

## CHAPTER 3 - Stabilization of the CE Phase of the KLS Oscillator

### 3.1 The KLSI Laser Oscillator

The foundation of the Kansas Light Source laser system consists of a chirped mirror dispersion-compensated KLM Ti:Sapphire laser oscillator (Femtolasers Scientific Pro S). This laser is used to seed a multi-pass grating-based amplifier, which will be described in a later chapter. The KLSI laser oscillator is shown in Figure 3.1.

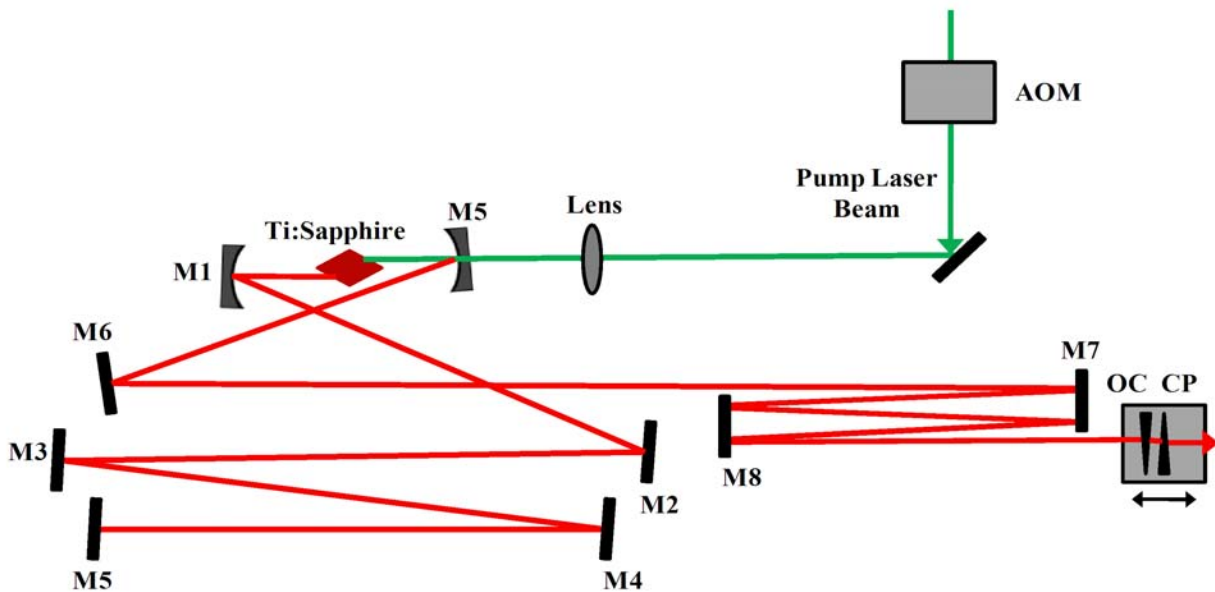


**Figure 3.1 The KLSI Laser Oscillator. M1-M8: cavity mirrors, AOM: acousto-optic modulator, OC: output coupler, CP: compensating plate**

In the laser oscillator, a pump beam from the diode-pumped-solid-state (DPSS) laser (Coherent Verdi VI) centered at 532 nm central wavelength, was focused into the Ti:Sapphire crystal by the lens. The absorbed energy created the population inversion in the crystal while the transmitted pump energy traveled out of the cavity through M1. In this laser, the Ti:Sapphire crystal was about 2.3 mm long and cut at Brewster's angle. The pump laser and the corresponding laser emission were horizontally polarized. The output coupler was cut at an

angle of 10 degrees to prevent back reflections of secondary reflections into the cavity, which would disturb the laser operation. The compensating plate was cut at the same angle and placed close to the output coupler in order to compensate the spatial dispersion.

Once lasing had occurred, two stable modes of operation existed for the laser, though an unstable hybrid mode did exist, called a Q-switch mode, but was undesirable for applications. The first mode was the CW mode. The CW mode had a central wavelength of  $\sim 800$  nm, which corresponded to the peak of the gain curve of the Ti:Sapphire crystal. This mode was the preferred mode of operation for the laser. Of course, the mode-locked state was second. In this laser, the intracavity chirped mirrors provided the dispersion compensation, which kept the pulse short and the intensity high in the laser crystal.

Stable mode-locking existed for only two regions, called stability zones. The stability range is given by  $\delta = d - 2f$ , where  $d$  is the distance between M1 and M5 and  $f$  was the focal length of the focusing mirrors. Experimentally, determining the best position of the crystal and focusing mirrors which would yield a mode-locked state was found by optimizing the CW operation to yield the highest output power. This power was generally around 620 mW. Then, the distance between M1 and M5 would be slowly changed to decrease the power to roughly 400 mW. The mode-locking only started at the edge of a stability zone. In order to start the mode-locking, either M5 or the OC/CP, which were mounted on translation stages, were rapidly moved. This gave the needed intensity fluctuation in the crystal, which initiated the mode-locking.

Once mode-locking had been started, the laser remained in that state unless stopped. The mode-locking provided  $\sim 5.3$  nJ energy output pulses at a repetition rate of  $\sim 76$  MHz, which corresponded to a cavity length of almost 2 m. The temporal separation of pulses in the pulse train was  $\sim 13$  ns. The polarization of the output pulses was horizontal.

The additional components added to the oscillator layout were the acousto-optic modulator (AOM) in the pump beam path and the translation stage on which the output coupler and compensating plates were mounted. The AOM was used to modulate the pump power in order to lock the offset frequency and stabilize the CE phase. The translation stage was used to move the offset frequency to the locking frequency used. By moving the translation stage, the dispersion in the cavity was changed, which changed the offset frequency. These components will be further discussed in an upcoming section.

The output spectrum of the laser is shown in Figure 3.2.

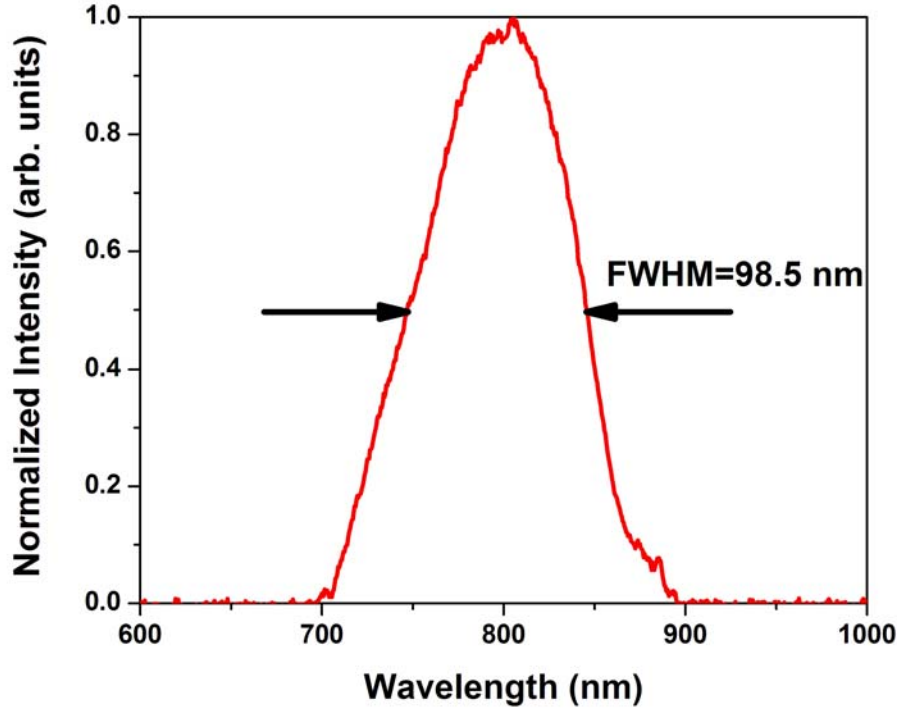


**Figure 3.2 Kansas Light Source Oscillator Spectrum**

The spectrum of the laser pulses from the Kansas Light Source laser is broad. In this figure, the FWHM is 98.5 nm. By optimizing the laser cavity, a broader spectrum can be obtained. However, this is the typical spectrum obtained.

If a pulse from the oscillator is assumed to be transform-limited and a Gaussian pulse-shape is assumed, then the pulse duration can be estimated by the fourier time-bandwidth product  $\Delta f_p \tau_p = \sqrt{2 \ln 2} / \pi$ , where  $\Delta f_p$  is the spectral FWHM and  $\tau_p$  is the pulse duration. For the spectrum in Figure 3.2, the spectral width is  $\Delta f_p = 4.64 \times 10^{13}$  Hz. This yielded a theoretical pulse duration of  $\sim 9.5$  fs. Typically, though, the pulse duration will be longer due to higher-order dispersion from the output coupler, compensating plate, and Ti:Sapphire crystal. [39]

Also, recalling the discussion of cavity modes from Chapter 2, the number of modes contributing to the mode-locking can be estimated from Figure 3.2. Since the spectrum extends from roughly 700 to 900 nm, the spectral width is about  $9.6 \times 10^{13}$  Hz. Assuming the laser

repetition rate was about 76 MHz, the number of modes contained in the spectrum was  $\sim 1.2 \times 10^6$ .

The spectrum obtained from the oscillator, though, was not wide enough to employ the  $f$ - $to$ - $2f$  self-referencing method discussed in Chapter 2. It did not span an octave in frequency. In the next section, the method used to obtain the offset frequency will be discussed.

## 3.2 Self-Referencing Setup

### 3.2a PCF Setup

In order to detect the offset frequency,  $f_0$  described in chapter 2, the laser spectrum from the KLS oscillator had to be broadened over an octave since the laser bandwidth extended from only 700 to 900 nm. In order to accomplish this task, a photonic crystal fiber (PCF) was used.

PCF technology is relatively new, only being around since the early part of the century. A normal fiber guides the light by total internal reflection between a high-index core and a lower index cladding. [40] A PCF, though, has a hybrid high/low index structure, which is used to give the fiber unique dispersive properties. The zero-dispersion (second-order) point of the fiber can be shifted to match the central wavelength of the in-coupled laser. Second-order dispersion leads to a chirping of the pulse and thus a temporal broadening. In fact, the fiber properties can also be manipulated to exhibit negative group-velocity dispersion at a desired wavelength. This slows the temporal broadening of the pulse through the fiber, allowing a higher intensity to be maintained along the length of the fiber. The high intensity would then yield higher nonlinear effects. For spectral broadening, nonlinear effects such as self-phase modulation, self-steepening, and four-wave mixing occur along the interaction. Those nonlinear processes broaden the spectrum of the in-coupled laser. [40]

An important point here is that the nonlinear processes occurring inside the fiber are wave-mixing processes. In the wave-mixing process, adjacent laser comb orders are added/subtracted to yield new lines, which broaden the spectrum. [40] This preserves the comb structure of the incident laser beam as the comb orders are still separated by the laser repetition rate. If this were not true, then the  $f$ - $to$ - $2f$  self-referencing method would not work. The comb orders obtained from the spectral broadening must be the same as for the in-coupled laser light.

The PCF used in the self-referencing setup for the KLS laser was purchased from Menlosystems GmbH and comes standard in their XPS 800 setup for CE phase stabilization. The PCF setup is shown in Figure 3.3.

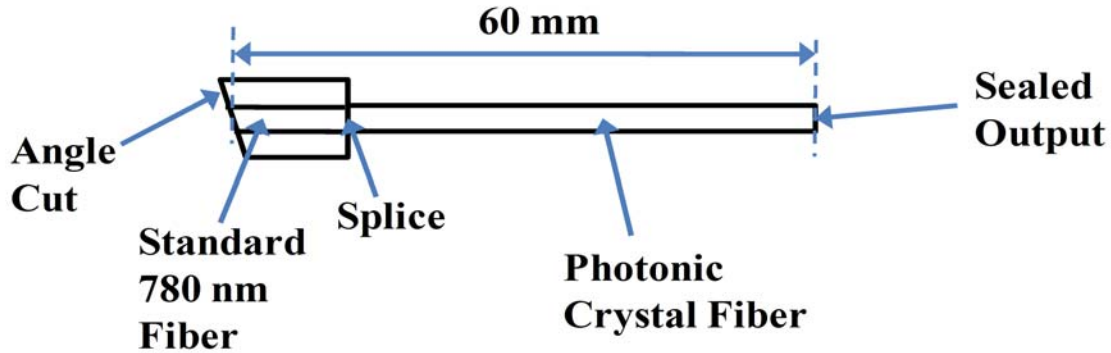


**Figure 3.3 PCF setup for spectral broadening.**

On the left side of the figure is the input of the PCF. The face of the fiber was cut at an angle of 10 degrees to prevent back reflections from going back to the oscillator and disrupting the mode-locking. In order to facilitate coupling of the laser to the setup, the input fiber was a standard 780 nm optical fiber. The fiber had a numerical aperture of  $NA=0.13$  and a mode-field diameter of 5 micron. Note that mode-field diameter is not exactly a measure of the fiber diameter, but a measure of the beam width which propagates in the core and cladding. The larger diameter in-coupling fiber provided an easier way to couple into the smaller core PCF. This is shown in the diagram where the in-coupling fiber is spliced to the PCF. The in-coupled light propagated through the in-coupling fiber and into the 2 micron PCF. The length of the fiber setup was 60 mm and was sealed off completely from the outside environment. The PCF itself was composed of a solid silica core surrounded by air holes. The zero-dispersion point of the fiber was around 780 nm. [41]

### ***3.2b Spectral Broadening with the PCF***

In the experiment, the pulses from the KLS laser were bounced once off of two chirped mirrors ( $-65 \text{ fs}^2 / \text{bounce}$ ) and then focused into the fiber setup by an  $f=7.5 \text{ mm}$  aspheric lens. An aspheric lens was used to reduce spherical aberration of the focused laser and to match the NA of the in-coupling fiber.

The output spectra obtained from focusing the KLS laser into the PCF are shown in Figure 3.4.

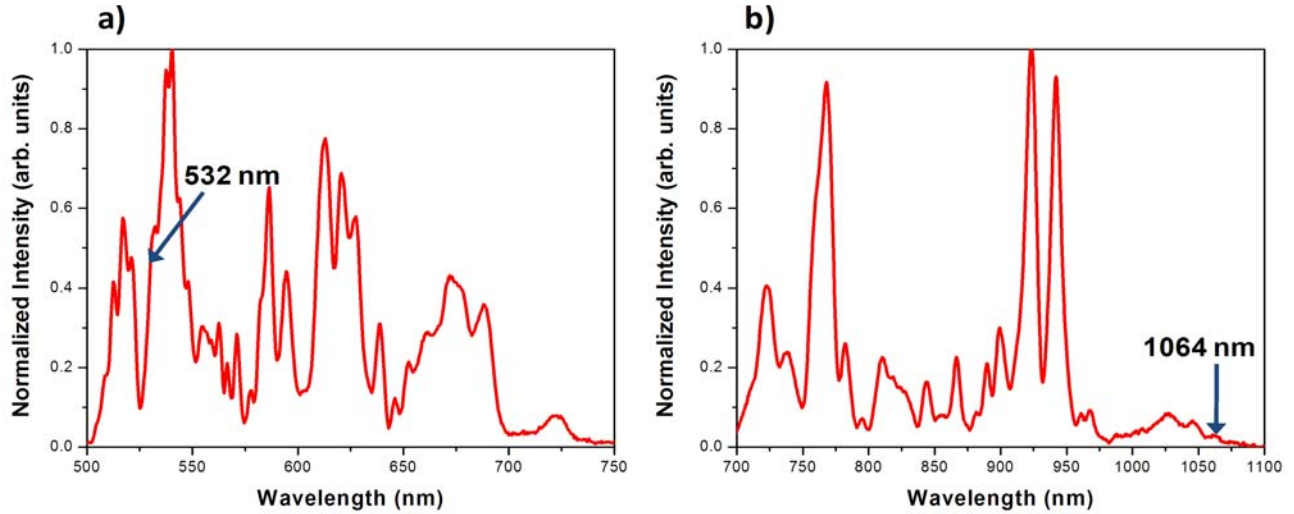


**Figure 3.4 PCF output spectra: a) low wavelength portion of the spectrum, b) spectrum measured with a >700 nm filter**

In Figure 3.4, each portion of the spectrum had to be measured separately with the spectrometer, which could not measure the broad spectrum without including 2<sup>nd</sup> order diffractions in the long-wavelength portion. For example, b) was measured with a >700 nm longpass filter to prevent the 2<sup>nd</sup> order diffractions from 500 nm from showing up around 1 micron. In the experiment, approximately 200 mW of mode-locked output power from the KLS oscillator were coupled into the PCF. The output power of the light emerging from the PCF was ~50 mW, giving a throughput of 25%. At times, the power could be higher or lower depending on the input beam mode, input laser power, and geometric coupling.

As can be seen from the data, the original spectrum of the KLS laser, which originally extended from ~700 to 900 nm, was broadened to cover ~500 to 1075 nm. Such a broad spectrum was over an octave and sufficient for  $f$ -to- $2f$  self-referencing to obtain the offset frequency. Of course, adjustment of the in-coupled laser power and laser polarization would also affect the spectral broadening. The PCF itself was not symmetric in structure, leading to a polarization dependent nonlinearity. Changing the laser polarization would adjust the spectral width and the amplitude at different wavelengths.



Changing the laser power had the most dramatic effect on the spectrum obtained from the PCF. The situation when the in-coupled laser had a lower power is shown in Figure 3.5.

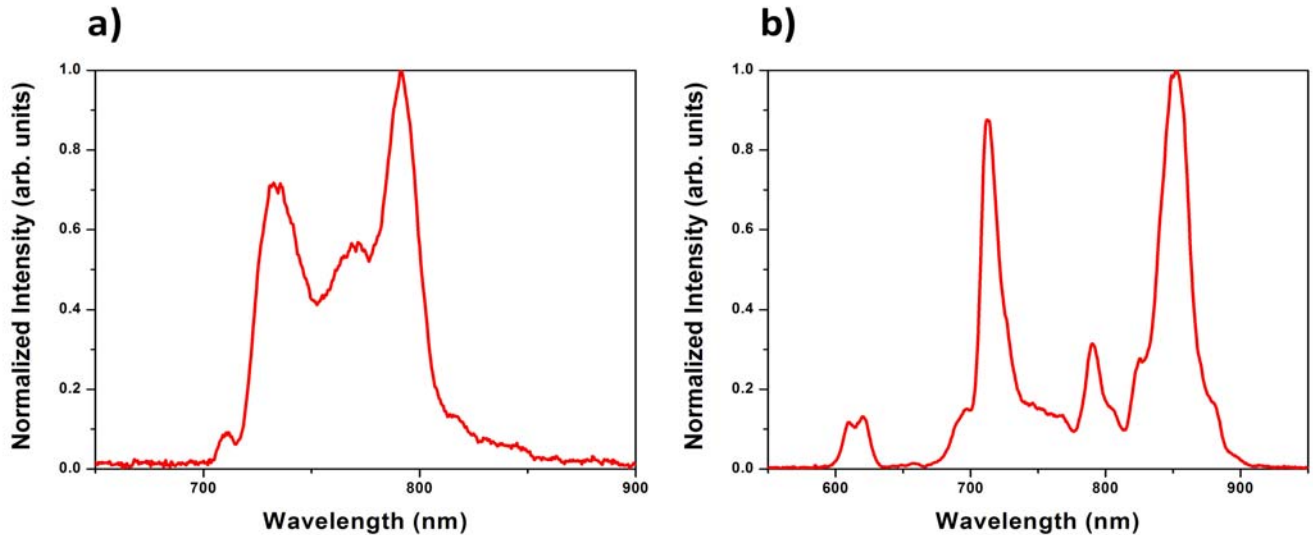


**Figure 3.5 PCF output at lower power: a) 6 mW output power, b) 18 mW output power**

As can be seen from the figure, at the lower output power of 6 mW, the spectrum tended to shift toward lower wavelengths, but was still not broad enough for offset frequency detection. When the output power was three times larger, the spectrum started to become much broader and started to shift toward longer wavelengths. Experimentally, the broad spectrum necessary for obtaining the offset frequency usually emerged at powers over 35 mW. However, the offset frequency signal-to-noise ratio was always better when the power was closer to 50 mW.

### **3.2c *f-to-2f* Setup**

The *f-to-2f* self-referencing required the second harmonic generation of a portion of the spectrum from the PCF around 1064 nm. Then, the second harmonic would be overlapped and interfered with the corresponding low wavelength at 532 nm. If you look at Figure 3.4, the 1064 nm component was in the extreme end of the spectrum obtained from the PCF and appeared to have little energy. However, the amplitude, or energy, of the spectral components around 1064 nm could be increased by changing the polarization of the laser input to the PCF or by adjusting the geometric coupling to the fiber.

The optical layout designed to obtain the offset frequency is shown in Figure 3.6.

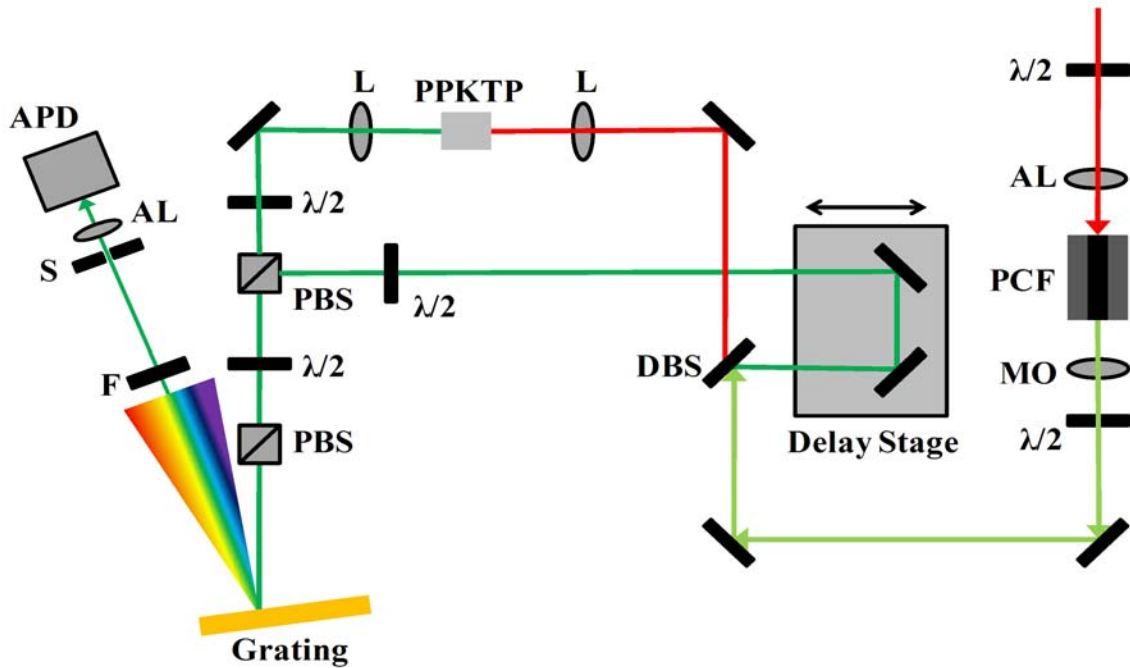


**Figure 3.6 *f-to-2f* Interferometer for self-referencing;  $\lambda/2$ : half-waveplate, AL: aspheric lens, PCF: photonic crystal fiber, MO: microscope objective, DBS: dichroic beamsplitter, L: lens, PPKTP: periodically-poled KTP, PBS: polarizing beamsplitter cube, F: filter, S: slit, APD: avalanche photodiode**

In the setup, 200 mW, which was half of the output from the KLS laser oscillator, was passed through a half-waveplate, was used to adjust the spectral broadening in the PCF by exploiting the non-symmetric nature of the PCF structure, and then focused in to the PCF by an  $f=7.5$  mm lens. The light leaving the PCF, which was then a broad spectrum, was collimated by a microscope objective having a numerical aperture of 0.40, which was identical to the NA of the fiber. A half-waveplate was then used to adjust the polarization of the beam to horizontal polarization since the PPKTP crystal was cut for Type I (o-o-e) phase matching. The long-wavelength portion and the short-wavelength portion of the white light were split by a dichroic beamsplitter. Figure 3.7 shows the portion of the white-light that propagated through each arm of the interferometer.

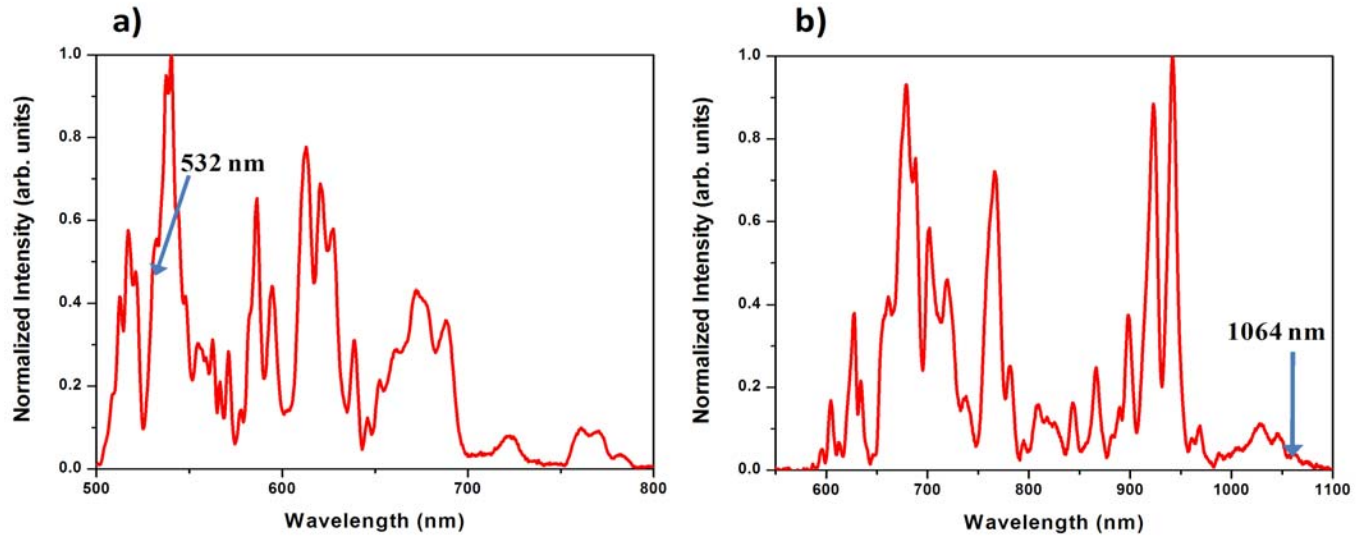


**Figure 3.7 Reflected and transmitted spectra from the dichroic beamsplitter: a) reflected spectrum, b) transmitted spectrum.**

As is shown, the short-wavelength components traveled through the lower arm of the interferometer and the long-wavelength components were sent to the top arm for frequency doubling.

A PPKTP crystal was used to obtain the second harmonic because of its high conversion efficiency and for the fact that it displayed zero walk-off. The crystal was periodically-poled, which meant that the sign of the nonlinearity changed as the phase of the second harmonic light and the fundamental light became unmatched. This yielded a higher intensity and allowed the beams to be overlapped. Most  $f$ -to- $2f$  interferometers use a BBO crystal. A BBO uses birefringent phase-matching which resulted in walk-off between the fundamental and second harmonic light. The walk-off reduced the nonlinear interaction and made alignment difficult.

The long-wavelength components were focused into the 5 mm thick PPKTP crystal, which was cut for Type I phase-matching for SHG of 1064 nm, by an  $f=50$  mm lens. The second harmonic was collimated by an identical lens. The mirror after the SHG setup was designed for high-reflectivity of 532 nm light. This mirror acted as a spectral cleaner as it transmitted almost all other wavelengths. The second harmonic light was also vertically polarized. A half-waveplate was used to rotate the polarization of the second harmonic light to horizontal so it could pass through the polarizing beamsplitter cube (PBS).

Alternately, the short-wavelength portion of the light was passed through a delay stage. A half-waveplate was placed before the dichroic beamsplitter to adjust the amplitude of the fundamental green light that would be reflected from the polarizing beamsplitter. The function of the PBS should be noted. The cube was basically two right angle prisms cemented together with a special coating along the interface. Horizontally polarized light was transmitted and vertically polarized light was reflected. Thus, the fundamental green light was reflected and the second harmonic beam from the top arm was transmitted.

At this point in the interferometer, the two beams were spatially overlapped and adjusting the delay stage allowed for temporal overlapping, but their respective polarizations were different. In order to overlap the electric fields of the two beams, a half-waveplate was placed before a second PBS. The half-waveplate was rotated such that the two beams' polarizations were rotated roughly 45 degrees, giving each beam a combination of horizontal and vertical polarization. After passing through the polarizing beamsplitter, the two beams were spatially and temporally overlapped in addition to having the same polarization. The next step was to spectrally filter the beam and choose only the wavelengths which would contribute to obtaining the offset frequency.

In order to accomplish this task, the beam was directed to a grating, which spatially separated the wavelengths. An interference filter, with a 2 nm FWHM bandpass centered at 532 nm, was placed in the position of the 532 nm light. The transmitted light was then further spectrally filtered with a slit and then focused onto the detector in the avalanche photodiode (APD) by an aspheric lens. The spectrum entering the APD is shown in Figure 3.8.

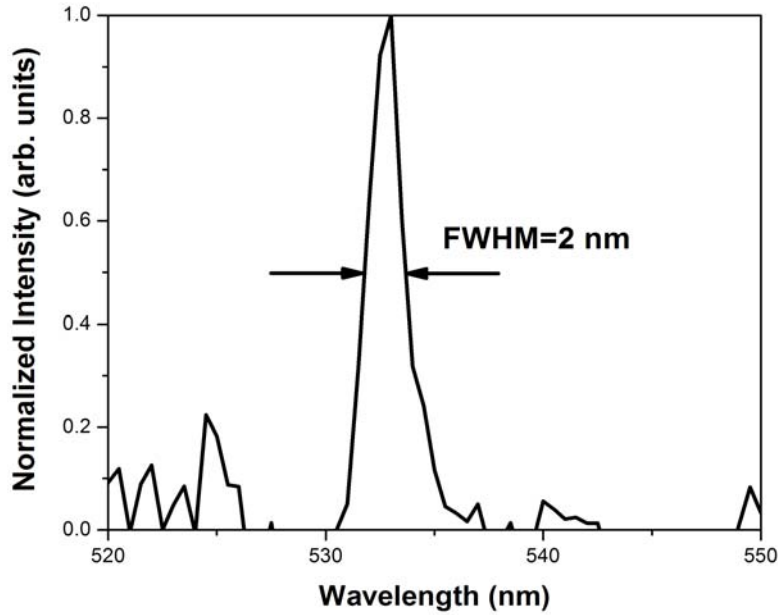


**Figure 3.8 Spectrum focused into the APD.**

A good signal-to-noise (S/N) ratio was obtained by focusing only the components from the fundamental green light that overlapped with the frequency doubled infrared components into the APD. Any other frequencies would only contribute as noise and would decrease the S/N.

The number of comb orders contributing to the spectrum in Figure 3.8 can also be estimated using the same method as for the oscillator spectrum in section 1 of this chapter. Assuming the laser repetition rate is 76 MHz and the comb lines within the 2 nm FWHM contribute the most energy, the number of comb orders contributing to the beat signal is  $\sim 28000$ . So, in the actual interference process where the offset frequency is obtained, many lines are actually contributing to the beat signal.

The interference signal obtained is shown in Figure 3.9. The detected frequencies are the result of the  $f$ -to- $2f$  self-referencing method. The offset frequency,  $f_0$  is near 20 MHz and the repetition rate,  $f_{rep}$  is near 76 MHz. The mirror frequency, which is the difference in the repetition rate and the offset frequency, is also shown.

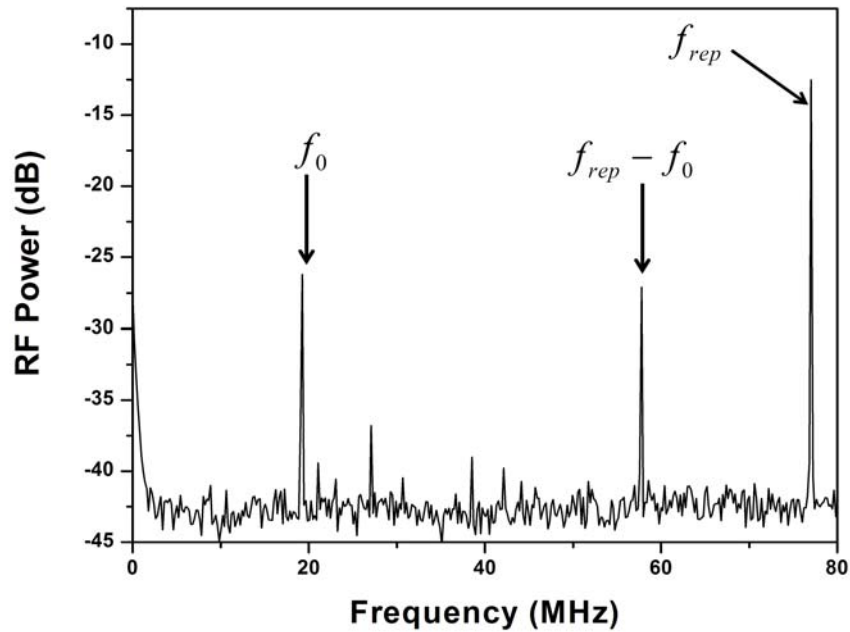
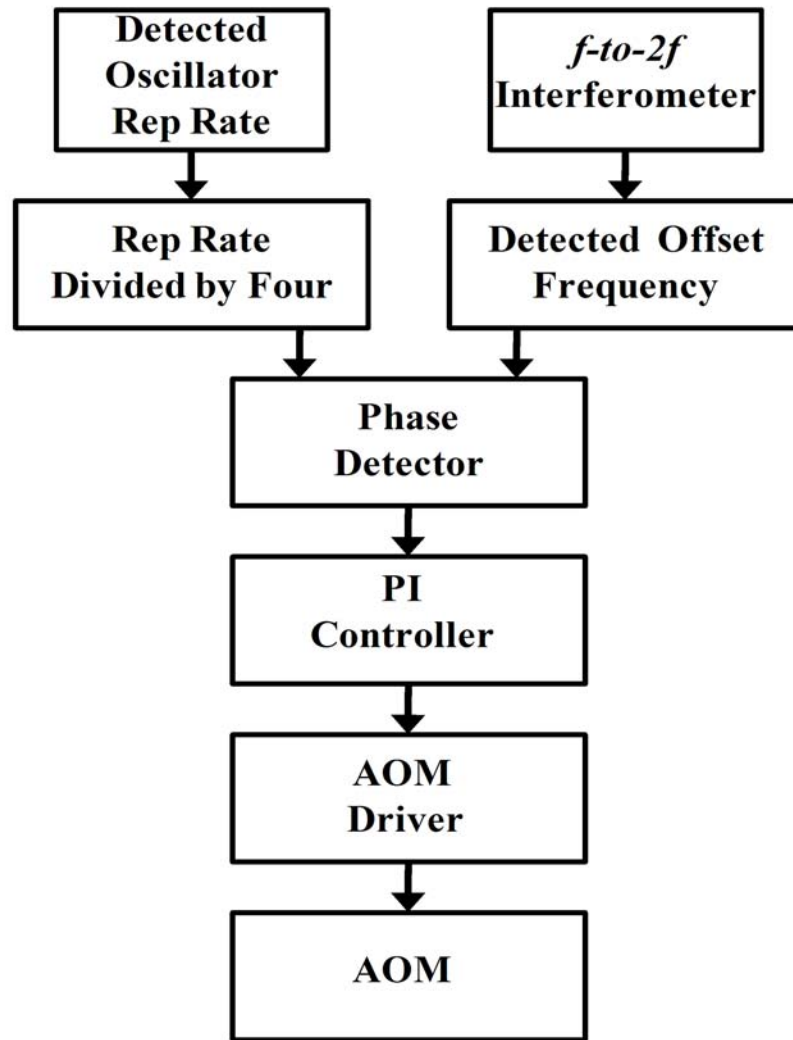


Figure 3.9 Signal obtained from the  $f$ -to- $2f$  interferometer.

### 3.3 Phase-Locking Loop

The phase-locking loop used to lock the offset frequency was also from Menlosystems GmbH. It consisted of several modules including a PI controller, phase detector, and frequency distributor. The phase-locking bandwidth, the frequency range over which it could track and control a frequency, of the Menlosystems unit was  $\sim 1$  MHz. The system locked the offset frequency to one-quarter of the laser repetition rate. A division by four was chosen so that every fourth pulse leaving the oscillator would have the same CE phase when the offset frequency was locked. A flowchart of the phase-locking system is shown in Figure 3.10.



**Figure 3.10 Phase-locking system.**

The basic scheme of the phase-locking system is shown in the figure. First, the repetition rate of the laser was detected and divided by four. At the same time, the offset frequency was obtained from the  $f$ -to- $2f$  interferometer. The divided repetition rate and offset frequency were compared in a phase detector, which output an error signal to the proportional-integral (PI) controller. The PI controller provided an output to the AOM driver, which drove the AOM in the laser cavity.

Another view of the phase-locking system is provided in Figure 3.11.

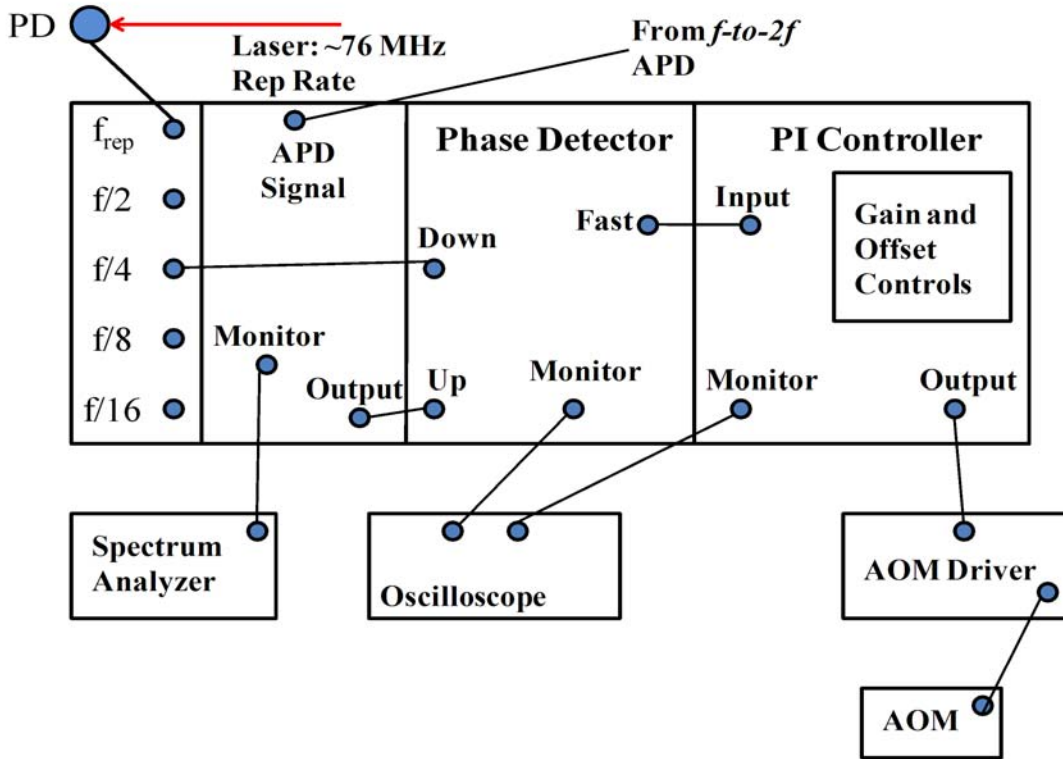


**Figure 3.11 Schematic of the phase-locking loop.**

The above figure displays the routes of the signals through the system. The repetition rate divided by four was sent to the “down” input of the phase detector while the offset frequency signal was sent to the “up” input. A spectrum analyzer and oscilloscope were used to monitor the signals.

The phase detector could measure a phase difference of  $\pm 16\pi$ . Mathematically,

$V_1(t) = V_1 \exp[-i2\pi(\frac{f_{rep}}{4})t]$  is the signal from the frequency distribution unit and

$V_2(t) = V_2 \exp[-i2\pi f_0(t) - i\varphi_0(t)]$  is the signal from the APD, where  $\varphi_0(t)$  is a temporally varying phase offset. The phase detector measures the signal:

$$\varphi(t) = 2\pi(\frac{f_{rep}}{4} - f_0)t + \varphi_0(t) \quad (3.1)$$



When  $\frac{f_{rep}}{4}$  and  $f_0$  are not equal, the phase changes linearly with time, leading to a sawtooth waveform, which corresponds to the  $\pm 16\pi$  measurement of the phase difference. When the two frequencies are equal, then the phase is locked to zero.

The sawtooth waveform for unequal frequencies is shown in Figure 3.12.

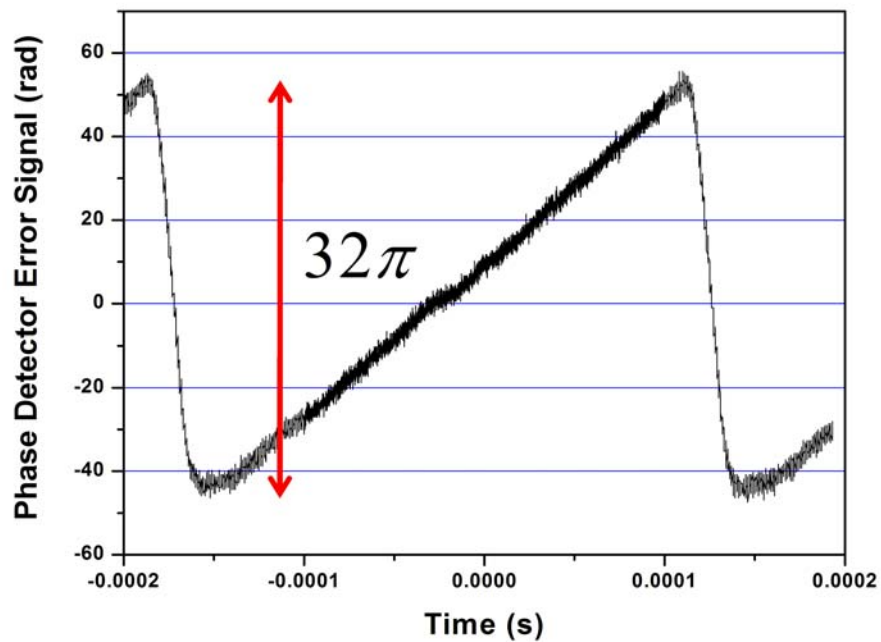


**Figure 3.12 Phase detector output**

In the figure, the sawtooth waveform represents the measurement of the  $\pm 16\pi$  range. The vertical axis was calibrated by measuring the voltage of the waveform with an oscilloscope and then dividing the total voltage difference by  $32\pi$ .

This signal was then sent to the PI controller of the Menlo systems unit, where a proportional and integral gain was applied to the error signal. A diagram of the PI controller circuit is in Figure 3.13.

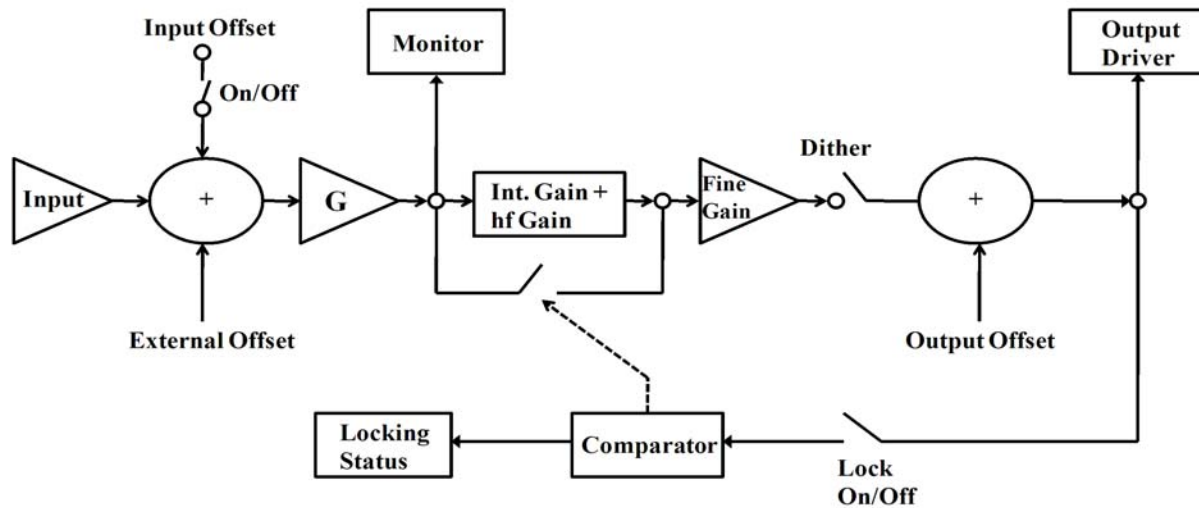


**Figure 3.13 PI controller circuit diagram.**

In the circuit, the input is the error signal from the phase detector. Optional external and internal offsets can be applied to the error signal. Then, a proportional gain is applied to the signal. Subsequently, an integral gain and a high frequency gain are added to the signal. Then, the signal has a fine gain applied and if needed, an output offset. Finally, the signal is sent to the output driver when the lock is engaged. [41]

The output driver sent a voltage to the AOM driver, which then amplified the signal and sent it to the AOM in the pump beam path of the oscillator. The AOM worked as a Bragg diffraction device, which was essentially a transmission grating. The sound field applied to the acousto-optic crystal acted as the grating. As the voltage applied to the AOM changed, part of the laser beam was deflected into the first order diffraction. The 0-order beam was used to pump the KLS laser. The action of the AOM is shown in Figure 3.14. [42]

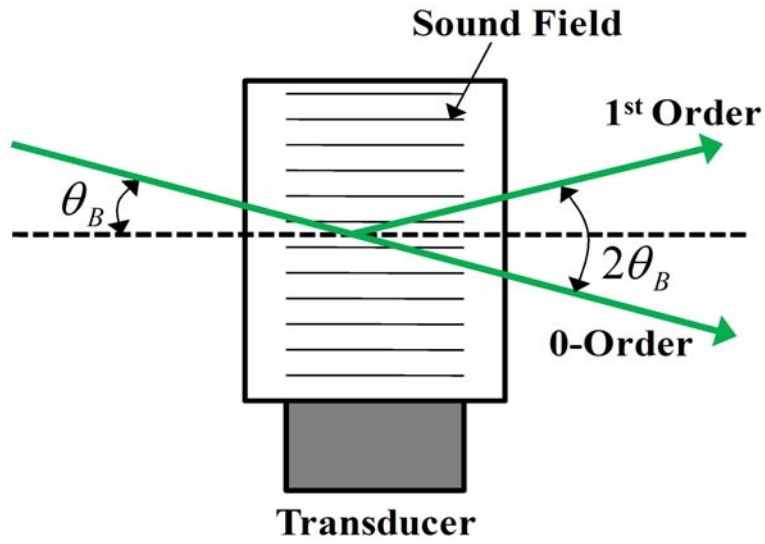


Figure 3.14 AOM,  $\theta_B$  : Bragg angle

### 3.4 Results and Discussion

The linewidth of the offset frequency is shown in Figure 3.15.

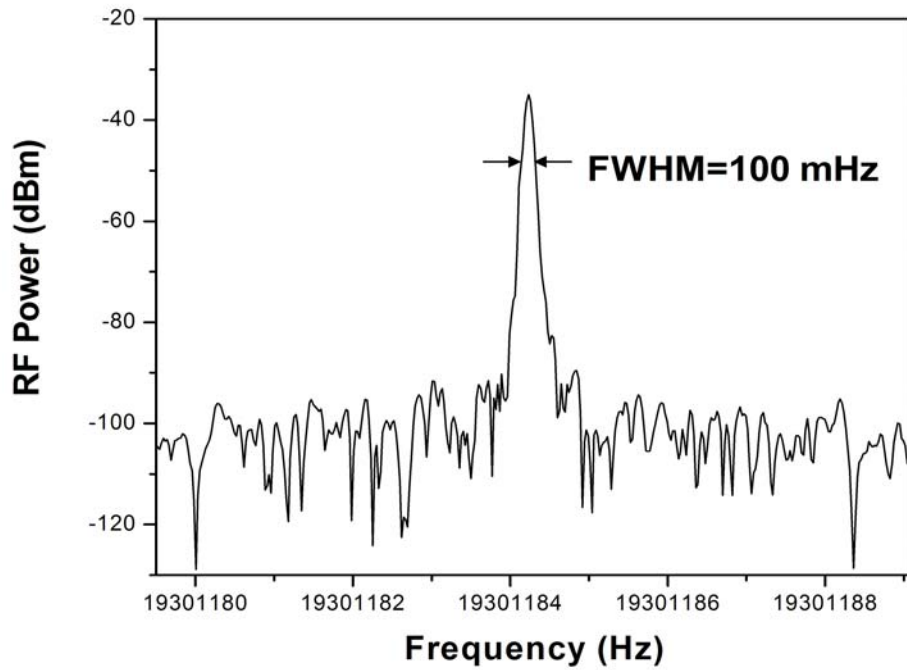
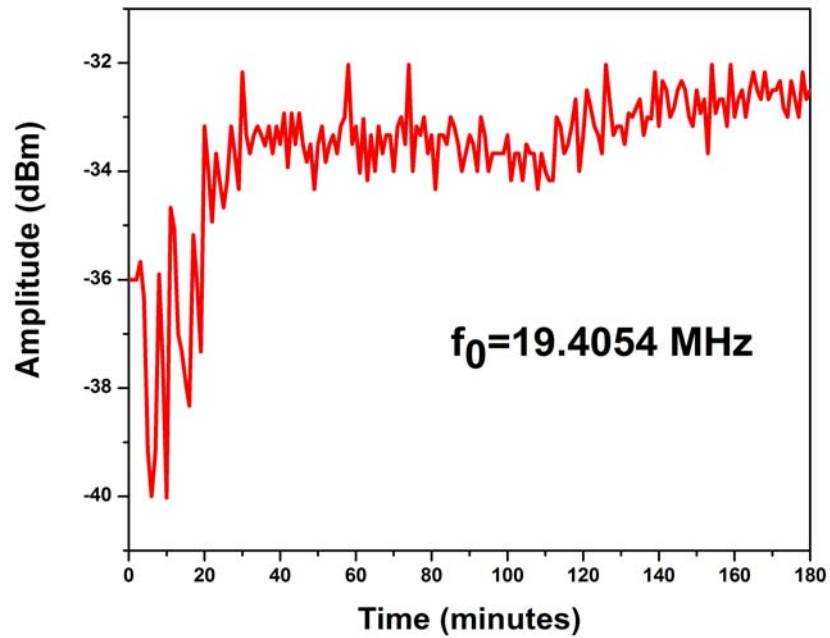


Figure 3.15 Linewidth of the offset frequency when the phase-locking loop was engaged.

The width of the offset frequency was measured with a spectrum analyzer utilizing a fast FFT algorithm. This result shows that the offset frequency could be locked to within a 100 mHz linewidth. The criterion for CE phase locking is that the offset frequency should be locked to less than 1 Hz. A 1 Hz drift would yield a  $\sim 1$  rad pulse-to-pulse shift in the CE phase due to the time-frequency relationship. The width of the peak could be further resolved for longer observation times using the FFT analyzer. The measurement in Figure 3.15 could in fact be less than 100 mHz. Extending the time scale over which the offset frequency was observed would yield a finer frequency bandwidth. This is not so important since the linewidth was verified to be much less than 1 Hz.

Typically, the offset frequency can be locked for five to tens of minutes in normal lab operation, i.e. when people are working on the table; the lab door is opened and closed, etc. The time can be even less if the laser is unstable. However, when the optical table is not perturbed and the laser is operating in a very stable state, the offset frequency can be locked over many hours. The offset frequency amplitude then becomes the limiting factor. The offset frequency must remain  $\sim 35$  dB in amplitude within a 100 kHz bandwidth in order for the electronics to track the signal. [41] The coupling to the fiber can shift, though, as the optical mounts relax. The offset frequency amplitude plotted over three hours is shown in Figure 3.16.



**Figure 3.16 Offset frequency amplitude vs. time.**

As is shown, the amplitude of the offset frequency started around 36 dB and slightly increased in value. The amplitude then decreased over the first hour and then stayed around ~33 dB during the remaining period of the locking time. The amplitude was not adjusted during this period.

An example of the phase detector output and the AOM control voltage during operation of the phase-locking loop are shown in Figure 3.17.

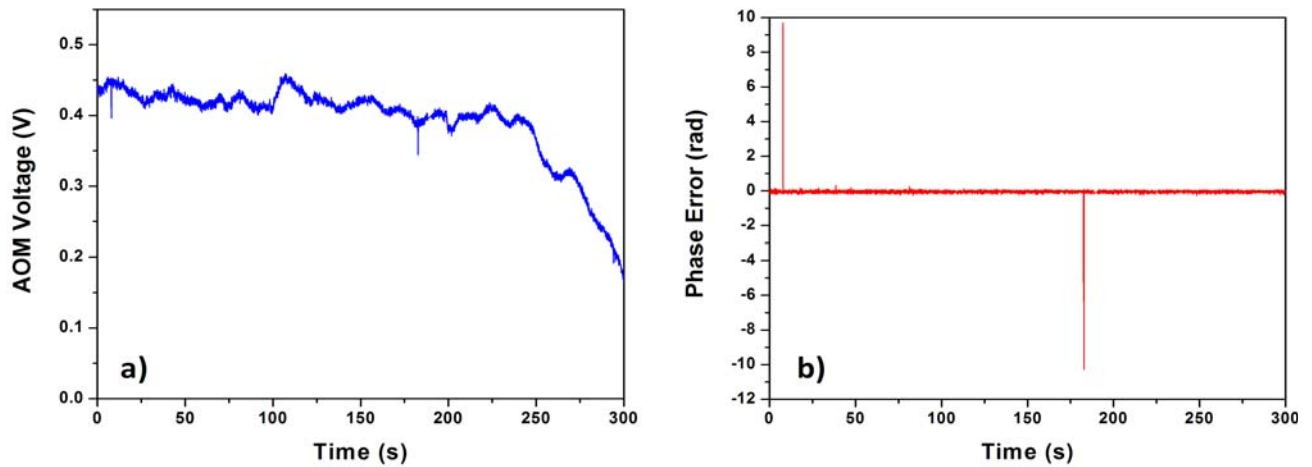


**Figure 3.17 a) AOM control voltage, b) Phase detector output.**

The data was collected over a five minute run. The two spikes in the phase detector output occurred when the optical table near the laser oscillator was momentarily perturbed. The perturbation led to a large spike in phase error showing the need for stability of the lab conditions during CE phase stabilization.

The AOM control voltage started at a value of  $\sim 440$  mV, which was the center of the locking range. As the locking began to slip, near 300 s, the control voltage reached to  $\sim 200$  mV. In fact, at a value of  $\sim 100$  mV, the locking loop failed and the offset frequency could no longer be locked. The AOM control voltage kept between 100 mV to 800 mV at roughly 400 mV during normal locking operation. The locking failed at the extreme ends of that range. Also, the control voltage showed a slow drift in addition to a fast drift. By applying a high-pass filter ( $>500$  mHz) to the AOM control voltage output showed that the fast variation was  $\sim 1\%$ .

The rms deviation of the phase detector output for the time period between the first spike in phase error and the second spike is shown in Figure 3.18.

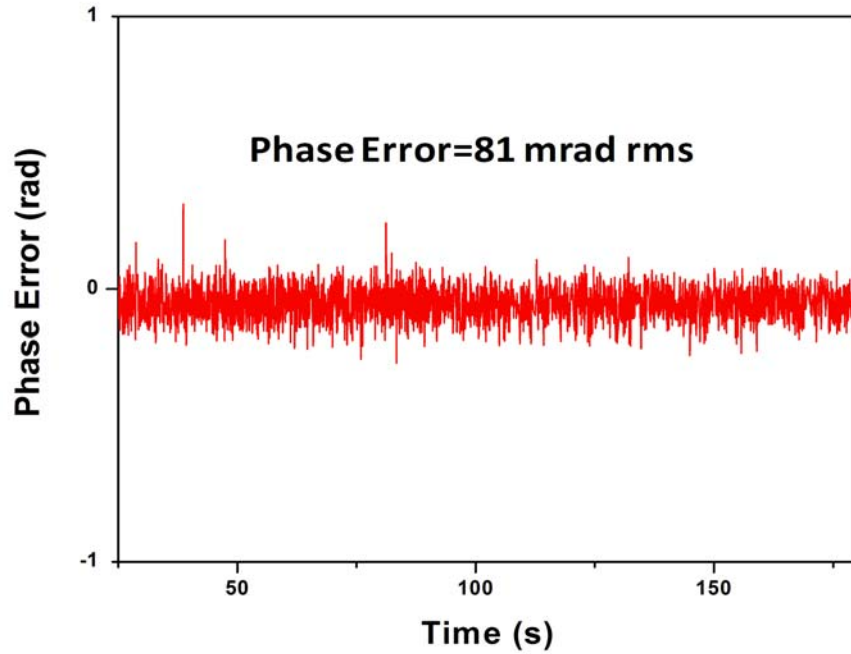


**Figure 3.18 Phase detector output stability.**

The phase detector output showed an 81 mrad rms phase error which shows that the difference between the offset frequency and one-quarter of the repetition rate was almost zero.

A better measurement of the quality of the phase-locking loop was obtained by measuring the phase noise spectrum and then calculating the accumulated phase error. Using a dynamic signal analyzer, the power spectrum of the phase detector signal could be measured while the phase-locking loop was in operation. Recall that the phase detector signal is given by Equation 3.1 and is graphically displayed in Figure 3.18. Mathematically, the two-sided power spectral density (PSD) is given by:

$$S_{\varphi}(f) = \lim_{T \rightarrow \infty} \frac{1}{T} \left| \int_{-\frac{T}{2}}^{\frac{T}{2}} \varphi(t) \exp[i2\pi ft] dt \right|^2 \quad (3.2)$$

where  $T$  is the observation time and  $f$  is frequency and  $\varphi(t)$  is the phase detector signal. The limit is taken in the integral to avoid divergence. Experimentally, though, the one-sided PSD is measured, which is twice the value of the two-sided PSD. [43] The accumulated CE phase error can be calculated over a certain time range by integrating the one-sided PSD over frequency.

Then, the accumulated phase error, or integrated phase error as it is commonly called, is represented as:

$$\sigma_{\varphi}^2 = \int_{\frac{1}{T}}^{f_{\max}} S_{\varphi, \text{one-side}}(f) df \quad (3.3)$$

This value gives the noise of the CE phase locking loop directly. Researchers in the field define the coherence time of the CE phase locking to be the observation time at which the accumulated phase error is  $\sim 1$  rad or  $\sqrt{\sigma_{\varphi}^2} \sim 1$  rad. [44]

Ideally, the integration would be done for frequencies very close to DC all the way up to the repetition rate of the laser. However, for very high frequencies ( $>1$  MHz), the phase-locking loop is unable to compensate those errors. Also, for frequencies  $> 10^4$  Hz, the noise is on the level of the noise floor of the detection system. So, it is experimentally sufficient to measure the noise up to  $\sim 100$  kHz.

The PSD of the phase noise from the phase detector and the integrated phase error is shown in Figure 3.19.

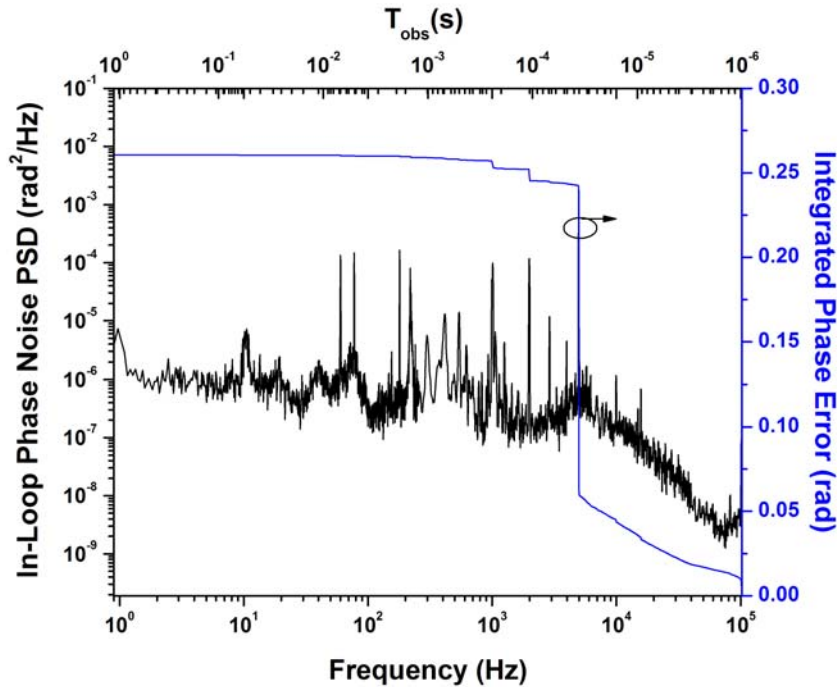


Figure 3.19 PSD of the phase detector signal (black curve) and integrated phase error (blue curve).



The above data was taken by piecing together frequency spans that approached DC. This required the offset frequency to be locked over 3 hours as the spans close to DC took almost an hour to accumulate the required time samples. The accumulated phase error for the longest observation time measured was  $\sim 260$  mrad for 1 s of observation time. Much of the low frequency noise was mechanical noise from the optical mounts in the oscillator and interferometer used for phase locking. The peak at  $\sim 1$  kHz was most likely from small back reflections from the Pockels cell, which picked a 1 kHz pulse train from the 76 MHz oscillator pulse train. The noise, though, began to roll off near  $10^4$  Hz.

This phase noise measurement, though, represents a good stability of the phase-locking system employed. Compared to other groups, this noise is lower. For example, in [45], who used a prism-based laser, the integrated phase error was  $\sim 1$  rad for a measurement time of 1 s. Actually, prism-based lasers have been found to be noisier than mirror based lasers, since beam pointing effects are much more severe in those lasers. Pointing jitter leads to variations in the offset frequency and thus the CE phase.

An improvement to the measurement in Figure 3.19 would be to measure the out-of-loop phase noise. An out-of-loop measurement is a measurement of the real phase noise. The in-loop measurement is involved in the stabilization process. Any error occurring in the in-loop measurement would be written onto the CE phase of the pulses leaving the cavity of the laser oscillator. Thus, by measuring the out-loop measurement, the variations could be seen. However, a secondary  $f$ -to- $2f$  interferometer and PCF were not available for the measurement.

Another improvement would be to measure the unlocked phase noise. By comparing the locked and unlocked phase noises, the frequencies actually suppressed by the phase-locking loop would be known and a better estimate of the phase-locking bandwidth could be determined. However, this was not possible with the Menlosystems electronics since the phase detector wrapped the phase.

### **3.5 Noise of the Oscillator CE Phase Locking Interferometer**

In order to maintain a CE phase stable laser system, all sources of CE phase noise must be controlled. In Reference 17, the effect of the phase noise of the  $f$ -to- $2f$  interferometer used for stabilizing the CE phase of the laser oscillator was studied. In the experiments, a Helium-Neon

(He-Ne) laser, operating at  $\sim 632$  nm, was copropagated with the light in the  $f$ -to- $2f$  interferometer. [17]

The experimental setup is shown in Figure 3.20. A half-waveplate was added after the HeNe laser to adjust the intensity of the beam as it passed through the interferometer since the optics were not designed for the 632 nm wavelength. Also, a lens was used to loosely focus the beam in order to counteract the lenses in the top arm of the interferometer. The position of the lens could be adjusted to give the beams emerging from the interferometer roughly the same diameter. As the laser propagated through the interferometer, any variation of the path length caused interference between the beams from the two arms. [17]

After the HeNe beams traversed the interferometer, they were bounced off of the grating and sent to two locations. First, a CCD camera captured the interference pattern formed by the two beams. Second, a photodiode measured the intensity of a single fringe of the interference pattern. The single fringe was obtained by using two cylindrical mirrors and a slit. A later version of the interference setup took away the cylindrical mirrors and used the center of the circular (collinear) interference pattern. Both setups provided the same information.

The signal from the photodiode was sent to a PID controller (SIM960, Stanford Research Systems). The PID controller provided an output voltage, which was applied the PZT attached to the mirror in the top arm of the interferometer. [17]

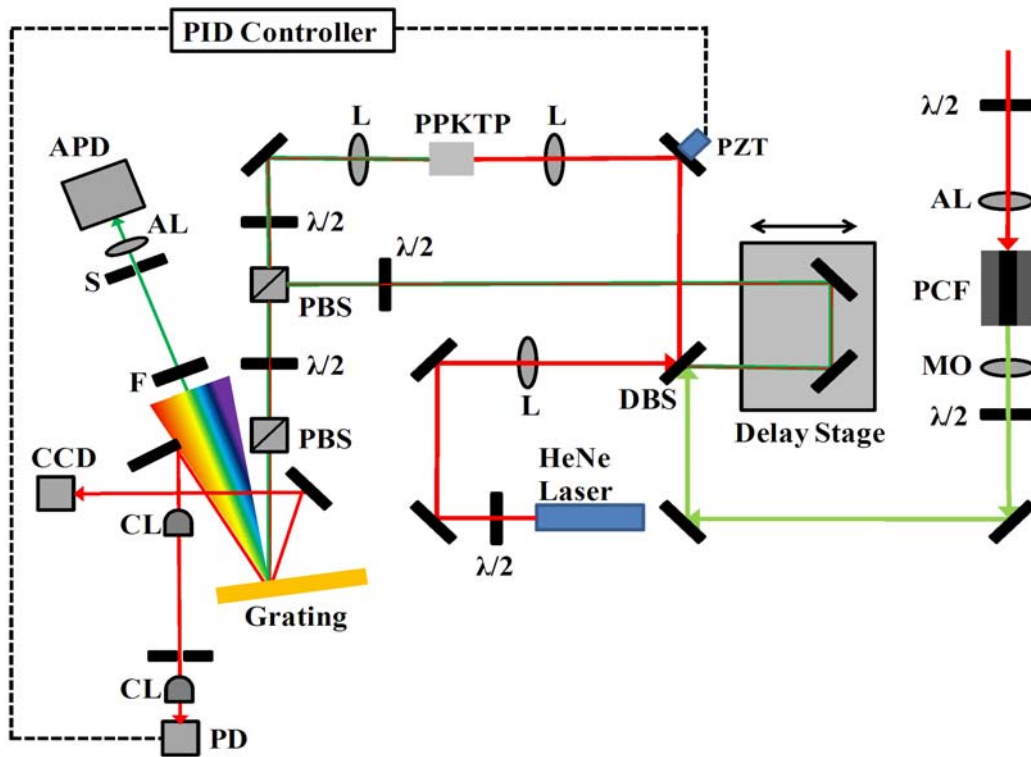


Figure 3.20  $f$ -to- $2f$  with a HeNe laser. CL: cylindrical-lens, PD: photodiode, CCD: camera.

An example of the fringes obtained from the CCD camera for the locked and unlocked cases is shown in Figure 3.21.

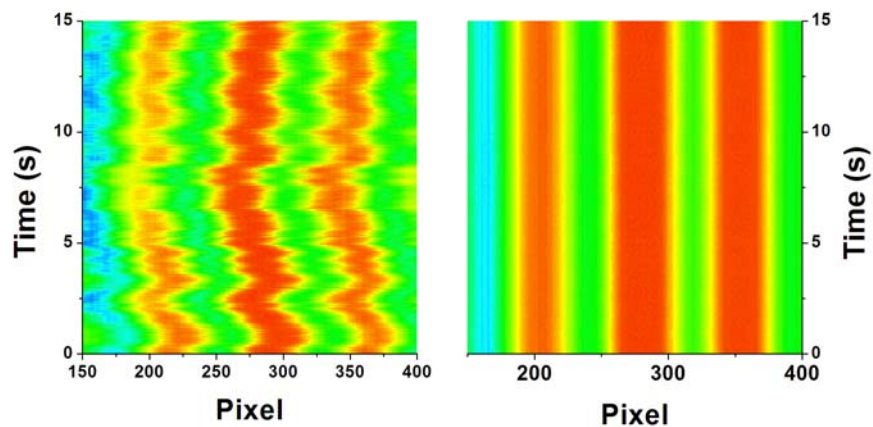
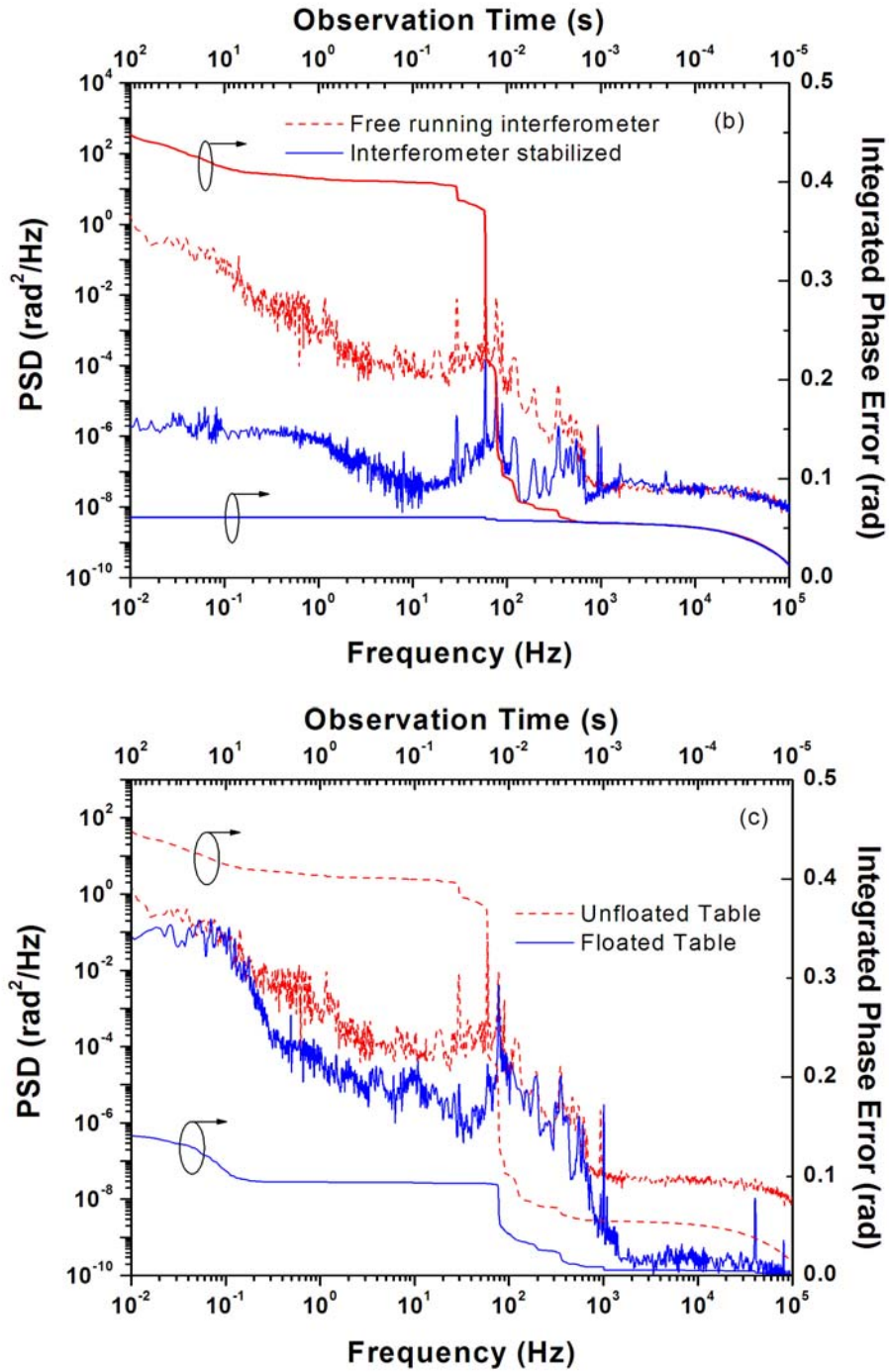


Figure 3.21 HeNe fringes. Left) unlocked, Right) locked.

The figure shows that when the interferometer was locked, the fringes did not jitter unlike as in the unlocked case. To measure the phase stability of the interferometer quantitatively, the signal from the photodiode was sent to a dynamic signal analyzer. Using the analyzer, the phase noise, similar to that measured for the oscillator CE phase, was measured. The results are shown in Figure 3.22.

In the figure, the majority of the noise is present from DC to  $\sim 1$  kHz. This noise presumably originated from air flow variations and vibrations of the optical table. When the locking servo was engaged, the noise was significantly reduced within that range. The dominating noise peak at 100 Hz was reduced by almost two orders of magnitude. It should be noted that the optical table was not floated when the top figure was measured. [17]

The effect of floating and unfloating the table is shown in the bottom figure. In the measurement, the locking servo was not engaged. This measurement shows the passive stability of the interferometer. When the table was floated, the high frequency ( $>1$  kHz) noise of the interferometer was reduced by almost two orders of magnitude. The low frequency noise in the range of  $\sim 500$  mHz to 100 Hz was reduced by 1 order of magnitude to 2 orders of magnitude for some frequencies. A possible reason that the low-frequency noise was not so affected for certain frequencies by floating the table was that certain noise sources were attached to experimental setups along the table. Vibration sources such as vacuum pumps, power sources, and computers could still couple to the table to some degree. The results could be improved by isolating all of those noise sources further and locking the interferometer. [17]



**Figure 3.22 Top) The power spectrum of the interferometer phase noise and the integrated phase error. Bottom) Comparison of phase noise measurements when the optical table was floated and unfloated.**

In the interferometer, any vibration of the mirror mounts or temperature or pressure variations will lead to time dependent path length,  $\Delta L(t)$ . Thus, the relative phase of the beams

in the two arms of the interferometer becomes time-dependent. The time dependent phase is given by  $\varphi(t) = 2\pi \frac{\Delta L(t)}{\lambda}$ . In this case, the wavelength is 532 nm. [17]

The bottom arm of the interferometer is chosen as the reference beam. The electric field of the beam is given by:

$$E_1(t) = E_{0,1}(t) \cos[2\pi(mf_{rep} + f_0)t] \quad (3.4)$$

where  $E_{0,1}$  is the amplitude and  $m$  is the mode-index determined by the wavelength. The electric field of the second harmonic of the infrared light in the top arm of the interferometer is given by:

$$E_2(t) = E_{0,2}(t) \cos[2\pi(mf_{rep} + 2f_0)t + \varphi(t)] \quad (3.5)$$

The frequency of the detected offset frequency will be deviated from its true value and will also become time-dependent.

$$f(t) = f_0 + \frac{1}{2\pi} \frac{d\varphi}{dt} \quad (3.6)$$

The CE phase locking electronics stabilize  $f$ , which is detected by the APD in the interferometer. If the detected offset frequency fluctuates, then the CE phase of the pulses leaving the oscillator will fluctuate. Thus, it is important to reduce the noise from the  $f$ -to- $2f$  interferometer. [17]

# CHAPTER 4 - CE Phase Stabilization of Amplified Laser Pulses

## 4.1 Background

Once CE phase stabilization had become a viable technology for Ti:Sapphire laser oscillators, the next step was to consider the CE phase stability through the amplification process. Ti:Sapphire laser oscillators generally produce pulses with nJ level energy. However,  $\mu\text{J}$  to mJ energy pulses are needed for exploring the majority of physical processes sensitive to the CE phase. For example, HHG and ATI require laser intensities  $\sim 10^{14} \text{ W/cm}^2$ . [3,1] In this section, the background of amplifying CE phase stable pulses will be briefly reviewed.

The first paper published on amplifier CE phase was in 2000 [46]; shortly after the first few papers on CE phase stabilization of laser oscillators was published. The paper suggested a method for obtaining the CE phase using amplified laser pulses by overlapping the second and third harmonics of the laser. However, the method was never implemented due to experimental complexities. [46] In 2001, though, a major paper was published which outlined the method of measuring the pulse-to-pulse change in CE phase by spectral interferometry and displayed its implementation. [47] The method involved  $f$ -to- $2f$  interferometry with the low repetition rate pulse train from the amplifier. Basically, the CE phase changes could be measured by overlapping the delayed superposition of the fundamental and second harmonic pulses, where the second harmonic overlapped in frequency with the fundamental. This method is very similar to that used for stabilizing the CE phase of the laser oscillator. [47] Also, it should be noted that the method is used by almost all groups even to this day for measuring the pulse-to-pulse CE phase drift. The method will be outlined in more detail in section 2 of this chapter.

The aforementioned method was used to measure the CE phase drift of the amplified pulses in Reference 48. [48] It was found that the CE phase drift gave a random distribution. The authors concluded the random distribution was due to the fact that they were using a non-CE phase stabilized oscillator to seed their amplifier. This group was also the first to address sources of CE phase fluctuations through the amplifier, especially the gratings in the stretcher and compressor. [48]

In 2003, the first demonstration of a CE phase stabilized amplifier was reported by Baltuška et al. [16] This group used a CE phase stabilized Ti:Sapphire laser oscillator to seed an amplifier equipped with a glass block stretcher and a prism-based compressor. They then used

the method in Reference 47 to measure the CE phase drift of the amplified pulses and used that signal to pre-compensate the drift in the oscillator phase-locking loop. The CE phase stabilize pulses were then used to investigate CE phase effects in HHG and ATI. [49]

In 2004 thru 2006, groups were involved in scaling the CE phase stabilized amplifiers to higher energies, which could be accomplished only by using grating-based stretchers and compressors. Material-based stretchers and compressors would not be able to withstand the multi-mJ energy level pulses desired from such systems. A major paper published in 2004 involved the regenerative amplification of a CE phase stable pulse train. [45] In this work, the amplifier employed grating-based stretchers and compressors. The group concluded that the gratings did not destroy the CE phase coherence through the amplifier. This was confirmed by measuring the CE phase stability using the method in Reference 47.

Much of the research up until the present time has followed the same path. Today, CE phase stable grating-based chirped-pulse laser systems are the state of the art and capable of producing several mJ energy per pulse. The research detailed in the remaining chapters of this thesis will address the amplification of CE phase stable pulses.

## **4.2 Experimental Methods**

### ***4.2a Chirped-Pulse Amplification***

As was said in the introduction, the nJ energy pulses from laser oscillators require amplification in order to explore the majority of physical processes sensitive to the CE phase. The pulses from laser oscillators are usually  $\sim 10$  fs in duration. Since the gain of the amplification system must be  $\sim 10^6$  to reach mJ energies, the peak intensity in the laser crystal would be enough, after several passes, to damage the crystal. Thus, another method needed to be employed to amplify the laser pulses.

The method, which was developed in 1985 by Strickland and Mourou, is called chirped-pulse amplification (CPA). [50] In this method, the pulses are stretched in time, amplified, and then temporally compressed. To amplify pulses from Ti:Sapphire laser oscillators, the pulses are usually stretched from  $\sim 10$  fs to  $\sim 100$  to 200 ps. A schematic of a CPA laser system is shown in Figure 4.1.



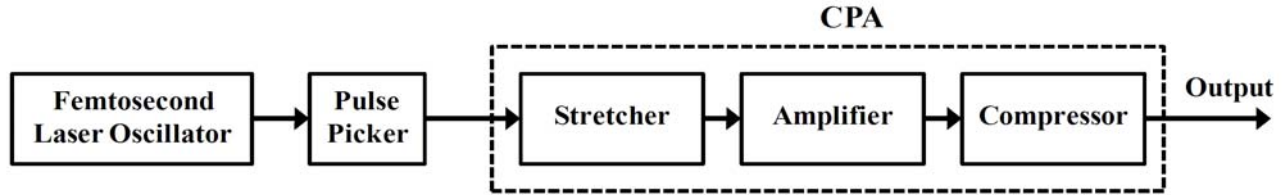


**Figure 4.1 CPA laser system.**

In a CPA system producing femtosecond pulses, the MHz repetition rate pulse train from a laser oscillator is counted down to the kHz or Hz level by a pulse picker. The pulses then enter the stretcher. The stretcher is either material-based or grating-based. For the material-based stretcher, the pulses are stretched by traversing a glass block or by a prism-stretcher arrangement. In the grating-based stretcher, the pulses are stretched by a pair of gratings combined with a telescope arrangement. Single-grating designs also exist. In both the material and grating cases, though, the pulses are stretched to  $\sim 100$  ps or more, depending on the design parameters of the amplifier. [50]

Once the pulses leave the stretcher, they enter the amplification stage of the CPA system. Two arrangements of amplifiers exist for femtosecond Ti:Sapphire lasers. The first configuration is a multi-pass setup. In this design, the separate passes through the crystal are separated geometrically. The number of passes through the crystal is determined by the desired output energy and of the complexity of the setup. In order for the gain to be high for each pass through the crystal, the crystal is pumped close its damage threshold. [51]

The second configuration used is called a regenerative amplifier. In this design, the pulses are amplified in a cavity. The pulses are trapped in the cavity by polarization techniques, amplified until the energy in the laser crystal has been fully extracted, and then sent out of the cavity by changing the polarization of the laser pulse.

Both amplifier designs, though, are capable of producing the mJ energy pulses for exploring high field physics. Often, the two amplifier configurations are used in tandem to produce very high energy pulses. Also, cascaded multi-pass amplifiers are often used to produce high power pulses. [51]

However, once the pulses have been amplified using either of the aforementioned methods, the pulses are sent to a compressor. Similar to the stretcher, the compressor is either material-based or grating-based. The compressor must compensate for the dispersion from the stretcher and from the amplifier. A material-based compressor would consist of either two pairs of prisms or a double-pass prism pair (pair of prisms followed by a retroreflector). Then, the grating-based compressor would consist of two gratings separated by an adjustable distance. Again, the grating-based systems can handle more energy than the material-based systems.

The amplification process, though, is not completely linear. The original pulse duration cannot be recovered by the compressor after the pulse has been amplified. This is due to gain narrowing during the amplification process. Even though the input pulse spectrum can be supported by the laser crystal, the effective gain spectrum is narrower due to higher amplitude frequencies in the input laser spectrum experiencing higher gain. The lower amplitude frequencies are suppressed through each pass, leading to a narrowing of the laser spectrum. [51] Thus, the pulses from the CPA are longer than the input pulses from the oscillator. Typically, for input pulses  $\sim 12$  fs, the transform-limited pulses obtained from the CPA are around 30 fs or longer. [51]

In order to study physical processes sensitive to the CE phase, the pulses must be short, approaching the few-cycle regime. For an experiment involving stereo ATI, for example, the pulses must be  $< 8$  fs. [1] Thus, the pulses from the amplifier must be shortened. Also, the CE phase stability must be maintained.

#### ***4.2b CE Phase and Few-Cycle Pulses***

A typical setup for generating few-cycle, high intensity, CE phase stable pulses is shown in Figure 4.2.

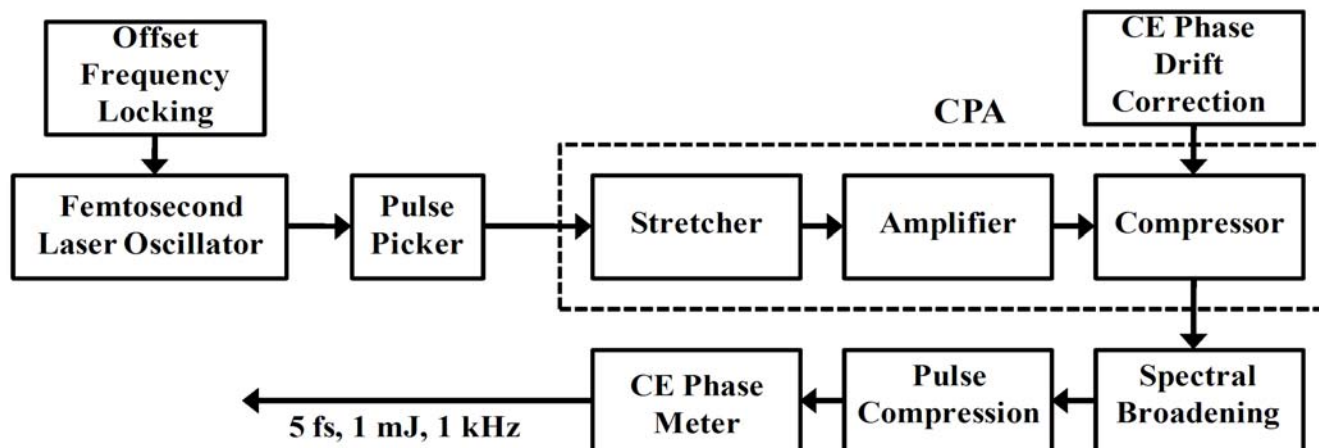


**Figure 4.2 Laser system for generating high-intensity, few-cycle, CE phase stable pulses.**

In order to produce the 5 fs, 1 mJ, 1 kHz repetition rate laser pulses, several steps need to be followed. First, the offset frequency of the nJ energy and MHz repetition rate laser oscillator is locked to a known value, stabilizing the evolution of the CE phase from pulse-to-pulse. This was covered in chapters 2 and 3. Then, a pulse picker such as a Pockel’s Cell is used to pick out a kHz pulse train from the MHz oscillator pulse train. Very importantly, the timing of the pulse picker is adjusted such that the picked pulse train consists of pulse with the same CE phase. This is usually done by synchronizing the pulse picker and the CE phase locking electronics. The CE phase stable pulse train is then directed to the CPA and amplified to several mJ in energy. As was discussed in the first section, the pulse duration of the pulse after the compressor is usually around 30 fs or greater.

The stretching, amplification, and compressing processes all add drift to the CE phase of the kHz pulse train. Thus, the drift of the CE phase of the amplified pulses is measured and corrected by either feeding back to the oscillator locking electronics or by adjusting the grating separation in either the stretcher or compressor. This aspect of producing CE phase stable pulses will be discussed in the next two sections.

To shorten the laser pulses to the few-cycle duration, some method of spectral broadening is used followed by temporal compression. The common method is to propagate the laser pulses through a hollow-core fiber filled with a noble gas such as Argon or Neon. [10] Another method

is to focus the laser pulses into a chamber, not a fiber, filled with a noble gas and create a filament. [13] Both methods take advantage of self-phase modulation. Self-phase modulation is similar to the Kerr Effect as it is nonlinear and occurs for high intensities. Basically, since the index of refraction can be written as  $n(t) = n_0 + n_2 I(t)$ , the laser will experience an extra phase shift of  $\Delta\varphi(t) = \frac{2\pi n_2 I(t)L}{\lambda}$  after traversing a medium of length  $L$ . Since frequency is the time derivative of phase, the extra phase shift will yield new frequencies. [52] This is done experimentally by exploiting the nonlinearity of the medium.

Once the pulses had been spectrally broadened, the dispersion added to the pulses is compensated. Usually, chirped mirrors are used as they are readily available and relatively simple to implement experimentally. They do have drawbacks though as the chirped mirrors can only compensate a fixed amount of dispersion. Also, the chirped mirrors can only compensate second-order dispersion. Another method exists in which the dispersion is compensated using an adaptive pulse shaper. This method can compensate all orders of dispersion and reach the transform limit. The drawback with this method is that the setup is lossy. [15]

However, once the pulses have been compressed to a few-cycles, the CE phase stability must be measured as the fiber or filamentation setups can add CE phase drift to the pulses. This can be accomplished by measuring the CE phase shift using the same method as was used after the CPA by performing a physics experiment such as ATI. [1]

In the next section, the method for measuring the CE phase drift of amplified laser pulses is discussed.

#### ***4.2c f-to-2f Spectral Interferometry***

As was stated before, the CE phase stability of the pulses exiting the amplifier must be measured and corrected in order to perform experiments. As the pulses traverse the amplifier, fluctuations in intensity, mechanical drifts, and thermal drifts will cause the CE phase to drift. In order to measure the CE phase stability of the pulses, an *f-to-2f* method, similar to that used for the oscillator pulse train, can be employed. This method was first proposed and experimentally realized by M. Kakehata et al. [47]

In this method, the laser pulses from the amplifier with a narrow spectral width are focused into a nonlinear medium. Usually, a sapphire plate or hollow-core fiber filled with a

noble gas is used. Once focused into the medium, the pulses undergo self-phase modulation and are broadened over an octave in spectrum. This is necessary, as it was for the oscillator pulses, because the  $f$  and  $2f$  components will be overlapped. The situation is shown in Figure 4.3.

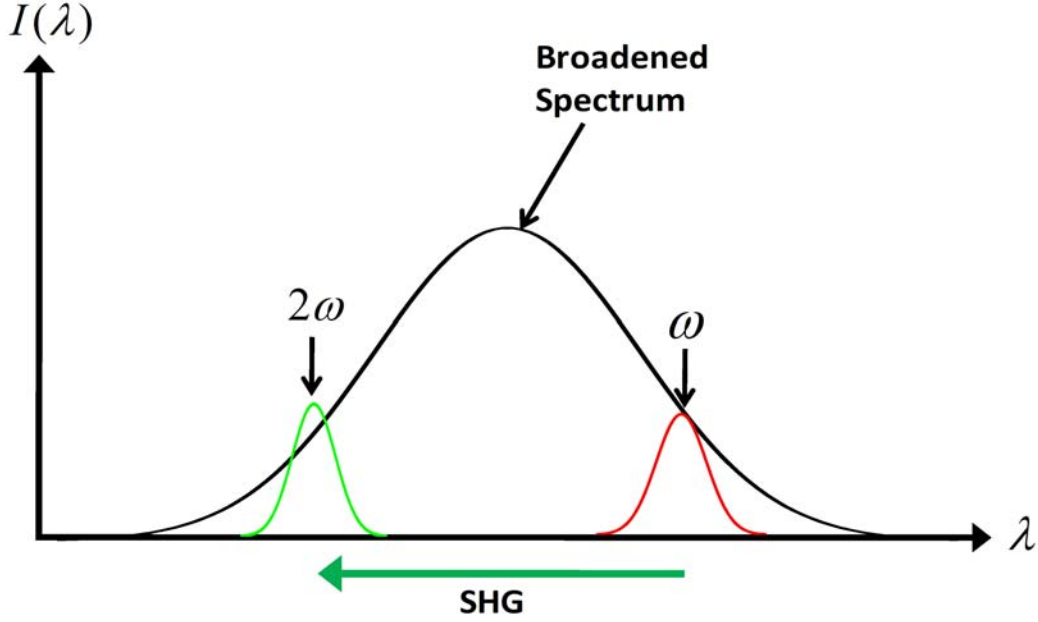


**Figure 4.3  $f$ -to- $2f$  interferometry for the amplified laser pulses.**

In the figure, the low frequency (long-wavelength)  $\omega$  components of the broadened spectrum are frequency-doubled and overlapped with the high frequency (short-wavelength)  $2\omega$  components. Unlike in the oscillator  $f$ -to- $2f$  self-referencing technique, the delay between the  $\omega$  and  $2\omega$  components is not set to zero. Also, a broader spectrum is used.

The interference of the components in the frequency domain can be expressed as:

$$I(\omega) \propto I_{WL}(\omega) + I_{SHG}(\omega) + 2\sqrt{I_{WL}(\omega)I_{SHG}(\omega)} \cos(\omega\tau_0 + \phi_{SHG}(\omega) - \phi_{WL}(\omega) + \phi_{CE}) \quad (4.1)$$

where  $I_{WL}(\omega)$  and  $I_{SHG}(\omega)$  are the intensities of the broadened spectrum (white-light) and the second harmonic respectively.  $\tau_0$  is the delay between the second harmonic and white-light pulses.  $\phi_{SHG}(\omega)$  and  $\phi_{WL}(\omega)$  are the spectral phases of the second harmonic and white-light respectively. The resulting interference pattern, given by Equation 4.1 gives information on the delay between the pulses and the CE phase. [16] The interference pattern will look similar to Figure 4.4.

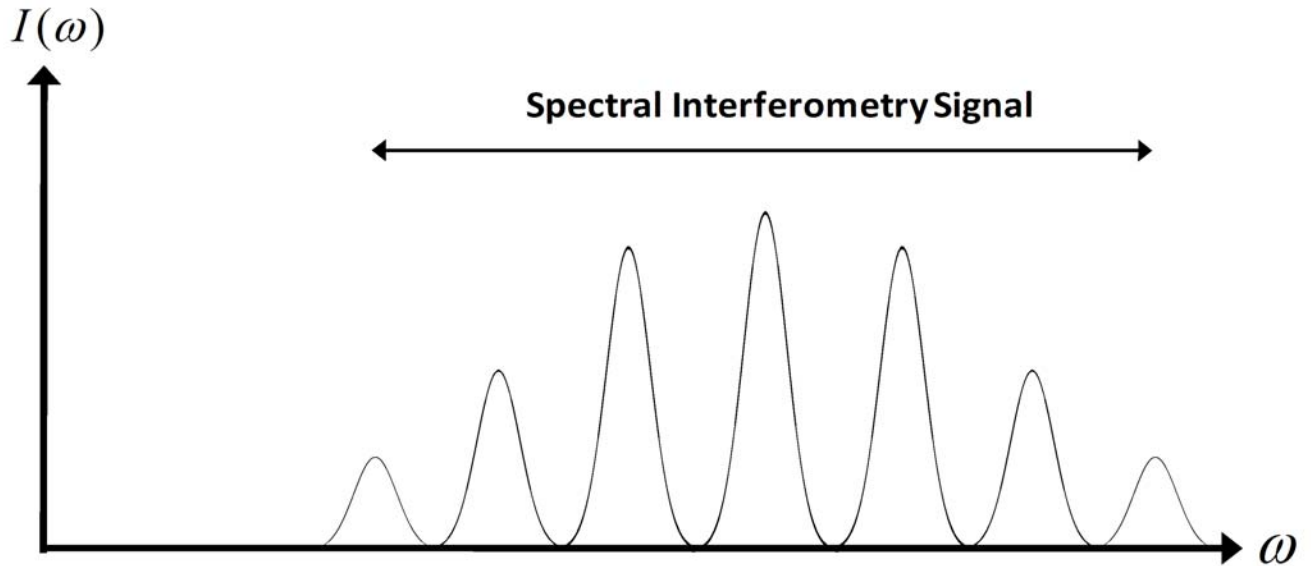


**Figure 4.4 Spectral interferometry signal.**

The above figure is similar to that which would be detected by a spectrometer. In practice, the fringe pattern usually covers  $\sim 30$  nm in wavelength.

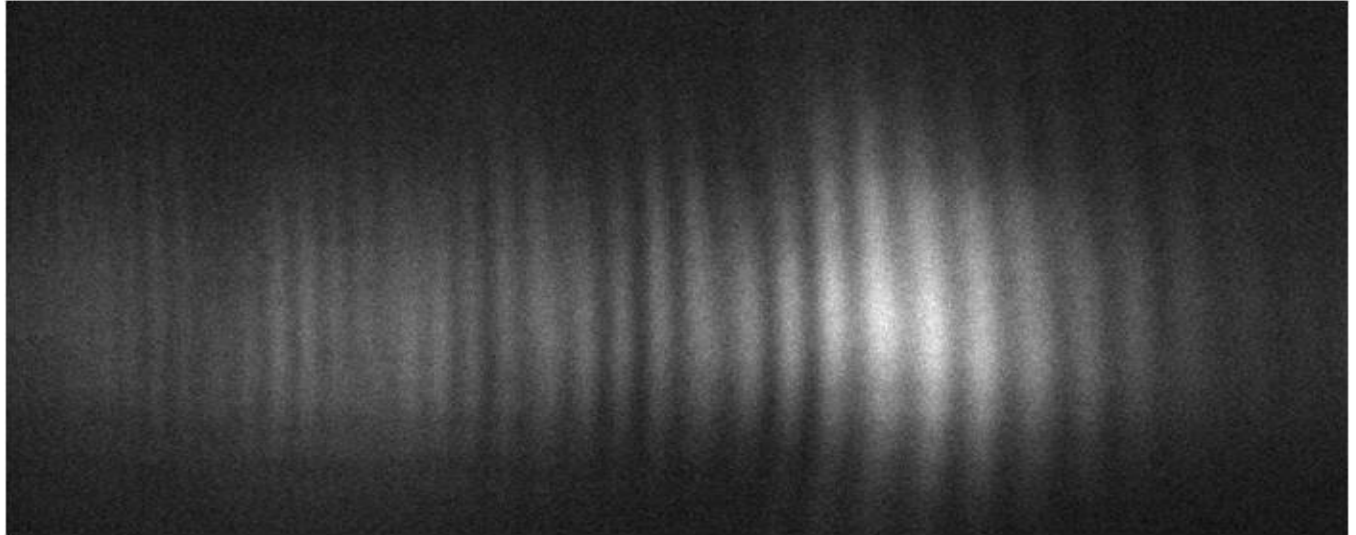


**Figure 4.5 Example of an experimental interferogram.**

The fringe pattern is easy to see in this figure. This is an example of what is obtained in the laboratory. The bright and dark bands show the modulation. The fringe pattern can be used

to obtain the pulse-to-pulse shift of the CE phase using a well-known algorithm called Fourier Transform Spectral Interferometry. [53]

The first step in the method is to take the inverse Fourier transform of the spectral interferometry signal to obtain the delay between the second harmonic and white-light pulses. The negative delay term and the DC terms are then filtered out. This is represented in Figure 4.6.

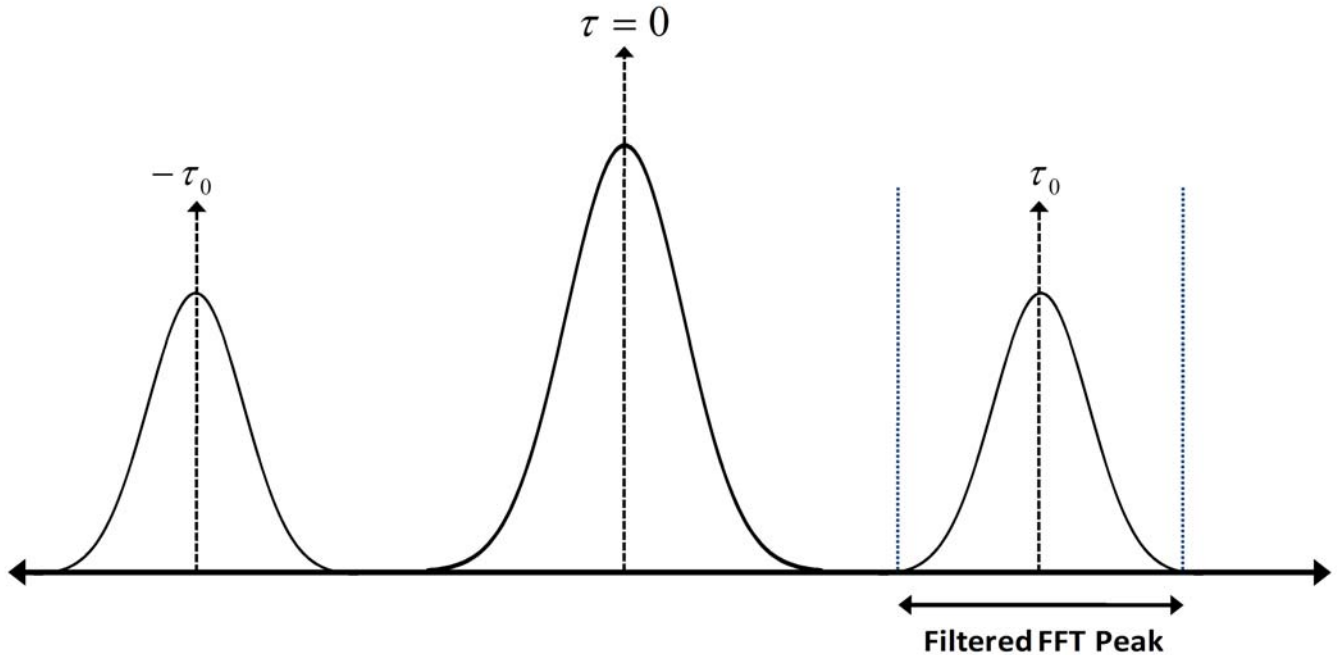


**Figure 4.6 FFT Peak from the spectral interferometry signal.**

The width of the peak determines the regularity of the fringe spacing. This can be understood by considering the ideal case where the interference is of the form  $A(1 + \cos(\omega\tau))$ , where  $A$  represents a DC term. The Fourier transform of such a function yields three delta functions: one for the positive delay, one for the negative delay, and one for the DC terms. In practice, though, the delay peaks exhibit some width, which indicates some irregularities in the fringe spacing. Practical values of the delay are usually hundreds of femtoseconds to  $\sim 1$  picosecond. This depends on the optical setup used to obtain the interference signal. For example, the setup to be described in the next chapter uses a 2.3 mm thick sapphire plate and a mm thick BBO crystal to obtain the white-light and second harmonic respectively. A typical value of delay from that setup is  $\sim 300$  fs.

The rest of the FTSI algorithm proceeds from the point the delay peak is chosen. A schematic of the algorithm is shown in Figure 4.7.

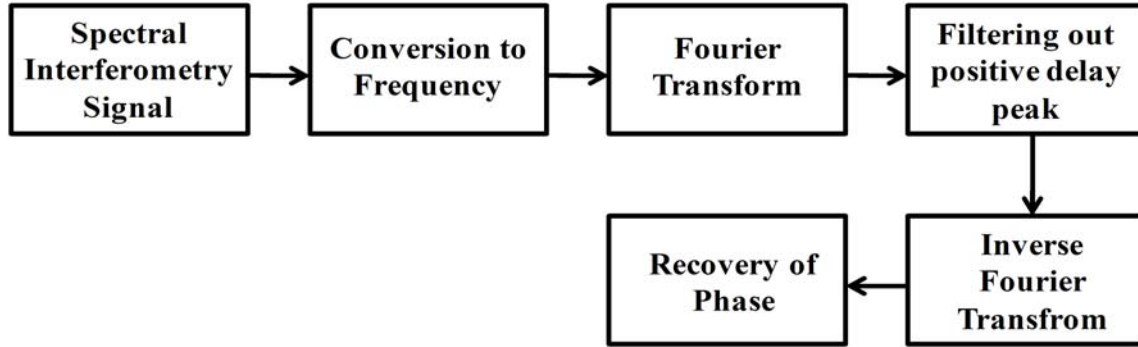


**Figure 4.7 FTSI Schematic**

Starting from the point where the positive delay peak is filtered out, the Fourier transform is taken back to the frequency domain. Here, the phase, which is the argument of the cosine in Equation 4.1, is recovered and unwrapped to remove discontinuities. [54]

This method, in principle, could measure the CE phase. However, in order to accomplish that, all phase shifts due to the propagation of the pulses through the second harmonic generating crystal would need to be known. Thus, it is not possible to measure the CE phase. The usefulness of the method, though, is in measuring the CE phase shift.

In the measurement of the phase, as long as intensity fluctuations of the input laser pulses is small, the delay and spectral phases of the white-light and second harmonic can be assumed to be constant during the measurement. This is not always true and will be addressed in a later chapter. However, assuming this condition, the total phase obtained from the spectral interferometry signal can be written as:

$$\Phi(\omega) = \omega\tau_0 + \phi_{CE} + \delta\phi(\omega) \quad (4.2)$$

where  $\delta\phi(\omega)$  represents the phases of the white-light, second harmonic, and any other static phase shifts. Then, the relative phase drift between the 0<sup>th</sup> pulse to the  $i^{\text{th}}$  pulse can be represented as:

$$\Delta\Phi = \Phi_i - \Phi_0 = \Delta\phi_{CE} \quad (4.3)$$

Thus, equation 4.3 shows that the relative phase drift is equal to the CE phase shift from pulse-to-pulse. As was mentioned, this assumes the following conditions: 1)  $\tau_i = \tau_0$ , and



2)  $\delta\phi_i(\omega) = \delta\phi_0(\omega)$ . [54] Experimentally, the CE phase shift is measured over a frequency range in which the delay has a constant value.

Finally, it should be noted that it is not possible to employ this method for the oscillator pulse train. In principle, it would give you information on the CE phase; however, the repetition rate of laser oscillators is too fast. It is an experimental impossibility to measure the pulse-to-pulse variation of the fringe pattern. This method can only be used for lower repetition rate amplifiers.

# CHAPTER 5 - Stabilization and Control of the CE Phase using the KLS Amplifier

## 5.1 The KLS Amplifier

As was discussed in chapter 3, the KLS laser oscillator emits 5.6 nJ, ~12 fs pulses at a repetition rate of ~76 MHz. In order to explore physical processes sensitive to the CE phase in the KLS laboratory, those pulses are amplified to the mJ level using the KLS amplifier. [55] The amplifier is outlined in Figure 5.1.

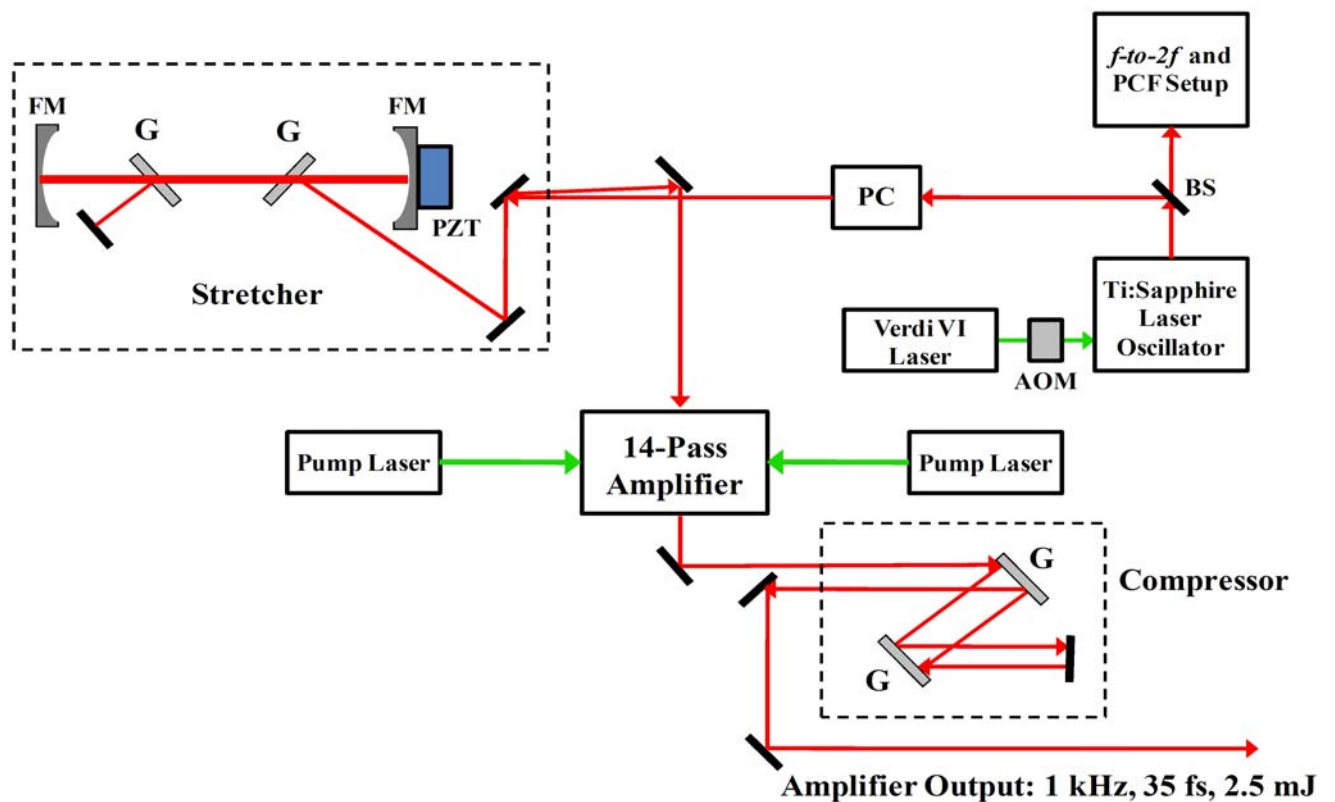


**Figure 5.1 KLS Amplifier:** BS: beamsplitter, AOM: acousto-optic modulator, PC: Pockel's cell, FM: focusing mirror, PZT: piezo-electronic transducer, G: grating

In the diagram, the pulses from the oscillator were split by a 50:50 beamsplitter. Half of the output went to the  $f$ -to- $2f$  and PCF setup, while half went through the Pockel's cell, which selected a kHz pulse train from the MHz pulse train. The pulses then entered the double-pass stretcher, where a pair of gratings and two mirrors, which acted as a telescope, stretched the

pulses to  $\sim 80$  ps. The pulses then entered a 14-pass amplifier pumped by two Q-switched ND:YLF lasers. The Ti:Sapphire crystal was cooled by liquid nitrogen to prevent thermal lensing. After the 14 passes, the pulses had energy of 5 mJ. A double-pass compressor consisting of two gratings compressed the pulses to  $\sim 35$  fs. The efficiency of the compressor was  $\sim 50\%$ , so the output pulses had energy of 2.5 mJ. Note that the original pulse duration, which was  $\sim 12$  fs, of the oscillator pulses could not be recovered due to gain narrowing in the amplifier. The spectrum of the amplified pulses is shown in Figure 5.2.

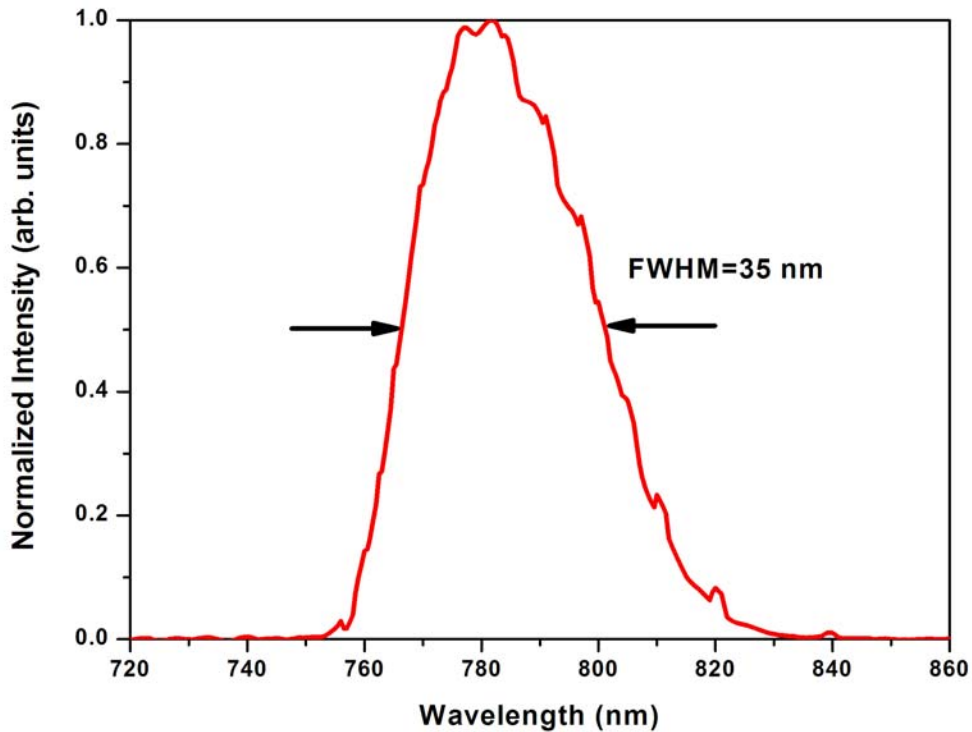


**Figure 5.2 Spectrum of the amplified pulses.**

This spectrum is much narrower than the oscillator pulse spectrum, which was shown in Figure 3.2. Again, gain narrowing in the Ti:Sapphire crystal reduced the spectrum. However, the spectrum is still broad enough to support  $\sim 35$  fs pulses.

In order to select a pulse train in which every pulse had the same CE phase, the timing of the laser was adjusted so that every fourth pulse from the MHz pulse train was selected. This was done, since the offset frequency of the oscillator was locked to one-quarter of the repetition

rate giving every fourth pulse the same CE phase. The timing of the system is shown in Figure 5.3.

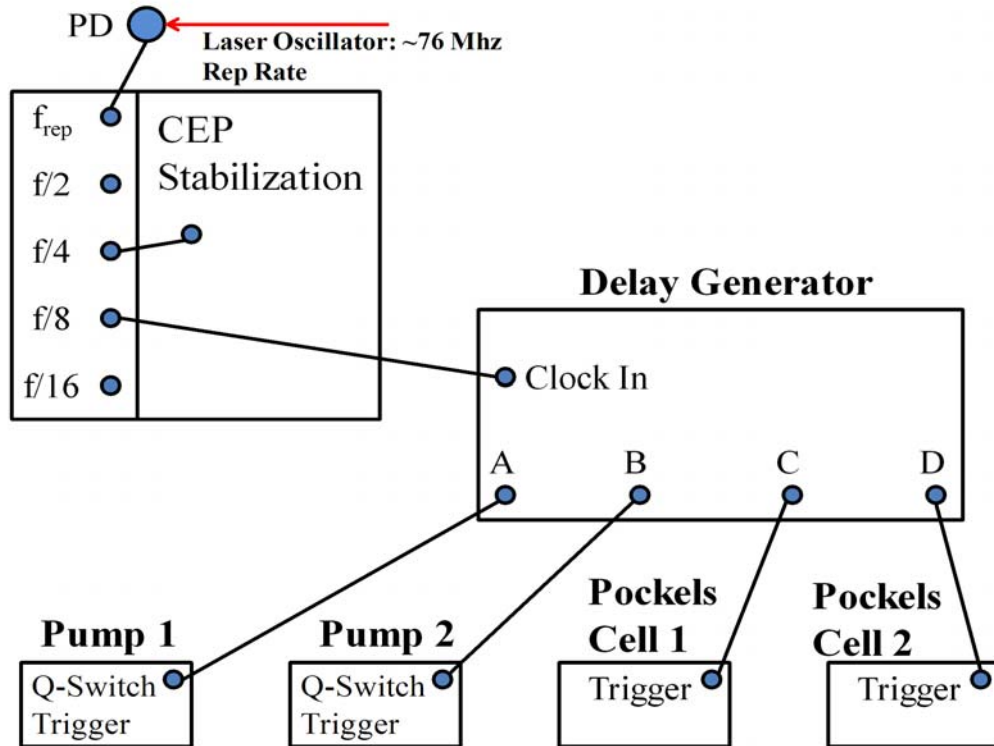


Figure 5.3 KLS laser timing.

A photodiode was used to detect the repetition rate of the oscillator pulse train. This signal was fed to the Menlosystems locking electronics. The  $f/4$  signal was used to lock the offset frequency while the  $f/8$  signal was used as the master clock for the amplifier timing. This signal was sent to a Delay Generator and was used to trigger the Pockel's cells and to trigger the Q-switching of the pump lasers. This way, the Q-switched pulses from the pump lasers arrived at the same time as the seed pulses in the Ti:Sapphire crystal in the amplifier. The Pockels cell 1 trigger was used to select the 1 kHz pulse train from the oscillator, while the Pockels cell 2 was used for pulse cleanup in the amplifier.

Even though only pulses with the same CE phase were amplified, the pulses still exhibit drift after passing through the system. Similar to the case of the laser oscillator, any changes of dispersion in the amplifier system would affect the CE phase of the laser pulses. Shifting of the

optical mounts, fluctuations in energy, and temperature changes would all contribute to CE phase drift. By measuring the CE phase drift, it could be corrected. The next section describes the experimental method for measuring that drift.

## 5.2 Measurement of the CE Phase Drift

In order to obtain the spectral interferometry signal necessary for employing the FTSI algorithm described in chapter 4, the  $f$ -to- $2f$  method is used. [61] The experimental layout for obtaining the fringes for the KLS laser pulses is shown in Figure 5.4.

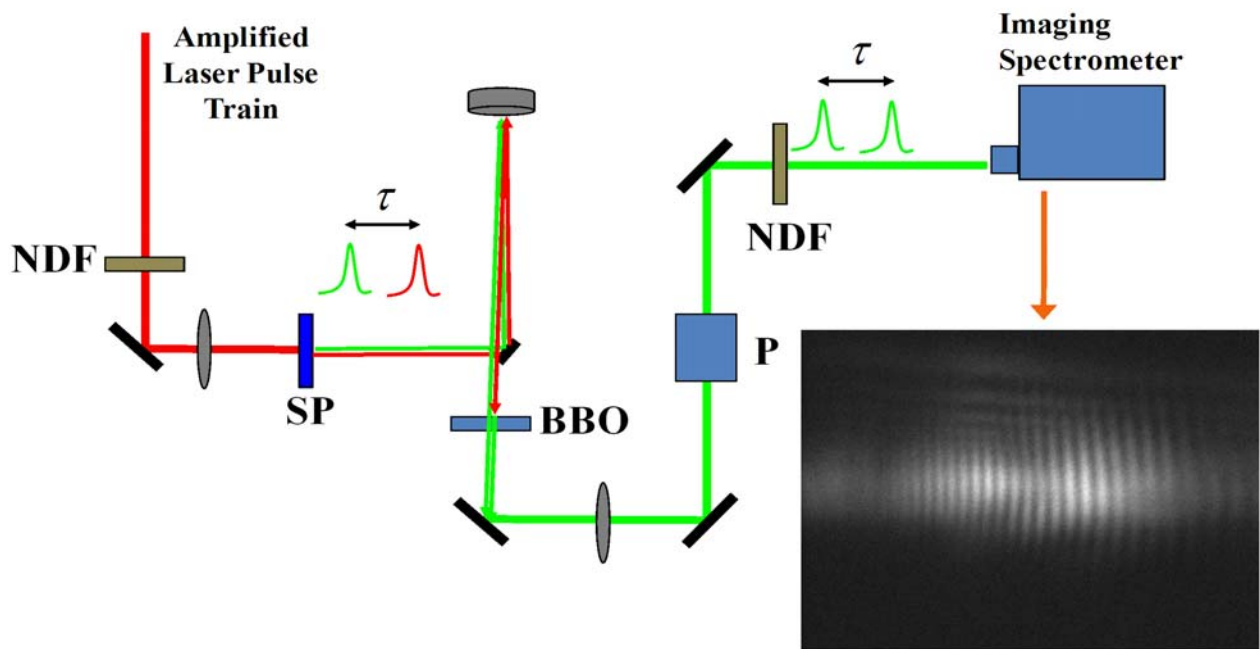


**Figure 5.4  $f$ -to- $2f$  for measuring CE phase drift: NDF: neutral density filter, SP: sapphire plate, BBO: SHG-crystal, P: polarizer,  $\tau$  : delay**

In the experimental setup, a small portion of the amplified laser pulse train ( $<1 \mu\text{J}$ ) was sent into the interferometer. The beam size was focused into the 2.3 mm thick sapphire plate by an  $f=75$  mm lens. The NDF was used to adjust the beam power in order obtain a stable single-filament inside the sapphire. The strong self-focusing in the sapphire plate broadened the spectrum of the input pulses by over an octave. Since the sapphire was birefringent, the plate

was mounted in a rotational mount in order to adjust the spectrum, similar to that done for the PCF in the case of the oscillator.

The  $f$  and  $2f$  components exhibited a delay, given by  $\tau$  in the figure, due to creation at different times during the self-focusing process and propagation through the sapphire plate. The two components were then focused by an  $f=100$  mm concave mirror into a 1 mm thick BBO crystal cut for Type-I phase matching at 1064 nm. Note that in this setup, unlike in the oscillator setup, a slightly broad second harmonic phase-matched spectrum was desirable in order to measure the CE phase drift. This is because a broader spectrum gave a better sampling of the CE phase drift across the spectrum.

Once the pulses had exited the BBO crystal, they were focused by an  $f=70$  mm lens into an imaging spectrometer after passing through a polarizer used to select a common polarization. A second NDF attenuated the beam in order not to saturate the CCD camera of the spectrometer. The image in the figure shows a typical SI signal obtained from the experimental setup.

A measurement of the white-light obtained from the sapphire-plate for different energies is shown in Figure 5.5.

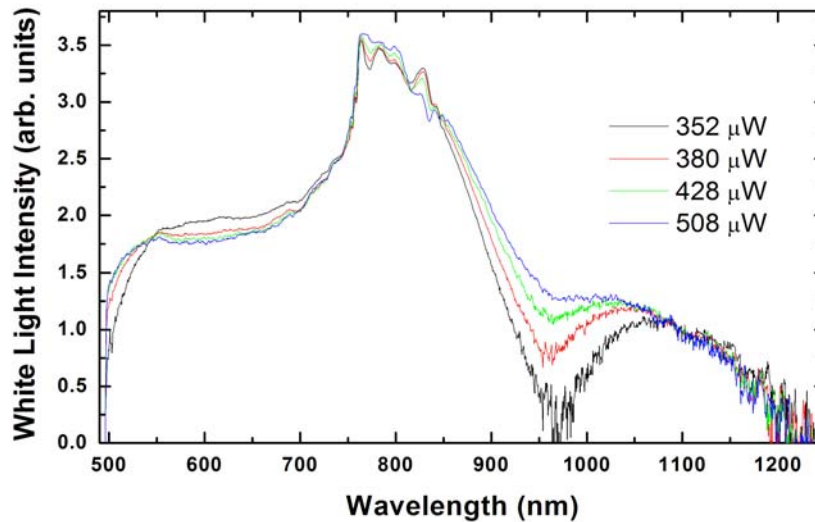


**Figure 5.5 Spectrum from the sapphire-plate at different energies.**

The spectra were obtained by scanning across the CCD of the spectrometer down to around 500 nm. As is shown, the spectra cover more than an octave. In fact, the spectrum can actually go below 500 nm to around 460 nm, depending on the axial orientation of the sapphire

plate. Typically, the *f-to-2f* measurement is carried out around a 30 nm width centered on 500 nm. Also, the pulse energy required for the generation of an octave depended on the input pulse duration. This depended on the optimization of the compressor in the KLS amplifier. If the pulse duration was long, then more energy was required, usually around 700 nJ. For an optimized compressor, the energy needed was lower, usually 300 to 500 nJ. Theoretically, the required intensity on the sapphire plate for generating the white-light was  $\sim 2 \times 10^{12}$  W/cm<sup>2</sup>. The orientation of the sapphire plate's optical axis, or equivalently the input laser polarization, would also be a factor in how much energy was required.

The experimental procedure, though, would involve an optimization of all of the aforementioned parameters. The feedback for the optimization would be the quality of the fringes obtained. The phase-matching angle would be rotated, the input power adjusted, the rotation of the sapphire plate, the rotation of the polarizer, and the position of the lens used to focus the light into the imaging spectrometer would all be adjusted until a fringe pattern with high contrast was obtained. A typical problem, though, with the optimization was that focusing too much energy onto the sapphire plate caused the formation of multiple-filaments. The multi-filamentation produced fringe patterns unusable for measurement of the CE phase drift.

Once a stable fringe pattern was obtained, though, a comparison of the CE phase drift for different integration times of the spectrometer was obtained. Since each laser pulse came every 1 ms (1 kHz repetition rate), fringe patterns for 1, 50, and 100 ms integration times were obtained when the oscillator CE phase stabilization was on and when it was disengaged. The 1 ms integration time is shown in Figure 5.6.

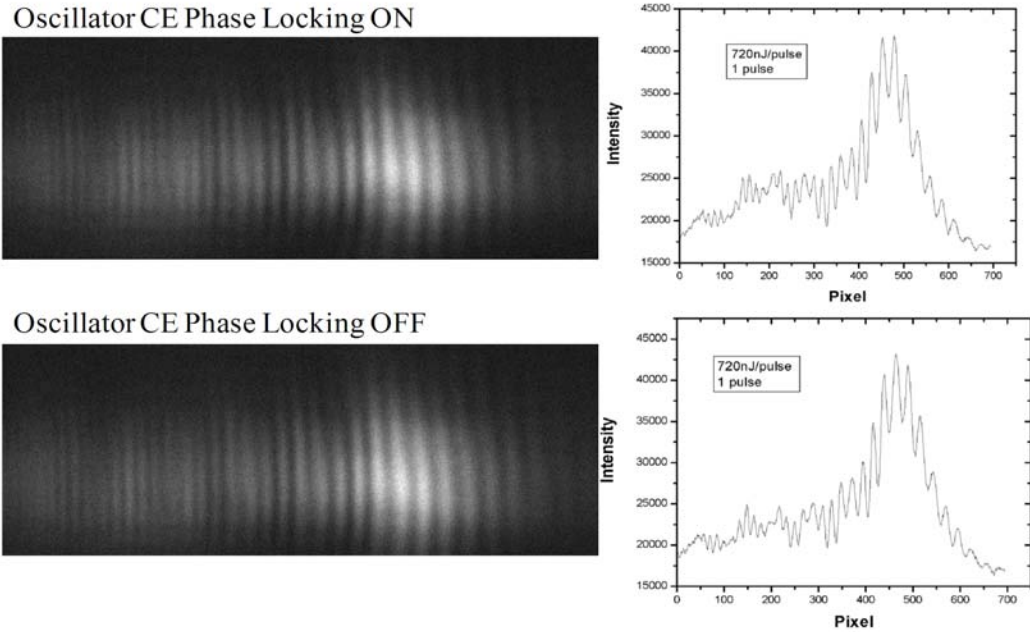


**Figure 5.6 1 ms integration time interference fringes.**

The lineouts of the fringe patterns are shown on the right. Since, for 1 laser shot, the CE phase drift is not measurable. This is why the locked and unlocked versions are not different. The 50 ms and 100 ms cases are shown in Figures 5.7 and 5.8 respectively.

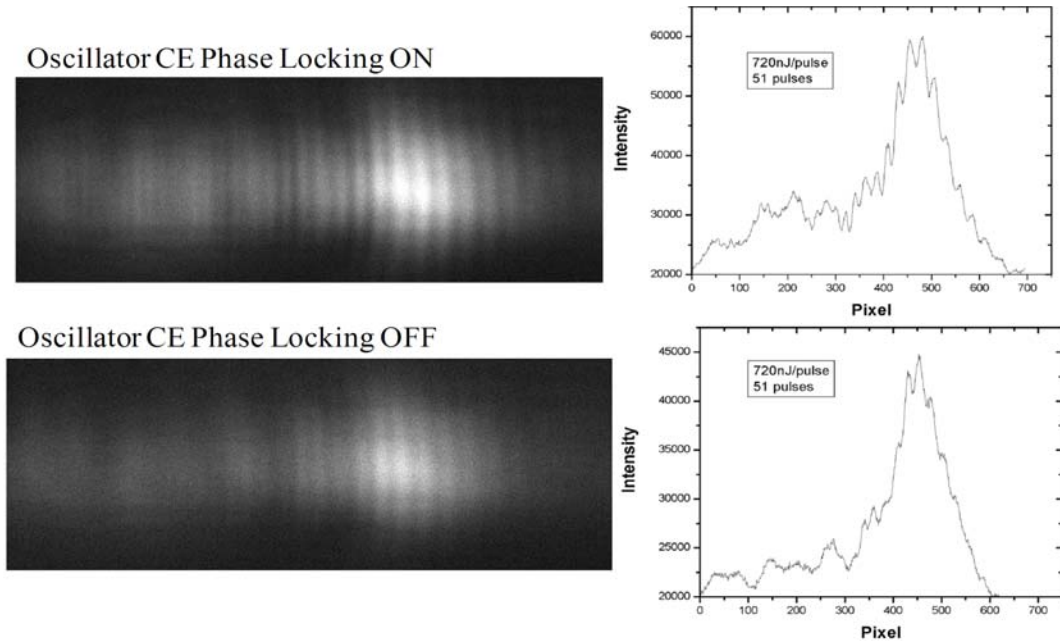


**Figure 5.7 50 ms integration time interference fringes.**



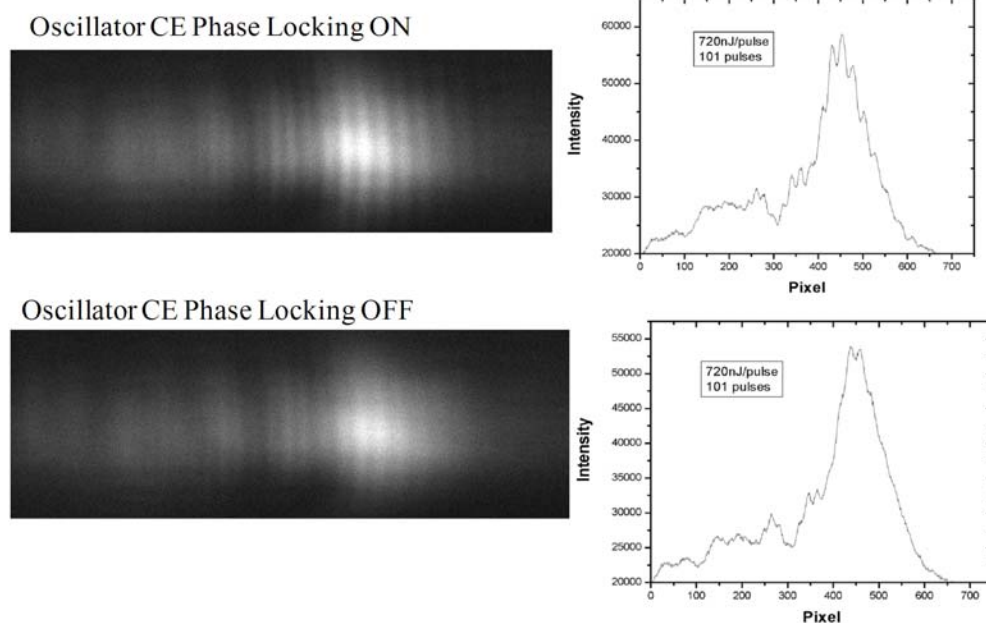


**Figure 5.8 100 ms integration time interference fringes.**

In figure 5.7, 50 laser shots were integrated. As is shown, when the laser oscillator CE phase lock was engaged, the fringe contrast remained high during the integration. However, the unlocked CE phase situation showed that the fringes began to blur, which was representative of CE phase drift. For the 100 ms integration time, the difference between the locked and unlocked cases was even more dramatic. Since the fringe contrast remained high when the oscillator was locked, the CE phase drift of the amplified laser pulses could be measured. The shift of the fringes could be used to correct the CE phase drift of the amplified laser pulses.

### 5.3 Previous Work

In previous research, pulses from the CE phase stabilized oscillator were stretched by passing through a glass block, amplified, and then compressed using prism pairs. [16] The typical energy from such a system was  $\sim 1$  mJ. In order to correct the CE phase drift of the amplified pulses, a portion of the amplifier output was sent to an  $f$ -to- $2f$  interferometer. The measured CE phase drift was used as a feedback control signal to the oscillator locking electronics. An example of such a system is shown in Figure 5.9.

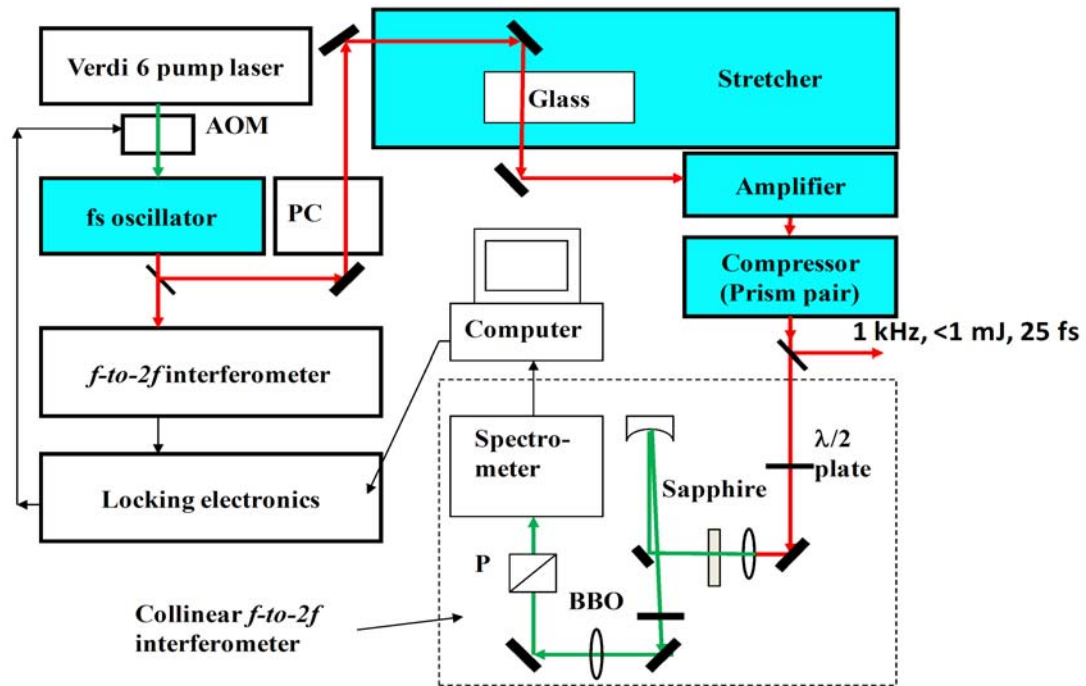


**Figure 5.9 Material-based CPA with CE phase drift feedback to the oscillator locking electronics.**

Using material-based stretchers and compressors, though, made scaling the output of the amplifier to several mJ impossible since the damage threshold of material is low. In order to reach higher energies, grating-based stretchers and compressors must be used. Another problem with the setup described in Figure 5.9 is that the CE phase correction signal is sent to the oscillator locking electronics. In that method, the oscillator locking electronics must stabilize the CE phase of the oscillator plus precompensate the CE phase drift of the amplified laser pulses. This decreases the time over which CE phase locking of the oscillator is possible.

A new method for stabilizing the CE phase drift of the amplified laser pulses is discussed in the next section.

## 5.4 Grating Control Feedback Method

It was found that the grating separation in the stretcher or compressor affected the CE phase of the amplified laser pulses. [56] Also, the grating separation could be varied to correct

the CE phase drift. In addition to correcting the CE phase drift, changing the grating separation could vary the CE phase within a  $2\pi$  range.

In Figure 5.10, two grating-based stretcher arrangements are shown. The top figure shows a stretcher utilizing mirrors in the telescope arrangement. The bottom figure shows a stretcher with lenses as the telescope.

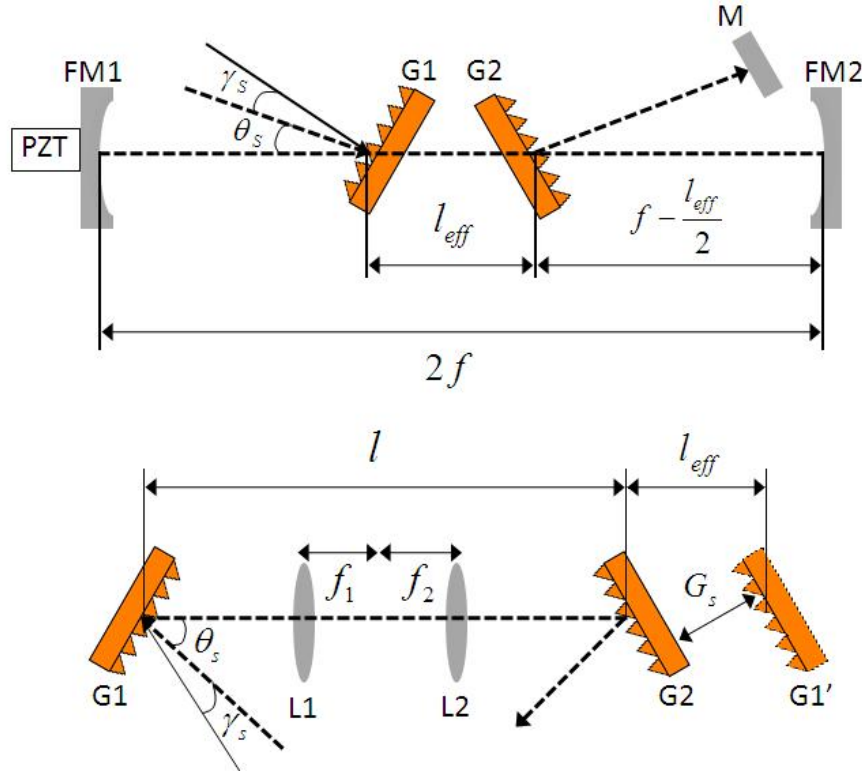


**Figure 5.10 Grating-based stretchers for CE phase stabilization of the amplified laser pulses:  $\gamma_s$  : angle of incidence,  $\theta_s$  : angle between the incident and diffracted rays,  $l_{eff}$  : effective grating separation,  $f$  : focal length, FM1 and FM2 are the focusing mirrors, M is a retroreflecting mirror, PZT: piezoelectronic transducer,  $G_s$  : perpendicular distance between the gratings, G1 and G2 are the gratings, G1' : image of G1,  $l$  : is the distance between the gratings.**

The analysis of the CE phase shift through the stretcher is fairly simple. First, the input electric field of a laser pulse in the frequency domain is given by  $E(\omega) = E_0(\omega) \exp[i(\phi_{CE} + \varphi(\omega))]$ , where  $\varphi(\omega)$  is the spectral phase of the input pulse and

$E_0(\omega)$  is the spectral amplitude. For this analysis, the pulse is assumed to be transform limited which gives a spectral phase of zero. [57]

The spectral phase of the pulse after it traverses the stretcher arrangement is given by:

$$\varphi'(\omega) = \omega\tau(\omega) - 4\pi \frac{G_s}{d_s} \tan[\gamma_s - \theta_s(\omega)] \quad (5.1)$$

where  $\tau(\omega)$  is the group delay. Equation 5.1 evaluated at the carrier-frequency,  $\omega_c$  gives the phase of the carrier-wave at the output of the stretcher. The group delay is given by  $\tau(\omega_c)$ .

Thus, the CE phase change at the output of the stretcher is given by:

$$\Delta\phi_{CE} = \omega_c\tau(\omega_c) - \varphi'(\omega_c) = 4\pi \frac{G_s}{d_s} \tan[\gamma_s - \theta_s(\omega_c)] \quad (5.2)$$

By making the substitution  $G_s = -l_{eff} \cos(\gamma_s - \theta_s)$ , Equation 5.2 can be written as:

$$\Delta\phi_{CE} = -4\pi \frac{\Delta l_{eff}}{d_s} \sin(\gamma_s - \theta_s) \quad (5.3)$$

Now, the effects of beam pointing instability of the incident beam have been studied before and were found to be insignificant. [58] This can be understood by considering that a jitter of the incident beam pointing will be negated as it makes a double-pass through the stretcher.

Equation 5.3 can be further explained if two approximations are made. First, most stretcher and compressor setups have the incident angle close to the Littrow angle, which makes  $\theta_s = 0$ . Second, the grating constant is on the order of a wavelength. Most stretcher and compressor designs used in ultrafast laser systems have gratings with  $\sim 1000$  lines/mm or more. So, this approximation is valid. In this case, Equation 5.3 simplifies to:

$$\frac{\Delta\phi_{CE}}{\Delta l_{eff}} = 2\pi \frac{\lambda}{d_s^2} \approx \frac{2\pi}{\lambda} \quad (5.4)$$

Thus, Equation 5.4 shows that a variation in the effective grating separation on the order of a wavelength will impart a significant CE phase shift to a laser pulse. Equation 5.4 also shows how changing the effective grating separation allows the CE phase to be shifted in value. By attaching a PZT to the focusing mirror (FM1), the grating separation can be changed.

It should be noted that the difference in the previous analysis is equivalent for stretchers and compressors. Equation 5.4 gives the result for both situations. However, in the compressor, a grating must be moved in order to change the CE phase whereas, in a stretcher, a grating or

telescope mirror (or lens) can be translated. Also, the analysis can be extended to prism-based compressors. However, it was found that the CE phase is not nearly as sensitive to the prism separation as it is to the grating separation.

## 5.5 Stabilization of the CE Phase Drift

The experimental setup for measuring and stabilizing the CE phase drift of the amplified laser pulses is shown in Figure 5.11.

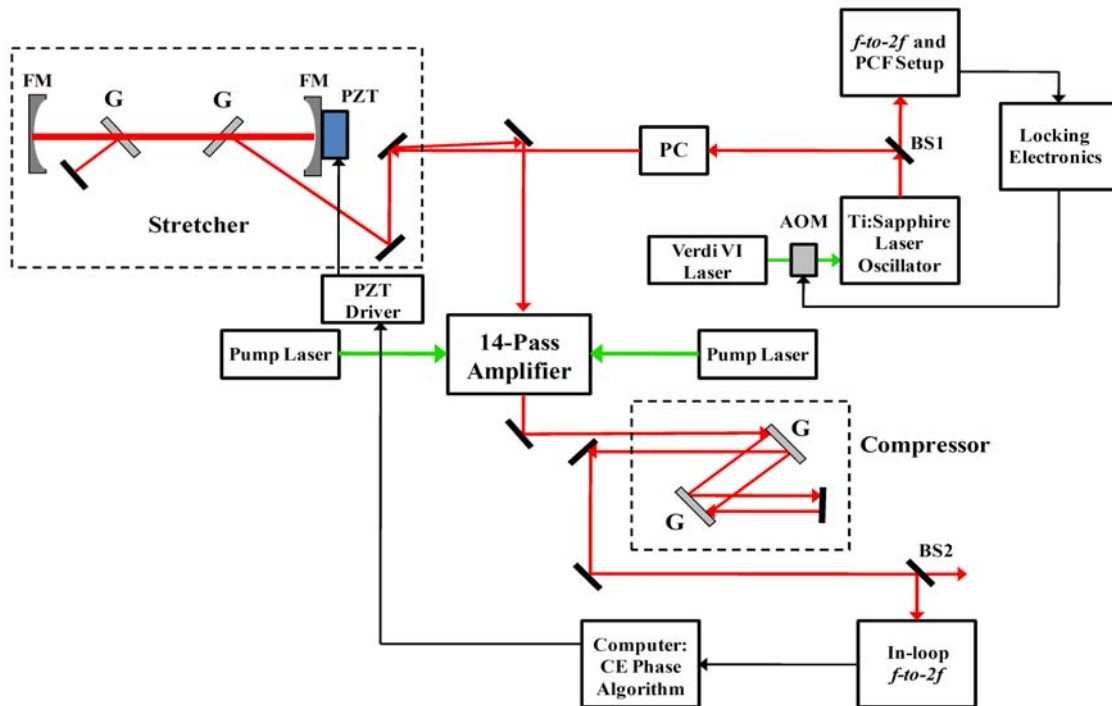
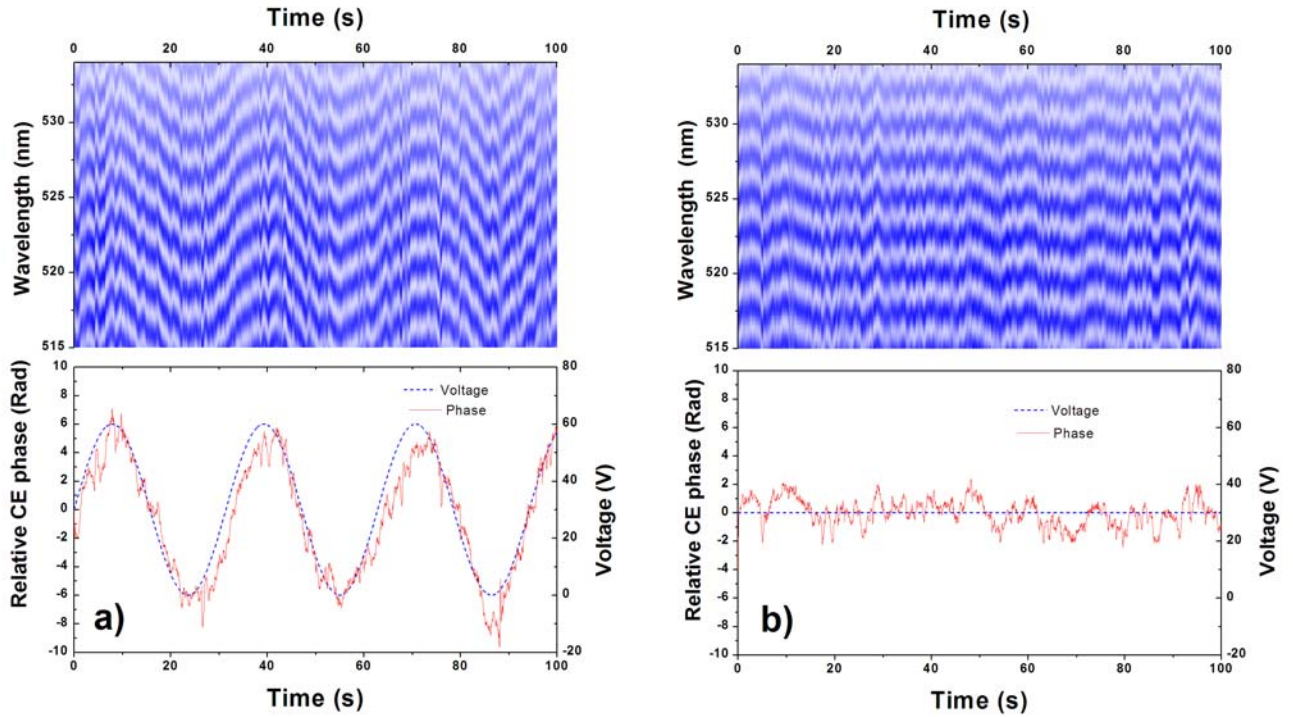


**Figure 5.11 KLS with CE Phase drift stabilization and measurement.**

The setup is exactly the same as in Figure 5.1, except here, the measurement and stabilization setups are shown. The CE phase of the pulses from the laser oscillator was locked by using the  $f$ -to- $2f$  and locking electronics, which sent the correction signal to the AOM in the pump laser path. Similarly, the output of the amplified laser pulse train was split by BS2, which was a 10% beamsplitter, and sent to the  $f$ -to- $2f$ , which here is called the in-loop  $f$ -to- $2f$ . The fringe pattern was collected by the spectrometer and sent to a computer running a CE phase drift measurement algorithm, which will be described in the appendix. The error signal was sent to a PZT driver, which provided the driving voltage for the PZT in the stretcher. Note here that the

spectrometer's CCD camera was triggered off of the laser timing at 50 ms integration time. The CCD then discharged the array at 20 ms.

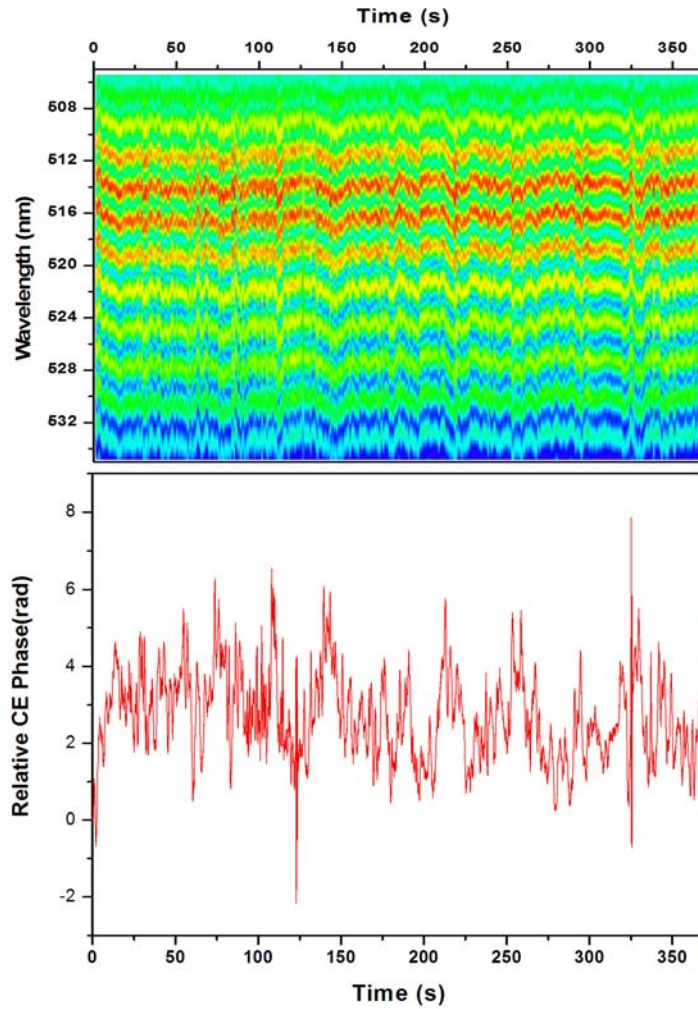
The effect of changing the grating separation on the CE phase drift through the system was measured in Reference 57. [57] In the measurement, the oscillator CE phase was locked. A  $60 V_{p-p}$  sinusoidal modulation was applied to the PZT. The result is shown in Figure 5.12.



**Figure 5.12 Effect of changing the grating separation on the CE phase drift: a)  $60 V_{p-p}$  voltage applied, b) DC voltage applied.**

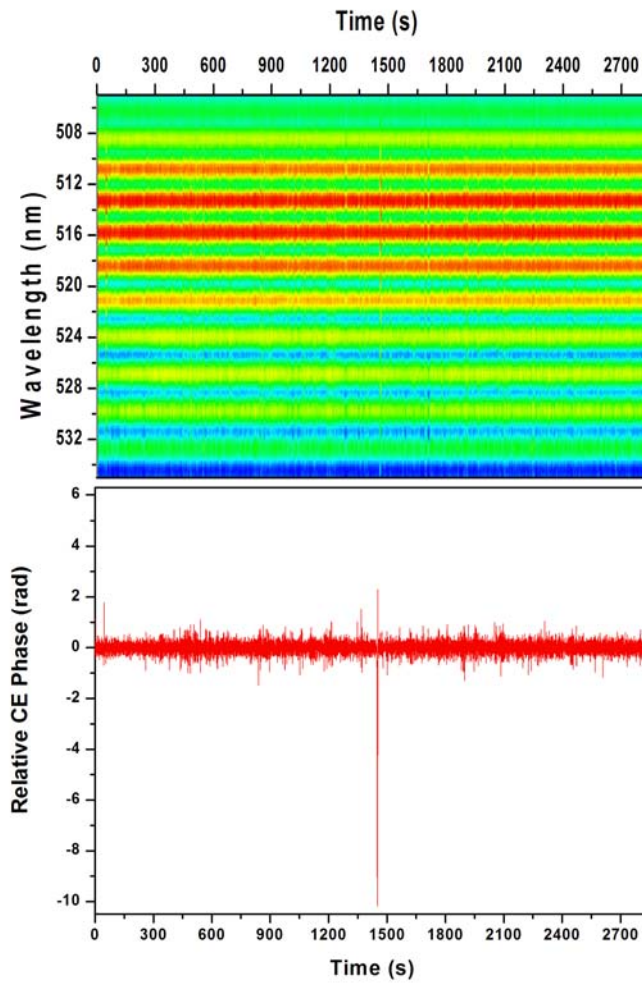
By applying the sinusoidal voltage, the PZT moved by  $3.6 \mu\text{m}$ . From the results, it was found that  $\frac{\Delta\phi_{CE}}{\Delta l_{eff}} \approx 3.7 \pm 1.2 \text{ rad}/\mu\text{m}$ . Since the PZT uncertainty was  $6.1 \pm 1.5 \mu\text{m}/100 \text{ V}$ , some error would be in measurement. However, it was found that changing the grating separation on the order of a wavelength, would result in a significant change in the CE phase. Changing the grating separation of the stretcher is used to correct the CE drift phase drift of the amplified pulses. [57]

Figure 5.13 shows an example when the feedback control was disengaged and the oscillator was locked.



**Figure 5.13 Measured CE phase drift when the feedback control was disengaged.**

The figure shows the shift of the fringe pattern with time. The CE phase drift had a slow drift, usually on the order of Hz. The case when the feedback control was turned on is shown in Figure 5.14.



**Figure 5.14 Feedback control engaged.**

Figure 5.14 clearly shows how the feedback control corrected the slow CE phase drift of the laser pulses. The fringes appeared rigidly locked during the measurement, showing the high CE phase stability of the system. The large spike occurring near 1500 s was due to a slight disturbance of the optical table.

A typical example, when the system is well stabilized is shown in Figure 5.15.



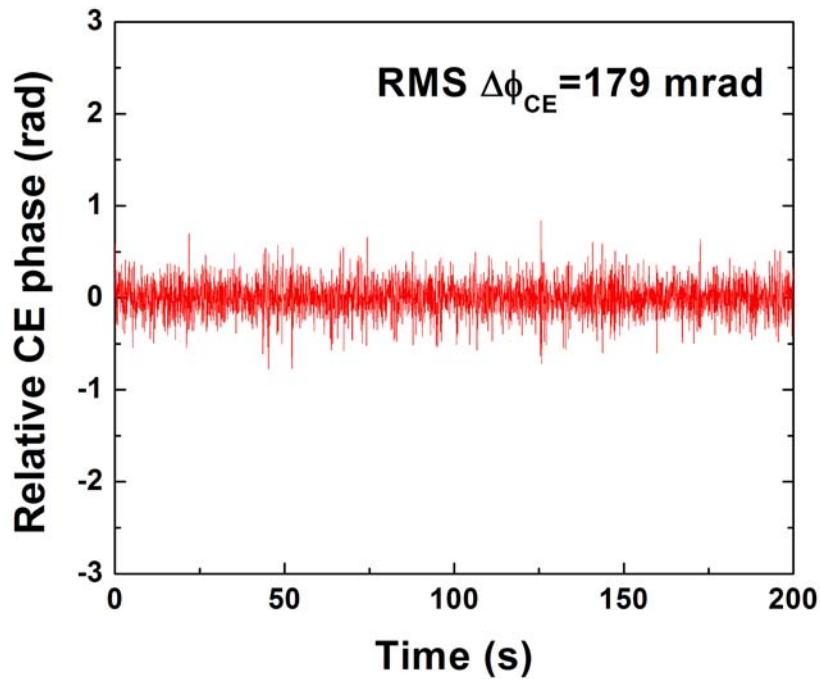


**Figure 5.15 Stabilized CE phase drift.**

In the figure, the rms error of the CE phase drift was 179 mrad. This is a typical value when the oscillator CE phase is well-locked and the feedback control of the amplified laser pulses is running smoothly.

Typically, though, errors of the CE phase drift will be incurred on the system. For example, the optical table may be disturbed, which causes mounts and gratings to shift rapidly. Also, the fast drift of the CE phase is not correctable using the PZT/grating separation method since the response of the optic is too slow. Figure 5.16 shows the type of CE phase errors experienced by the amplified laser pulse train. [18]

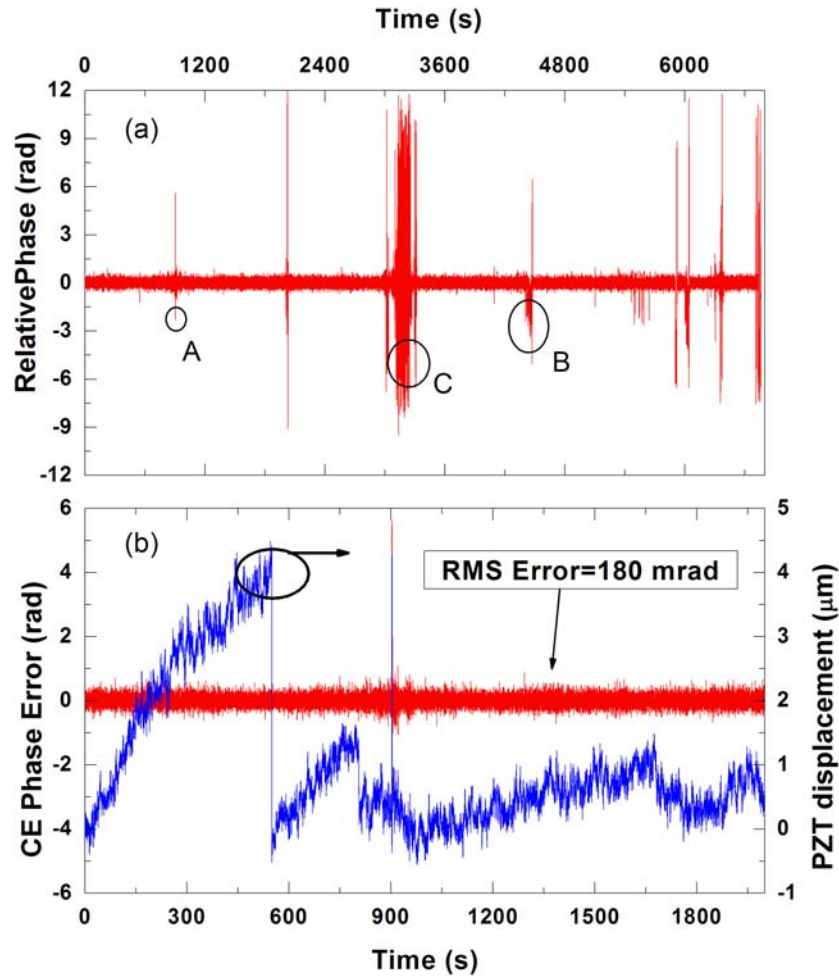


**Figure 5.16 a) temporal evolution of the relative CE phase. A, B, and C represent the three kinds of error spikes. b) the relative CE phase and the displacement of the PZT in the first 32 minutes in a).**

The evolution of the relative CE phase is shown in the above figure. For the experiment, the oscillator CE phase was locked and the CE phase drift of the amplified laser pulses was corrected. The CE phase was stabilized over 110 minutes, except for a 4 minute relocking time. During the relatively stable time, isolated spikes in the relative CE phase occurred due to disturbances of the optical table. Such a spike is represented by A. At B, the PZT could not move quick enough to correct the CE phase error. Typically, though, the relocking time of the PZT, for a short disturbance, was roughly 2 to 3 seconds. However, the hesitant motion of the PZT increased the relocking time to nearly 1 minute. [18]

The biggest error occurred at C, when the oscillator CE phase locking was lost. The relocking of the oscillator took ~2 minutes. Once the oscillator was relocked, though, the amplifier feedback control quickly started to work to correct the CE phase drift.

In figure 5.16b, the displacement of the PZT is shown along with the CE phase error. The error signal is the pulse-to-pulse change in the CE phase. In the first 10 minutes, the PZT moved slowly towards its limit of 5  $\mu\text{m}$ . Once there, the computer reset the PZT to its center position. The change caused little CE phase error. This was not expected as such a big change should have produced a large change in the CE phase. However, it was possible that a large error in the CE phase occurred at the same time as the large shift of the PZT displacement. The PZT followed the large spike in the CE phase error at 900 s to correct. The rms error was 180 mrad during the locking time. [18]

It was soon discovered that changing the grating separation could not only be used as a feedback control mechanism to stabilize the CE phase drift but that it could be used to change the CE phase. This is discussed in the next section.

## 5.6 Control of the Relative CEP

As the grating separation is changed, the set-point for stabilizing the CE phase is changed. This effect was investigated in Reference 18. In the experiment, the set-point for the CE phase locking was varied from  $-1.1\pi$  to  $0.9\pi$  in steps of  $0.2\pi$ . [18] The results are shown in Figure 5.17. The top graph shows the temporal evolution of the fringes obtained using the  $f$ -to- $2f$  interferometer. The bottom plot shows the relative phase, denoted as  $\Delta\phi_{CE}$ , as the set-point was varied. When the measurement began, the set-point moved continuously from 0 to  $-1.1\pi$  during the first 30 seconds. The CE phase was locked at each set-point for 1 minute and shifted to the next value in an increment of  $0.2\pi$  over 1 second. The fringes shifted by almost exactly 1 fringe as the set-point was changed by  $2\pi$ . The CE phase stability and the displacement of the PZT during the changing of the set-point are shown in Figure 5.16. The RMS error during the experiment was found to be 160 mrad. The bottom part of the figure shows how the PZT moved during the experiment. In the first 30 seconds, the PZT moved by 1.5  $\mu\text{m}$  to reach  $-1.1\pi$ . During the changing of the set-point, the PZT moved around an equilibrium position of  $-1.05 \mu\text{m}$  with a standard deviation of 0.28  $\mu\text{m}$ . Thus, as the PZT moved to change the set-point of the CE phase

locking, it also moved in such a fashion as to correct any CE phase errors. Table 1 lists the set-point values, the averaged CE phase ( $\mu$ ) and the standard deviation ( $\sigma$ ) at each locking position.

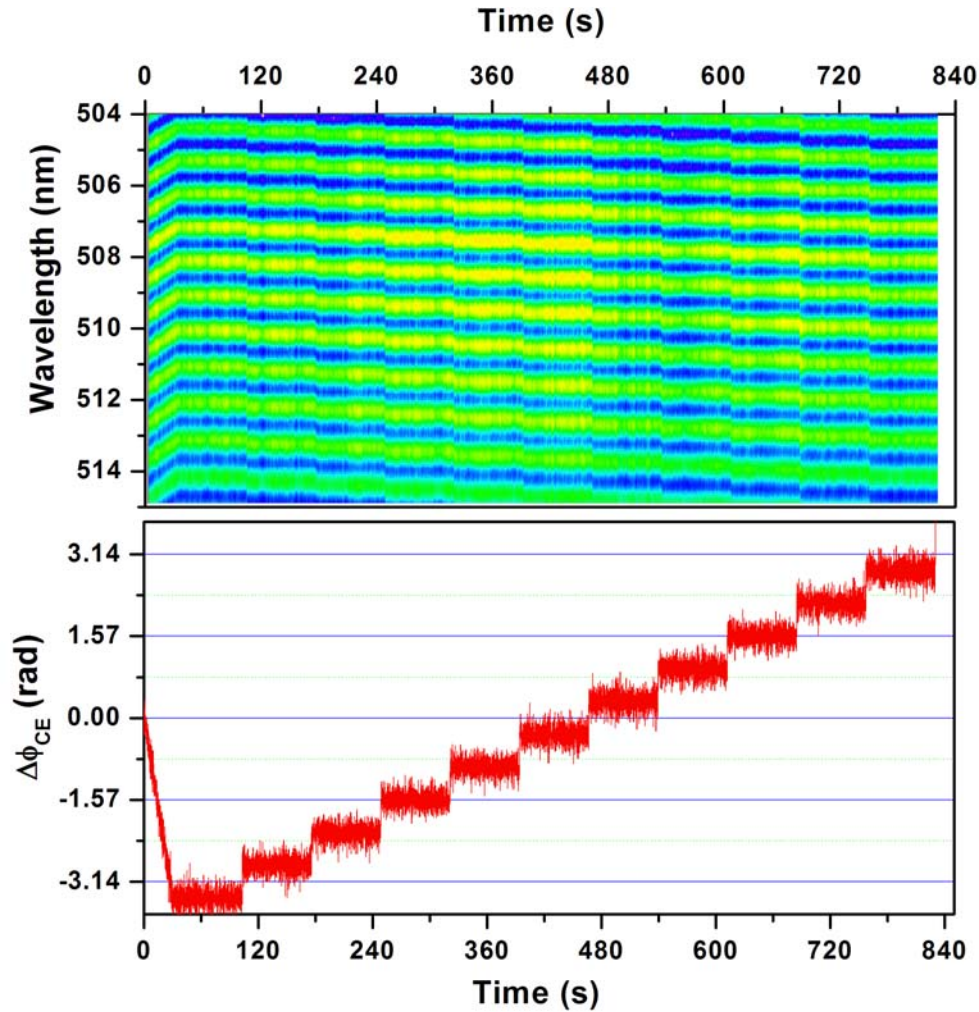


**Figure 5.17** Precisely controlling the CE phase of the amplified laser pulses. Top, the temporal evolution of the interference fringes. Bottom, the effect of changing the locking set-point on the measured relative CE phase.

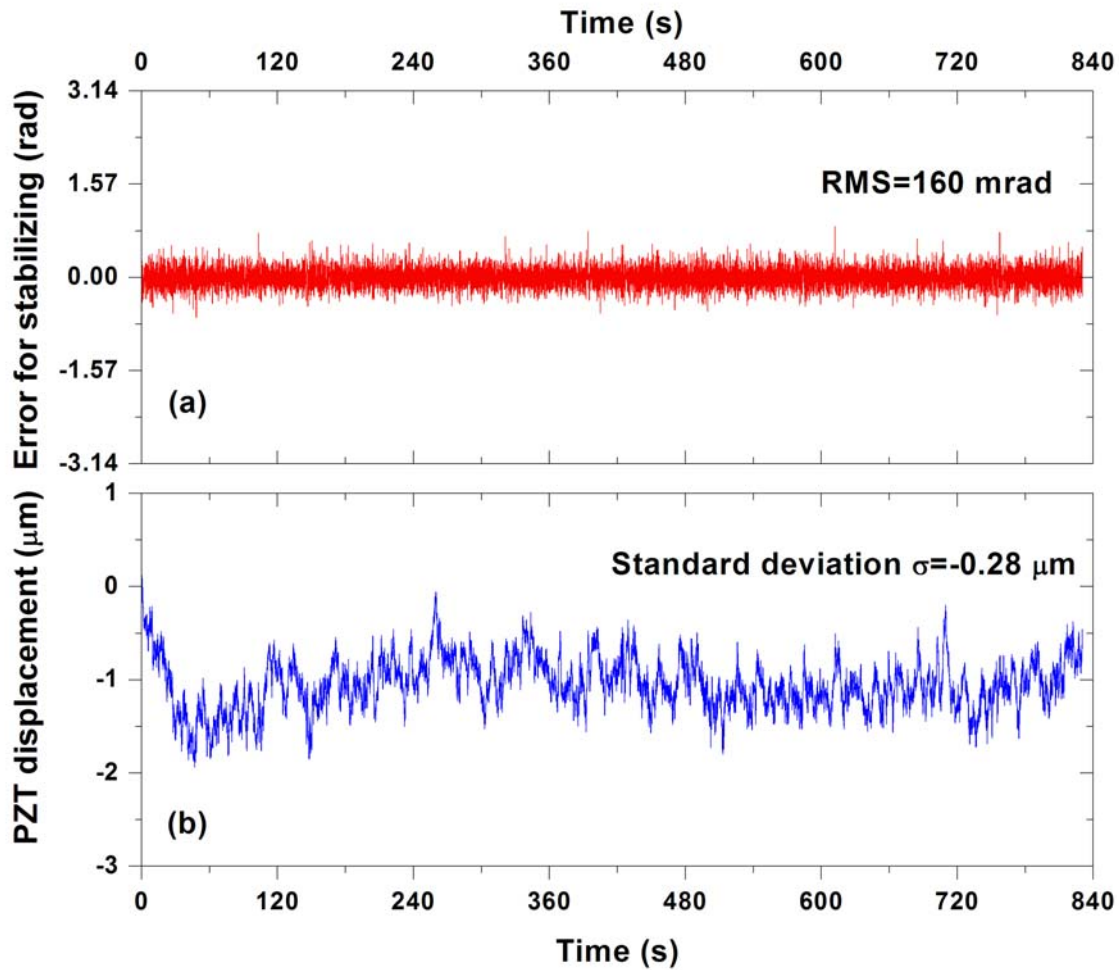
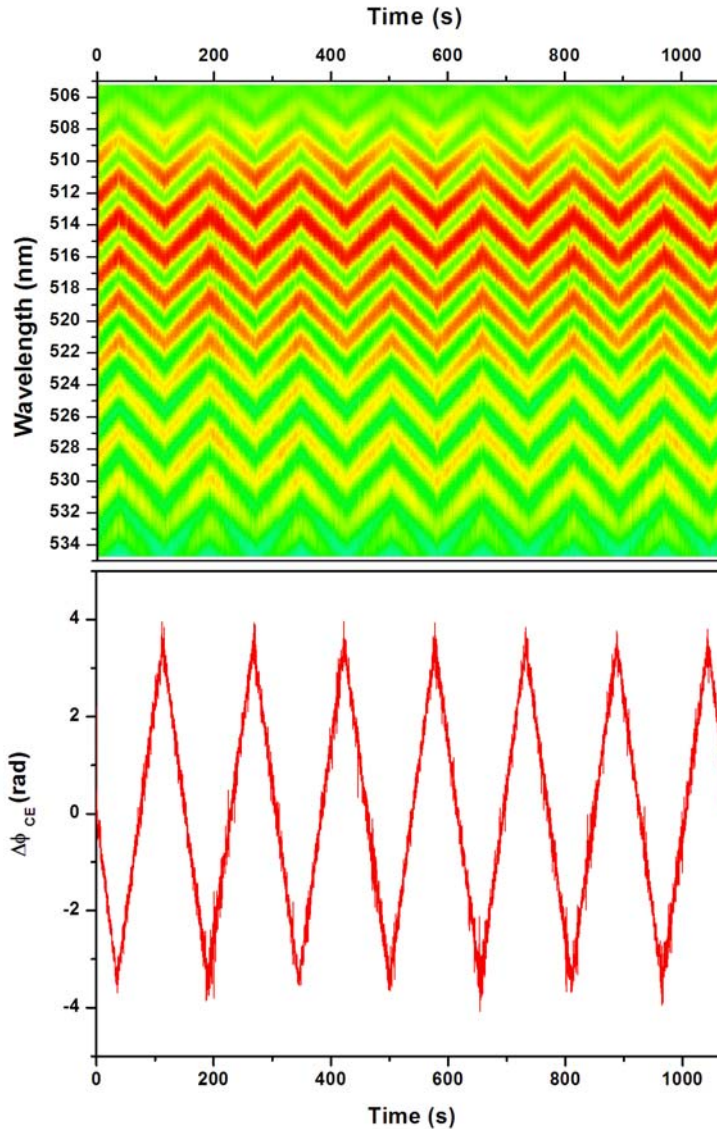


Figure 5.18 a) The error signal for the slow feedback stabilization, b) the displacement of the PZT when the set-point was shifted.

Table 5-1 Comparison of the set-point, average relative CE phase, and corresponding standard deviation of the CE phase error.

<b>Set-Point (rad)</b>	-3.454	-2.826	-2.198	-1.57	-0.942	-0.314	0.314	0.942	1.57	2.198	2.826
<b><math>\mu</math> (rad)</b>	-3.456	-2.828	-2.2	-1.571	-0.944	-0.314	0.314	0.941	1.57	2.199	2.826
<b><math>\sigma</math> (mrad)</b>	159	162	157	153	154	166	170	164	156	163	171

The aforementioned experiment varied the CE phase in a stepwise fashion. In some experimental situations, it might be desirable to sit at a fixed CE phase for a period of time and then move to another point. However, in other situations, rapidly varying the CE phase might be desirable. Using the KLS laser, a “sweeping” modulation was applied to the stretcher grating separation. The results are shown in Figure 5.19.



**Figure 5.19 Top, temporal evolution of the interference fringes. Bottom, swept relative CE phase vs. time.**

The figure shows a triangular modulation to the relative CE phase. The modulation was over  $\sim 2.45\pi$ . Small errors occurred near the peaks and troughs of the triangular wave due to the

PZT moving hesitantly. Those errors could be corrected by having a slower modulation. The CE phase error and displacement of the PZT during the experiment are shown in Figure 5.20.

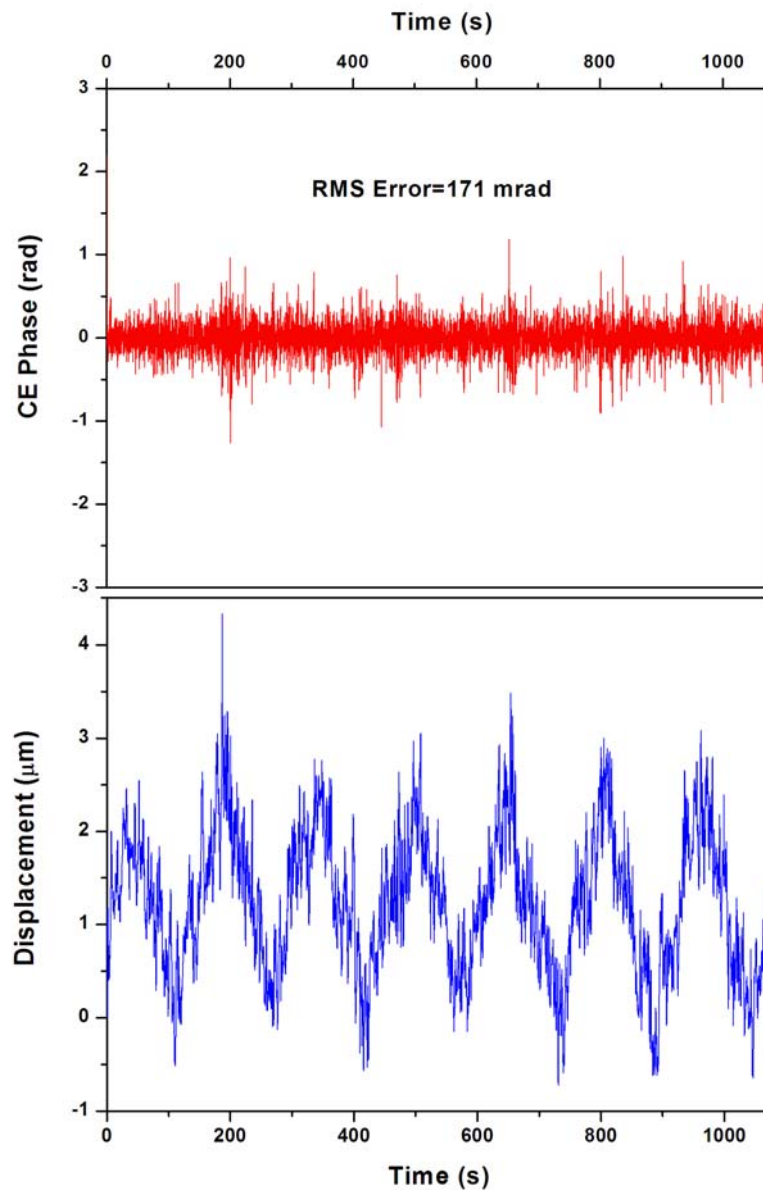


**Figure 5.20 Top, CE phase error during the modulation. Bottom, displacement of the PZT.**

The rms error during the experiment was 171 mrad, which was close to that obtained in the experiment changing the CE phase in steps. The error spikes coincided with the turnaround points of the triangular modulation. Again, by using a slower modulation, the method could be improved.

An example of the long-term sweeping ability of the grating-based system is shown in Figure 5.21.

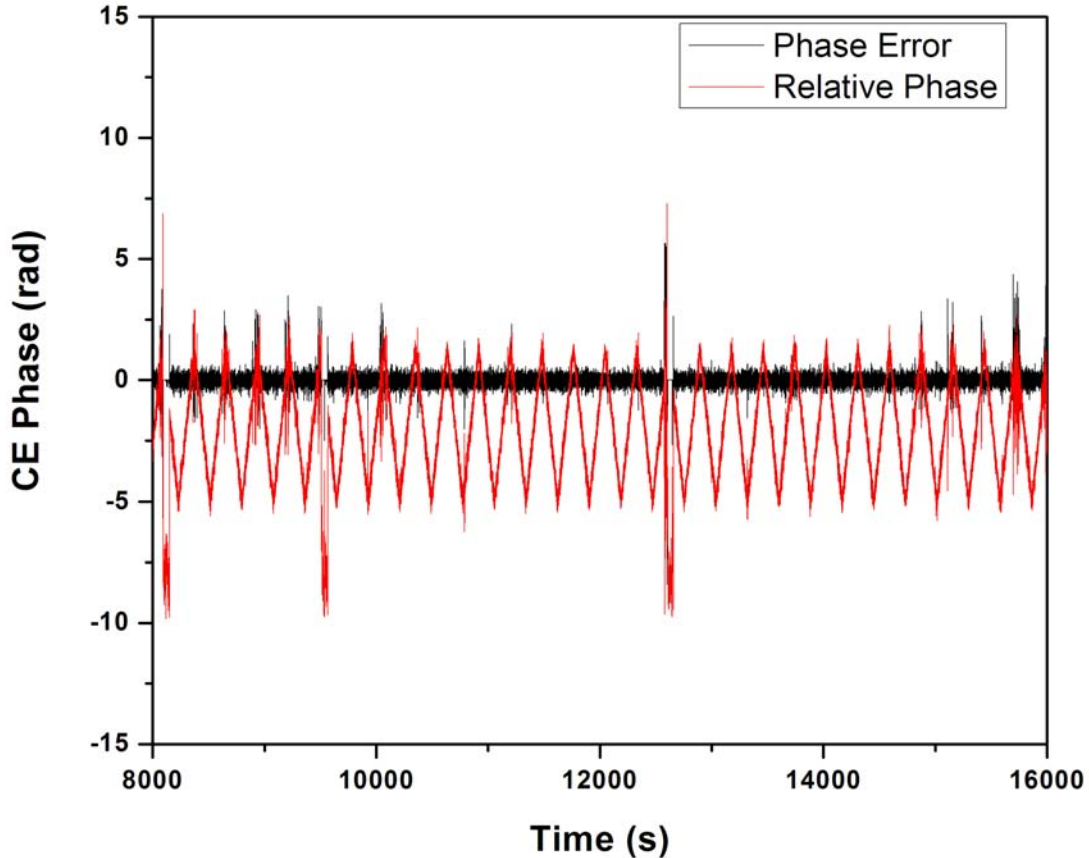


**Figure 5.21 Long-term sweeping stability.**

The figure shows  $\sim 2.2$  hours of the CE phase modulation time. At three points, the CE phase of the amplifier became unlocked, but was quickly relocked by the system. The data, though, shows that the modulation of the CE phase can be maintained over a long time-period. The major limitation is the stability of the oscillator CE phase locking. If the oscillator CE phase locking fails, then the entire system fails.

The ability to use the grating separation to change the CE phase during an experiment is a definite advantage over material-based laser amplifiers. Most physics experiments sensitive to the CE phase require the variation of the CE phase during the experiment. Those groups used a pair of thin fused silica wedges to change the CE phase. However, the fused silica would also



temporally broaden the pulse. Since the experiments required short laser pulse duration, only a small amount of material could be used. The grating-based method obviates the need for wedges and thus solves the pulse broadening problem.

## 5.7 Path Length Drift Stabilization and CE Phase Stability

The CE phase stability of the amplified laser pulses was improved by stabilizing the path length drift of the  $f$ -to- $2f$  interferometer used to stabilize the oscillator CE phase.

The CE phase of the  $i^{\text{th}}$  pulse coming from the oscillator compared to a reference,  $0^{\text{th}}$  pulse, from the oscillator is given by:

$$\phi_{CE,i} - \phi_{CE,0} = \int_0^{i/f_{rep}} 2\pi \left( \frac{f_{rep}}{4} - \frac{1}{2\pi} \frac{d\varphi}{dt} \right) dt = \frac{i}{4} 2\pi + [\varphi(i/f_{rep}) - \varphi(0)] \quad (5.5)$$

Thus, Equation 5.5 shows how a jitter of the path length in the interferometer leads to the imprinting of that noise on the CE phase stability of the pulses from the laser oscillator and from the amplifier. [17]

The effect of locking and unlocking the interferometer on the CE phase stability of the pulses from the amplifier were studied. In the experiment, the CE phase of oscillator was stabilized and the slow drift of the CE phase of the amplified laser pulses was corrected. The results are shown in Figure 5.22.

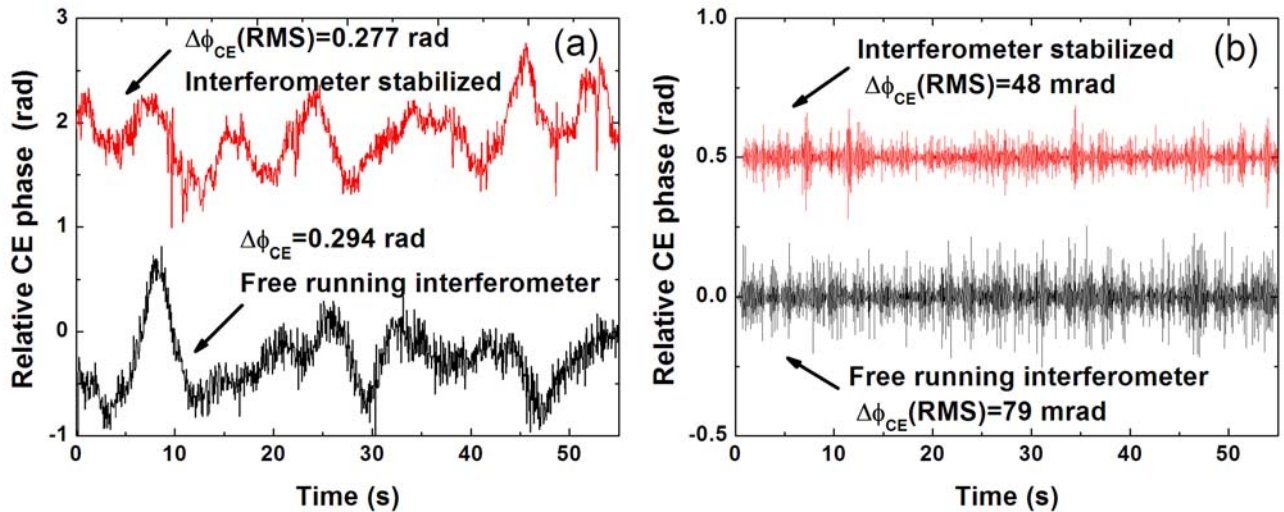


Figure 5.22 a) The relative CE phase measured by the collinear f-to-2f interferometer. b) The fast jitter of the CE phase obtained by applying a high-pass filter to the spectra in a).

The figure on the left shows the CE phase stability of the system when the interferometer was locked and unlocked. No difference was apparent from that measurement. However, in the figure on the right, the fast CE phase noise was investigated by applying a high-pass ( $>3$  Hz) filter to the measurements in the leftmost figure. The results show that the high-frequency CE phase noise of the amplified laser pulses was suppressed by 40%. The result was important because the framing transfer speed of the CCD camera in the  $f$ -to- $2f$  used for measuring the CE phase drift of the amplified lasers pulses was 20 Hz. The Nyquist frequency was then 10 Hz. All higher frequency noises were aliased to that range. Also, the system could only correct lower frequency drift, due to the bandwidth control of the CE phase software, which was  $\sim 3$  to 5 Hz. Thus, by locking the interferometer, the high frequency CE phase noise, which could not be corrected by the system alone, was suppressed. [17]

## **5.8 CE Phase Stabilization using the Compressor Gratings in the KLSII Amplifier**

Another advancement using the KLS laser system was the addition of a second amplifier. The second amplifier was called the KLSII. The KLSII consisted of a 7-pass, liquid nitrogen cooled amplifier followed by a grating-based compressor. Its design was based on the KLSI layout, except the crystal was pumped by a single, high power pump laser (Quantronix Darwin). The pump beam was split by a beamsplitter and focused from opposite directions into the Ti:Sapphire crystal. [19]

The seed pulses for the KLSII came from a small reflection ( $\sim 3\%$ ) from a beamsplitter placed before the KLSI compressor. The KLSI and KLSII shared the same oscillator and stretcher. The KLSII output 1 mJ, 38 fs pulses at a 1 kHz repetition rate.

The KLSII used a grating-based compressor. In the KLSI system, the stretcher was used to correct the CE phase drift of the laser pulses. The stretcher, though, could not compensate the drift through the KLSII amplifier.

In order to correct the CE phase drift through the KLSII amplifier, one of the gratings in the compressor was mounted on a PZT stage. The pulses from the amplifier were directed to an

$f$ -to- $2f$  interferometer similar to that used by the KLSI in order to measure the CE phase drift. The experimental layout is shown in Figure 5.23. In the  $f$ -to- $2f$  interferometer, a high-speed spectrometer (Ocean Optics HR2000) was used for measuring the CE phase shift. [19]

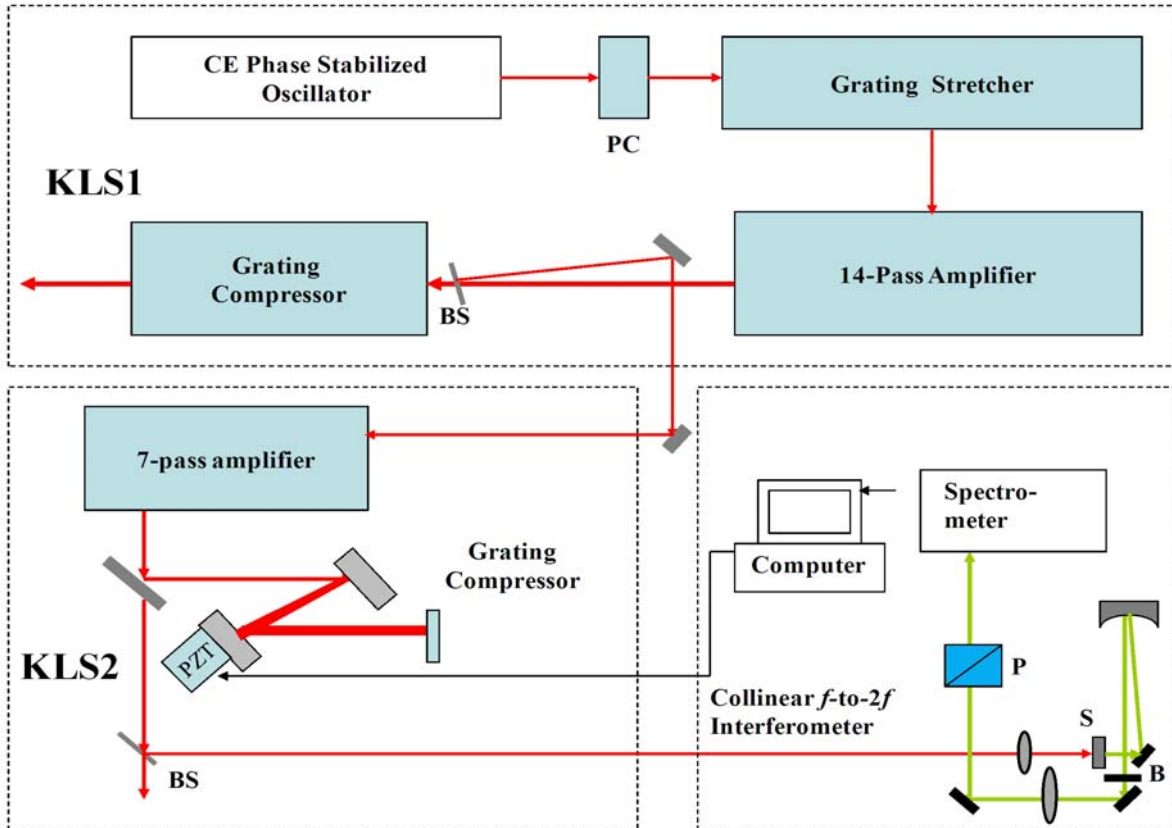


**Figure 5.23** Experimental setup for controlling the CE phase of the amplified laser pulses.  
**PC: Pockels cell, BS: beamsplitter**

The configuration of the double-pass grating compressor is shown in Figure 5.25. The CE phase shift is analyzed using exactly the same method as in Chapter 4. Here, each groove introduces a  $2\pi$  phase shift. The CE phase change for each pass is equal to the number of grooves covered by  $S$  multiplied by  $2\pi$ . [18]

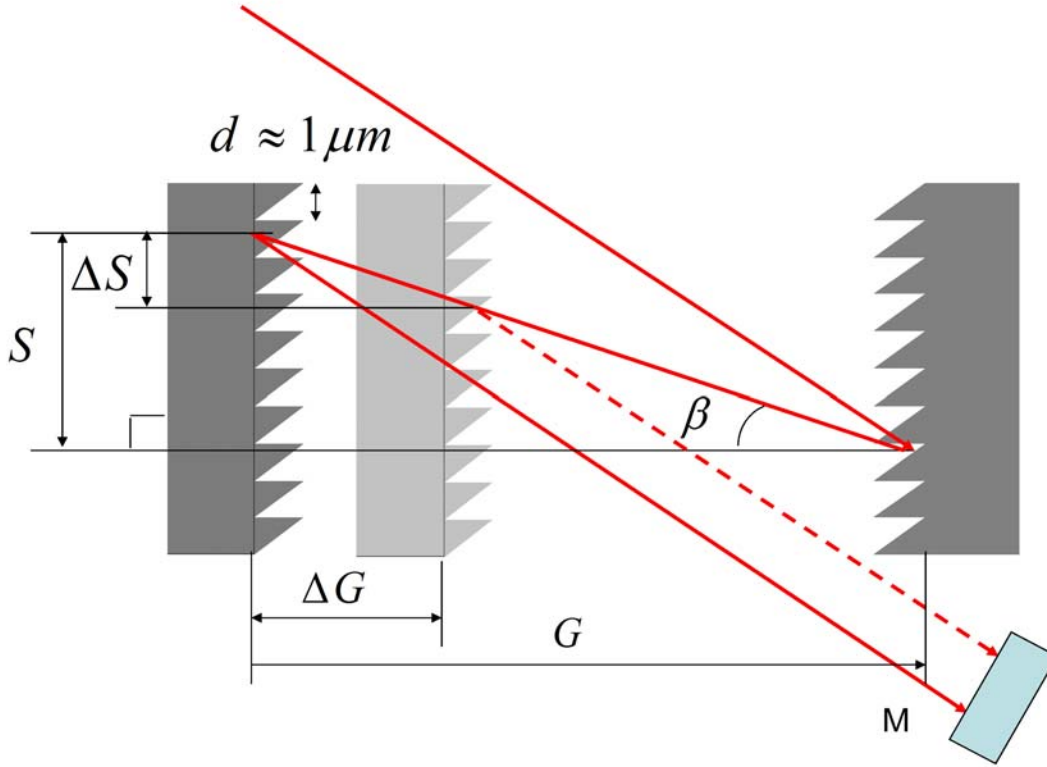


**Figure 5.24 Configuration of a double-pass grating compressor. G: grating separation, d: grating constant,  $\beta$  : diffraction angle, M: retro-reflection mirror.**

The CE phase shift is given by:

$$\Delta\phi_{CE} = \frac{4\pi\Delta S}{d} = \frac{4\pi\Delta G}{d} \tan[\beta(\omega_c)] \quad (5.6)$$

Prior to investigating the use of the compressor grating separation for CE phase stabilization, the frequency response of the PZT mounted grating was measured. In order to stabilize the CE phase drift, the frequency response of the grating needed to be within the bandwidth of the CE phase drift. The measurement was done with a Michelson interferometer and used a CW laser. The variation of the intensity of the interference pattern was measured on a dynamic signal analyzer. The experiment measured  $\Delta G(f) = H(f)V(f)$ , where  $H(f)$  was the frequency response function and  $V(f)$  was the applied voltage. The result is shown in Figure 5.25. For the low frequencies, the frequency response was modulated due to the hysteresis of the PZT. The resonant frequency was found to be near 90 Hz. [18]

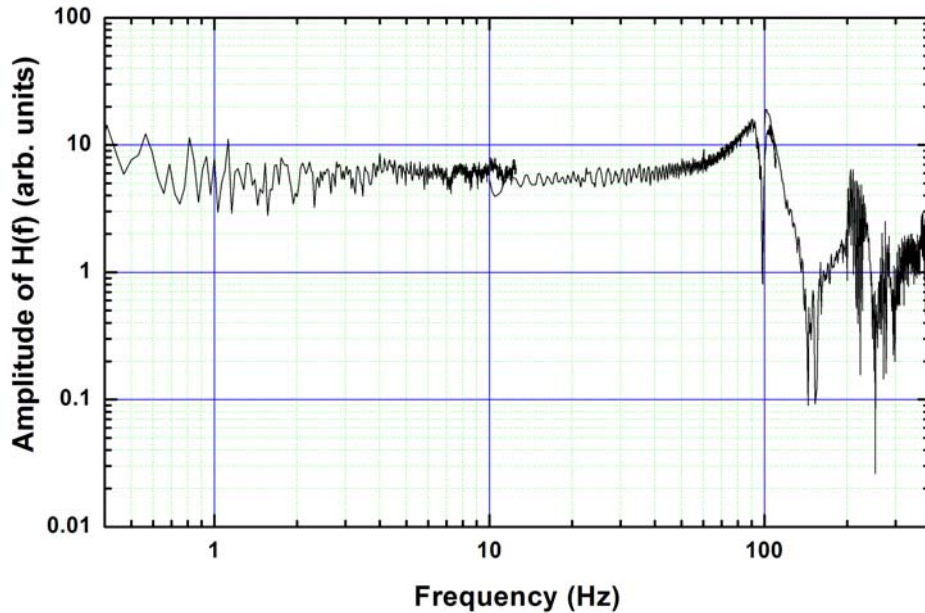


**Figure 5.25 The frequency response of the PZT mounted grating.**

The response of the CE phase at different driving voltages of the PZT was also measured. The response of the CE phase can be expressed as:

$$|\Delta\phi_{CE}(f)| = K(f)|V(f)| \quad (5.7)$$

where  $V(f)$  is the Fourier transform of the driving voltage sent to the PZT and  $\Delta\phi_{CE}(f)$  is the Fourier transform of the retrieved CE phase shift.  $K(f)$  is the frequency response of the CE phase shift, which is also determined by the measurement system and the frequency response of the PZT.

The experimental method used to determine  $K(f)$  involved measuring the CE phase shift at different driving voltages of the PZT. The CE phase shift was measured as a function of time by the spectrometer and analysis software. Thus, the Fourier transform of the CE phase shift was taken in order to obtain the frequency response. [18]

The result of the measurement is shown in Figure 5.26. The integration time of the spectrometer was 5 ms in the range of 3-35 Hz and 2 ms in the range of 40-120 Hz. The main result was that the resonant frequency of the system was found to be near 60 Hz. The result implies that CE phase drift lower than 60 Hz could be corrected by moving the grating.

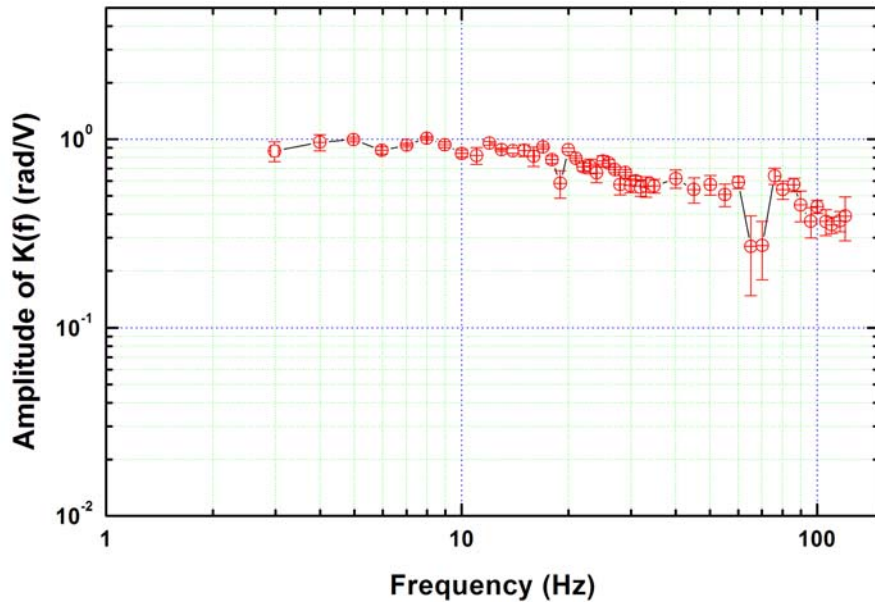


**Figure 5.26 The frequency response of the retrieved CE phase shift when the PZT was driven at different frequencies.**

Once the response characteristics of the CE phase system were known, the system was used to correct the CE phase drift of the pulses from the KLSII. In the experiment, the laser oscillator CE phase was stabilized, but the stretcher grating control in the KLSI was not engaged. The integration time of the spectrometer for the measurements was set to 50 ms. The results are shown in Figure 5.27. [18]

The top plot shows the CE phase drift as a function of time. The dotted line (blue) shows the free running CE phase drift. The solid line (red) shows the stabilized CE phase drift. The solid line was shifted to avoid the dip at 0 Hz in its Fourier transform spectrum, which is shown in the bottom figure. The CE phase was stabilized over 270 s with a 230 mrad rms error, which is comparable to that achieved using the KLSI stretcher grating separation. The bottom plot shows the Fourier transform spectra of the locked and unlocked cases. The graph shows that the low frequency CE phase drift (<4 Hz) was well-corrected by the system.

Ultimately, as was the case for the KLSI stretcher grating system, the CE phase stabilization of the laser oscillator determines the time over which the CE phase drift of the amplified pulses could be stabilized. In further measurements with the KLSII system, the CE phase drift was corrected over 30 minutes before the oscillator CE phase locking was lost.

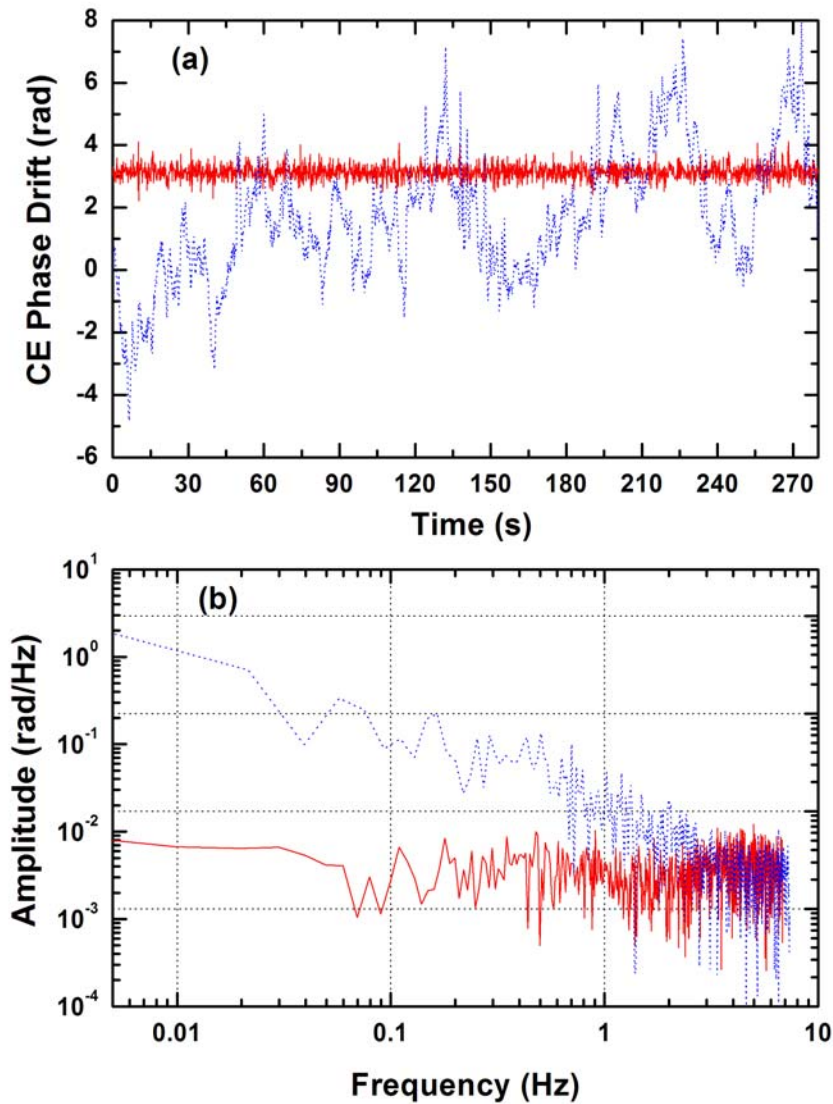


**Figure 5.27 a) The evolution of the free drifted (dotted line) and stabilized (solid line) CE phase drift. b) The fast Fourier transform of the CE phase drift under the free running (dotted line) and stabilized conditions (solid line).**

The important result from the work with the KLSII amplifier was the use of the compressor grating separation to correct the CE phase drift, which was not previously studied. In some amplifier designs, the optics in the stretcher could be too big to mount on a PZT stage or inaccessible. Often, the stretcher employs large mirrors. It would then be desirable to mount the compressor grating on a PZT stage.

# CHAPTER 6 - Amplifier Power Stability and $f$ -to- $2f$ Measurement Error

## 6.1 Out-loop $f$ -to- $2f$

In order to determine the quality of the CE phase locking system, a second  $f$ -to- $2f$  interferometer, called the out-loop interferometer, was constructed. This interferometer's function was to measure the CE phase drift of the amplified laser pulses while the in-loop  $f$ -to- $2f$ , which was described in the previous chapter, was used to stabilize the CE phase drift of the KLS pulses. The out-loop interferometer did not participate in the stabilization of the CE phase drift and could therefore measure the quality of the phase locking system. The interferometer is shown in Figure 6.1.

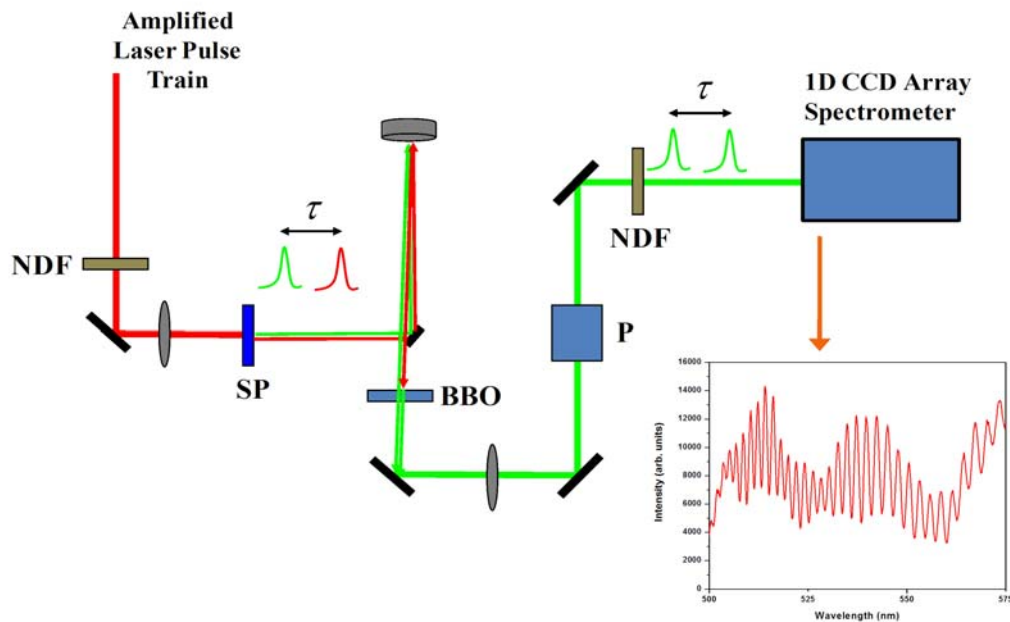


Figure 6.1. Out-loop  $f$ -to- $2f$ .

The out-loop interferometer was identical to the in-loop interferometer except that the BBO was 0.5 mm thick and the spectrometer consisted of a 1D CCD array for fast data acquisition. This spectrometer was used to measure the KLSII CE phase shift as described in the previous chapter.

## 6.2 Power Locking and In-loop and Out-loop Measurements



An important result was obtained when the CE phase drift, measured and stabilized using the in-loop interferometer, was also measured with the out-loop interferometer. The out-loop phase measurement showed that the real CE phase drift was not as well stabilized as the in-loop results indicated. The reason was due to power fluctuations of the amplified laser pulses.

In Reference 20, a power locking system was described. In the setup, the 0<sup>th</sup> order diffraction from the compressor in the KLS was input to a power meter. The signal was sent to a PID controller, which varied the voltage sent to the Pockels cell before the stretcher. The power noise below 40 Hz was suppressed by the control loop. This reduced the power fluctuation from 1.33% rms to 0.28% rms. [20]

Then, the out-loop was used to measure the CE phase drift when the power locking was turned on and when it was turned off while the in-loop interferometer stabilize the CE phase drift. The result for when the power locking was engaged is shown in Figure 6.2.

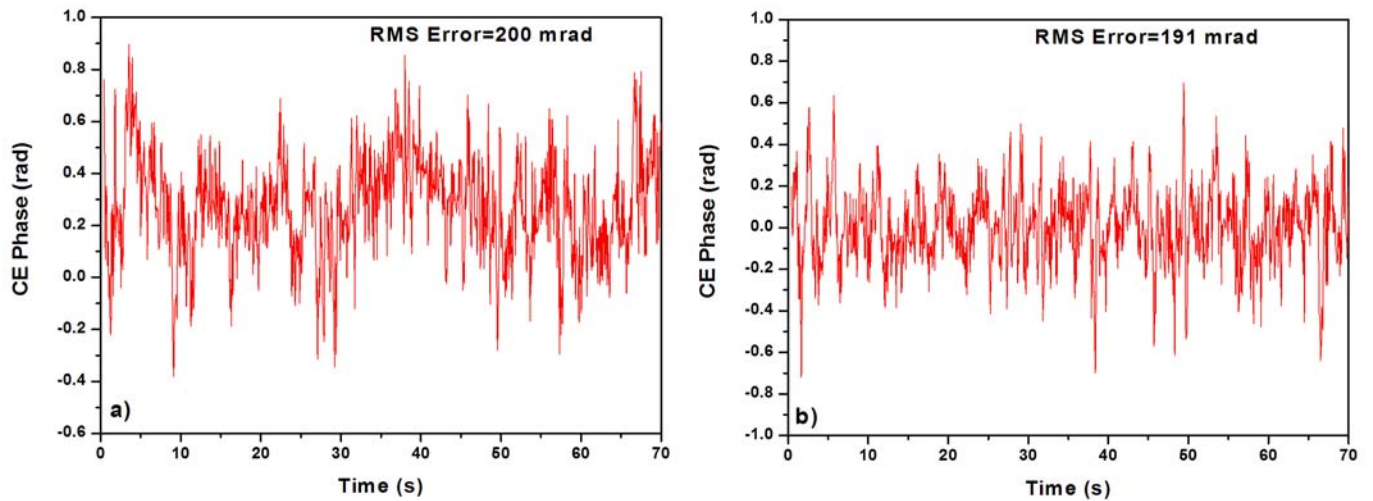


**Figure 6.2 Power locked. a) Out-loop measured CE phase, b) In-loop measured CE phase.**

When the power locking was turned on, the in-loop CE phase error was measured to be 191 mrad rms. Comparably, the out-loop CE phase error was measured to be 200 mrad rms. For the measurement, the power fluctuation was 0.28% rms. Figure 6.3 shows the case when the power locking was disengaged.

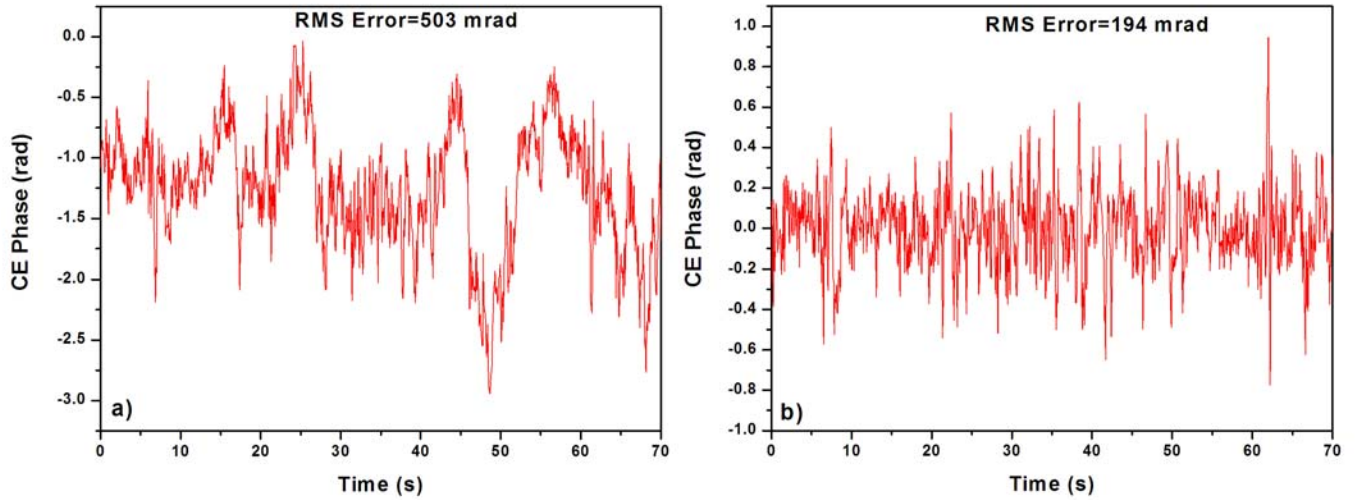


**Figure 6.3 Power unlocked. a) Out-loop measured CE phase, b) In-loop measured CE phase.**

When the power locking was turned off, the in-loop CE phase error was measured to be 194 mrad rms. The out-loop CE phase error, though, was measured to be 503 mrad rms, which was much larger than indicated by the in-loop. [20]

The results indicated the need for a good power stability of the amplified laser pulses in order to obtain an accurate measurement of the CE phase drift using the sapphire plate-based  $f$ -to- $2f$  interferometers.

### 6.3 Phase-Energy Coupling

In Reference 59, the CE phase-energy coupling was investigated. The coupling between the CE phase and the laser energy can be expressed as  $C_{PE} = \frac{\Delta\phi_{CE}}{(\Delta\varepsilon/\varepsilon)}$ , where  $\Delta\varepsilon/\varepsilon$  is the relative laser energy change. [59] Previously, the effect of power fluctuation on the oscillator CE phase locking measurement was reported. [60] A similar measurement for the amplifier CE phase measurement was performed. [16] However, the measurement was not performed at the wavelengths for the  $f$ -to- $2f$  measurement. The setup for measuring the coupling coefficient  $C_{PE}$  is shown in Figure 6.4.

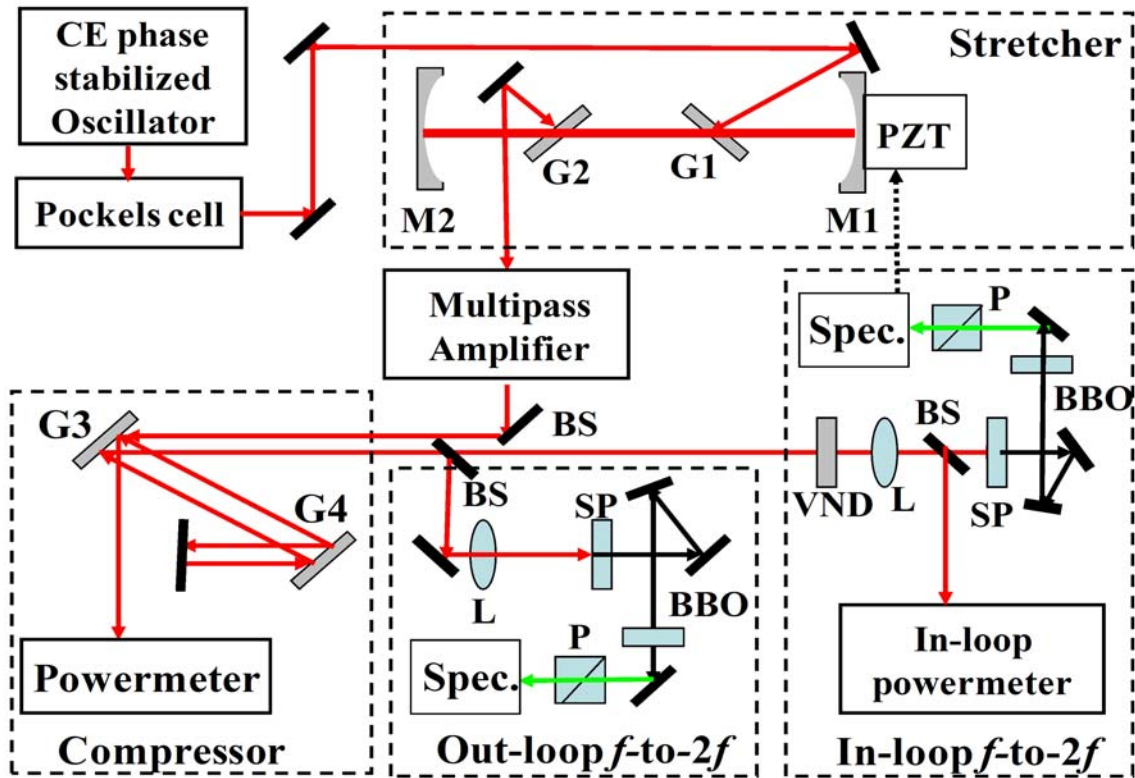


**Figure 6.4 Setup for measuring the CE phase-energy coupling coefficient.**

The setup was similar to the one used to measure the effects of power locking on the measured CE phase drift as discussed in the previous section. In the experiment, 10% of the output from the KLS laser was split off and half of that energy was sent to the in-loop  $f$ -to- $2f$ , while the other half was sent to the out-loop  $f$ -to- $2f$ . The in-loop was used to stabilize the CE phase drift of the laser pulses while the out-loop was used to measure the CE phase drift. Also, the power was locked during the experiment. The power stability was 0.1% rms within a 0-5 Hz bandwidth. The variable neutral density filter before the sapphire plate in the in-loop was mounted on a rotational mount. The VND then was rotated to change the laser energy in a sinusoidal fashion. [59]

Since the laser energy was changed, the in-loop would measure the CE phase drift and stabilize the phase to whatever it measured. Of course, as was reported before, a change in laser energy before the in-loop resulted in measurement error. In this experiment, the measurement error was finely controlled by changing the laser energy. Thus, as the in-loop stabilized the CE phase to its perceived value, the pulses incident at the out-loop interferometer carried the

measurement error. Since the power was locked, only a negligible measurement error was introduced on the out-loop measurement. An additional power meter measured the power stability of the laser system independent of the power locking loop. This power meter was called the out-loop power meter. The result of the measurement is shown in Figure 6.5. [59]

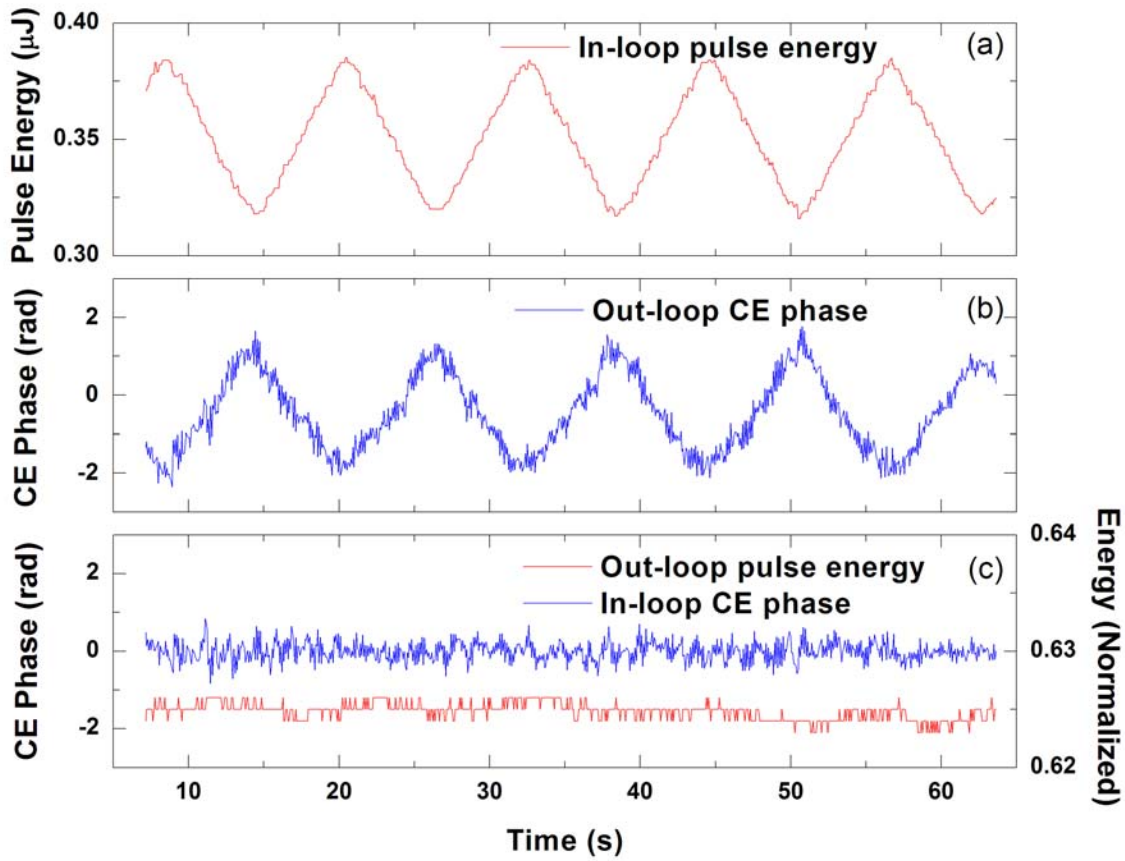


**Figure 6.5** Temporal evolution of the measured phase and laser energy. a) Modulated in-loop pulse energy, b) measured out-loop phase, c) the in-loop phase and out-loop pulse energy.

The result clearly shows how the measured out-loop phase modulated as the energy in the in-loop was modulated. Figure 6.6 shows the analyzed raw data.

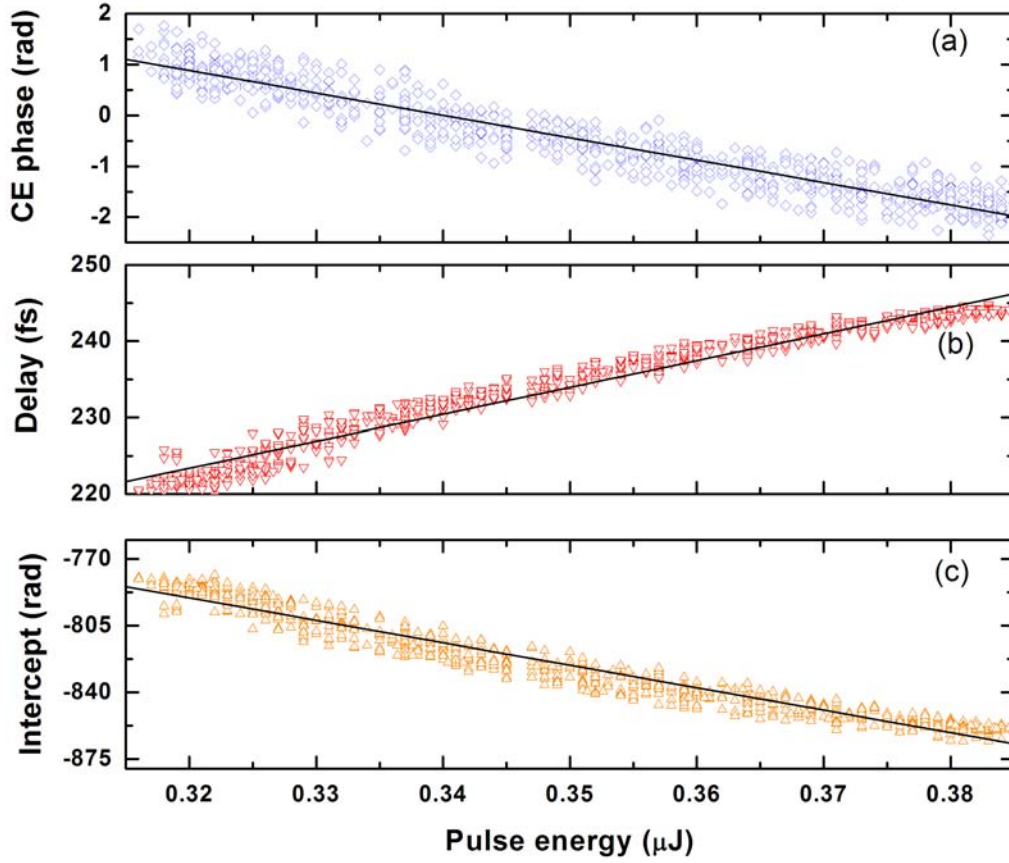


**Figure 6.6 Retrieved experimental results versus the laser energy. a) Relative CE phase, b) delay time, c) the residual intercept after the subtraction of the CE phase.**

From the top figure, the CE phase-energy coupling coefficient can be obtained from the slope of the fit line. The slope corresponded to a coupling coefficient value of  $C_{PE} = 160$  mrad per 1% change in laser energy. 160 mrad is the same as the best CE phase stability of the amplified laser pulses indicated by the in-loop measurements prior to this work. For example, in Figure 6.5, the in-loop CE phase stability was indicated to be 160 mrad. Thus, the energy stability of the amplified laser pulses is an important parameter for CE phase measurements. [59]

The error introduced by the energy fluctuation can be explained by considering the measured total phase. Similar to the discussion in chapter 4, the measured spectral interferogram can be expressed as:

$$S(\omega) = I_{WL}(\omega) + I_{SHG}(\omega) + 2\sqrt{I_{WL}(\omega)I_{SHG}(\omega)} \times \cos[\phi_{SHG}(\omega) - \phi_{WL}(\omega) - \omega\tau_0 + \phi_{CE} + \delta\phi_{CE}] \quad (6.1)$$

where  $\tau_0$  is the delay between the green pulse relative to the IR pulse, which is caused by dispersion in the sapphire plate and  $\delta\phi_{CE}$  is an acquired CE phase shift through the sapphire plate. For the CE phase stabilization procedure, the total phase, the argument of the cosine, is stabilized, as was discussed before in chapter 4. However, the terms in the phase, except for the absolute phase  $\phi_{CE}$ , are intensity dependent. The real CE phase shift, then, is given by:

$$\Delta\phi_{CE} = \Delta\Phi(\omega) - \Delta[\phi_{SHG}(\omega) - \phi_{WL}(\omega) - \omega\tau_0 + \delta\phi_{CE}] \quad (6.2)$$

where  $\Delta\Phi(\omega)$  is the change of the total phase and is set to zero when the CE phase stabilization procedure is implemented. Thus, the second term represents the CE phase error.

The delay time in the results given in Figure 6.6 was determined by fitting the measured total phase versus angular frequency. Then, the intercept was given by

$\phi_{SHG}(\omega) - \phi_{WL}(\omega) + \phi_{CE} + \delta\phi_{CE}$ . The fit of the line in the middle plot of Figure 6.6 gave a value of 1.23 fs delay change per 1% energy change, which corresponded to a phase shift of 4.45 rad. Alternately, as the laser energy changed, the intercept downshifted almost the same amount as the delay upshifted. The increase of the phase due to the delay was counteracted by the decrease of the phase due to the intercept. The sum of the two effects gave the 160 mrad per 1% energy fluctuation. [59]

The mechanism of the phase-energy coupling will be explained in the next section.

## 6.4 Coupling Mechanism

A simple two-step model has been proposed to explain the coupling between the energy fluctuation and the CE phase shift. The model focuses on the nonlinear effects in the sapphire plate which occur during the formation of the  $f$  and  $2f$  pulses. The generation of the white-light and the subsequent formation of a filament involve complicated nonlinear processes. The two-step model is analytical over the energy range considered for the phase-energy coupling measurements.

When the laser peak power is higher than the critical power,  $P_c = \pi(0.61)^2 \frac{\lambda_0^2}{8(n_0 n_2)}$ , a filament is formed inside the sapphire plate. For the model, the laser wavelength is chosen as  $\lambda_0 = 0.79 \mu\text{m}$ .  $n_0 = 1.76$  and  $n_2 = 2.9 \times 10^{-16} \text{ cm}^2/\text{W}$  are the linear and nonlinear indices of refraction of the sapphire plate respectively. The critical power is then  $P_c = 1.79 \text{ MW}$ . The focal

spot radius at the input of the sapphire plate is given by  $w_0 = \lambda_0 \frac{f}{D}$ , where  $D$  is the input laser diameter. [61,62]

As the laser beam is focused into the sapphire plate, the beam size decreases due to Kerr self-focusing until defocusing caused by laser-produced plasma balances the self-focusing. [62] The self-focusing distance as a function of laser energy is given by:

$$z_{sf}(\varepsilon) = \frac{2n_0 w_0^2}{\lambda_0} \frac{1}{\sqrt{\frac{\varepsilon}{\tau_p P_c} - 1}}, \quad (6.3)$$

where  $\tau_p$  is the laser pulse duration at the input of the sapphire plate and  $\varepsilon$  is the laser pulse energy. [64] For the *f-to-2f* interferometer used for the KLS CE phase stabilization, the pulse duration is 35 fs, the input beam diameter is 5 mm, and the focal length is 75 mm.

A calculation shows that the self-focusing distance decreases with increasing pulse energy, which was expected. Once the self-focusing distance is known, the filament length can be obtained. The expression for the filament length is  $z_{fila}(\varepsilon) = L - z_{sf}(\varepsilon)$ , where  $L$  is the thickness of the sapphire plate. The sapphire plate is 2.3 mm thick in the *f-to-2f*.

As the beam contracts to a filament, self-phase modulation and self-steepening occur along with other nonlinear processes. Those processes broaden the spectrum of the input laser pulse. The input spectral width of the laser is  $\Delta\lambda \approx 35$  nm. The spectral broadening due to self-phase modulation can be estimated as  $\Delta\lambda \approx \phi_{spm} \Delta\lambda_0$ . [63] If the origin of  $z$  is taken as the input of the sapphire plate, the maximum nonlinear phase shift is given by:

$$\phi_{spm} = -\int_0^{z_{sf}} \frac{2\pi n_2}{\lambda_0} \frac{2\varepsilon}{\tau_p \pi w^2(z)} dz \approx -\frac{2\pi^2}{\lambda_0^2} \frac{n_2 \varepsilon}{\tau_p} \quad (6.4)$$

Using the same parameters as before, the nonlinear phase shift is  $\phi_{spm} \approx 10$ .

Accounting for linear and nonlinear dispersion, the spectral phases of the green and IR pulses at the start of the filament are given by:

$$\phi_{G,sf}(\omega) = \phi_{CE} + \Delta\phi_{n_0} + \Delta\phi_{n_2} + \phi_{spm} \approx \phi_{G,sf}(\omega_G) \quad (6.5)$$

$$\phi_{IR,sf}(\omega) = \phi_{CE} + \Delta\phi_{n_0} + \Delta\phi_{n_2} + \phi_{spm} \approx \phi_{IR,sf}(\omega_{IR}) \quad (6.6)$$

where  $\omega_{IR}$  and  $\omega_G = 2\omega_{IR}$  are the angular frequencies of the green and IR pulses and  $\phi_{CE}$  is the CE phase at the input of the sapphire plate.  $\Delta\phi_{n_0}$  is the CE phase shift caused by linear dispersion and is equal to  $\omega_0\Delta\tau_0$ , where  $\Delta\tau_0$  is the difference between the group and phase delay at the input carrier frequency  $\omega_0$ . The nonlinear contribution to the dispersion is given by  $\Delta\phi_{n_2} = -\phi_{spm} \omega_0 (dn_2/d\omega)_{\omega_0} / n_2$ . For sapphire, the parameters are  $\omega_0 (dn_2/d\omega)_{\omega_0} = 8 \times 10^{-17} \text{ cm}^2/\text{W}$  and  $n_2 = 2.9 \times 10^{-16} \text{ cm}^2/\text{W}$  at 800 nm. [37]

It is assumed the spectral phase difference between the green pulse and the IR pulse is only affected by the linear dispersion during the propagation in the filament. The justification is that the laser peak power decreases as the pulse duration increases during the propagation, making the nonlinear contributions negligible. Then, including the linear dispersion in the filament, the spectral phases become,

$$\phi_G(\omega) = \phi_{G,sf} - [\beta_G + \beta'_G(\omega - \omega_G)]z_{fila} \quad (6.7)$$

$$\phi_{IR}(\omega) = \phi_{IR,sf} - [\beta_{IR} + \beta'_{IR}(\omega - \omega_{IR})]z_{fila} \quad (6.8)$$

where the phase delay of the IR pulse and the green pulse are given by  $\beta_{IR}z_{fila} = z_{fila}n(\omega_{IR})\omega_{IR}/c$  and  $\beta_Gz_{fila} = z_{fila}n(\omega_G)\omega_G/c$  respectively. The group delay of the IR and the green pulses are given by  $\beta'_{IR}z_{fila} = [d\beta/d\omega]_{\omega_{IR}}z_{fila}$  and  $\beta'_Gz_{fila} = [d\beta/d\omega]_{\omega_G}z_{fila}$  respectively.

If the phase-matching of the second harmonic generation of the IR pulses is assumed to be perfect. The spectral phase of the second harmonic then becomes

$$\phi_{SHG}(\omega) = 2\phi_{IR,sf}(\omega_{IR}) - [2\beta_{IR} + \beta'_{IR}(\omega - \omega_G)]z_{fila} \quad (6.9)$$

The total phase then becomes

$$\Phi(\omega) = \phi_{CE} + \Delta\phi_{n_2} + \phi_{spm} + \omega_0\Delta\tau_0 + \omega_G\Delta\tau_{ph} - (\omega_G - \omega)\Delta\tau_g, \quad (6.10)$$

where the phase delay between the second harmonic and green pulses is

$$\Delta\tau_{ph} = z_{fila}(\beta_G/\omega_G - \beta_{IR}/\omega_{IR}) \text{ and the group delay is given by } \Delta\tau_g = z_{fila}[\beta'_G - \beta'_{IR}].$$

In the previous section, the change of the time delay with energy was identified as the major influence on the CE phase measurement error. [59]  $\Delta\tau_g$  in equation 6.10 represents that time delay.



Two fitting parameters were used for the model. First, the power was chosen to be 32% of the peak power of the input pulse. Second, the spot size was fitted as  $9.68 \pm 0.4 \mu\text{m}$ . For the CE phase measurement, the total phase,  $\Phi(\omega)$ , was measured at  $\omega \approx \omega_G$ , which leads to  $(\omega_G - \omega)\Delta\tau_g \approx 0$ . Therefore, the time delay fluctuation does not directly affect the CE phase measurement.

The model suggests that the measurement error is caused by the pulse-to-pulse variation of the quantity  $\Delta\phi_{err} = \Delta(\Delta\phi_{n_2} + \phi_{spm} + \omega_0\Delta\tau_0 + \omega_G\Delta\tau_{ph})$  due to power fluctuation. As the laser energy increases,  $\omega_G\Delta\tau_{ph}$  increases as the filament length,  $z_{fila}$ , increases; whereas,  $\omega_0\Delta\tau$  decreases as the shortening of  $z_{sf}$  which cancels the effects of  $\omega_G\Delta\tau_{ph}$  to a large degree as our calculation shows. The nonlinear term,  $\phi_{spm}$ , also counters the effects of  $\omega_G\Delta\tau_{ph}$ . However, the overall result is that  $\Delta\phi_{err}$  increases with laser energy. This explains the measured decrease of  $\Delta\phi_{CE} = -\Delta\phi_{err}$  with laser energy when  $\Phi(\omega_G)$  was locked to zero.

Thus, a simple model which describes the CE phase measurement error on laser energy fluctuations was derived. The model can be used to describe the results obtained in the previous sections.

## CHAPTER 7 - Few-Cycle Pulses and CE Phase

### 7.1 CE Phase Measurement using Few-Cycle Pulses

Previously, 5.6 fs, 1.2 mJ pulses were generated by spectrally broadening pulses in a neon-filled hollow-core fiber. [11] Also, the CE phase stability of the pulses before and after the fiber was measured. The experimental setup used in that research is shown in Figure 7.1.

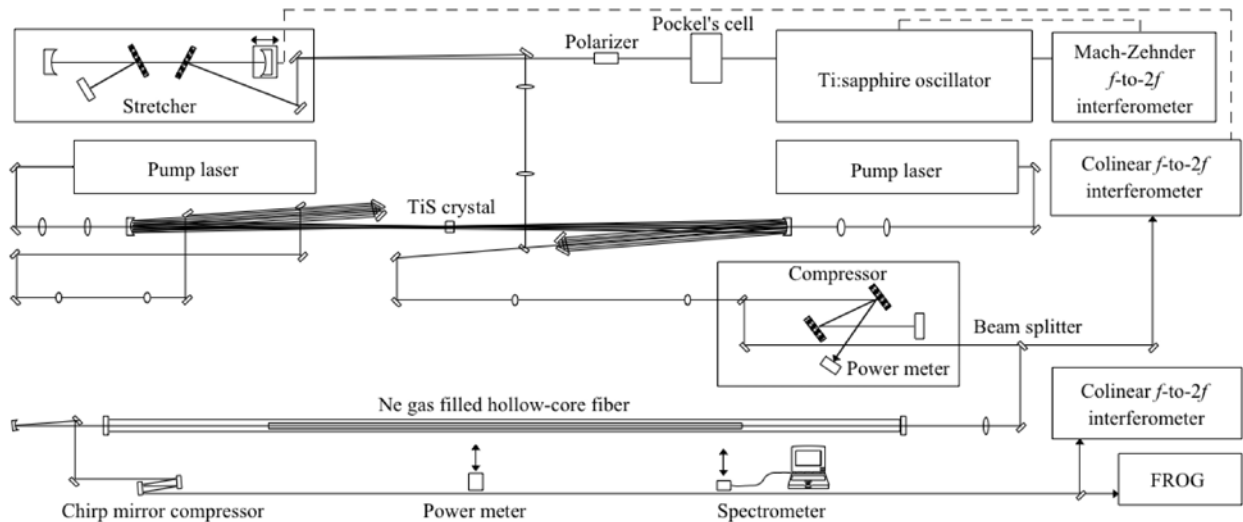


**Figure 7.1 Setup for Measuring CE phase stability of few-cycle pulses.**

In the experiment, the CE phase stable pulses from the laser oscillator were amplified to 2.5 mJ using the KLS amplifier. The 0-order diffraction from the compressor grating was used for the power locking system. 10% of the amplifier output was used for measuring the CE phase drift of the pulses using the in-loop  $f$ -to- $2f$  interferometer. The signal was used to correct the CE phase drift by feedback controlling the stretcher grating separation.

The remaining 2.2 mJ of the amplifier output was focused into a  $\sim 1$  m long hollow-core fiber filled with neon gas at a pressure of 3 bars. The output of the fiber was collimated by a focusing mirror and sent to a set of chirped mirrors for temporal compression. A FROG (Frequency-Resolved Optical Gating) was used to measure the pulse duration of the pulses after the fiber. [64] The input and output spectra are shown in Figure 7.2 along with the measured pulse duration.

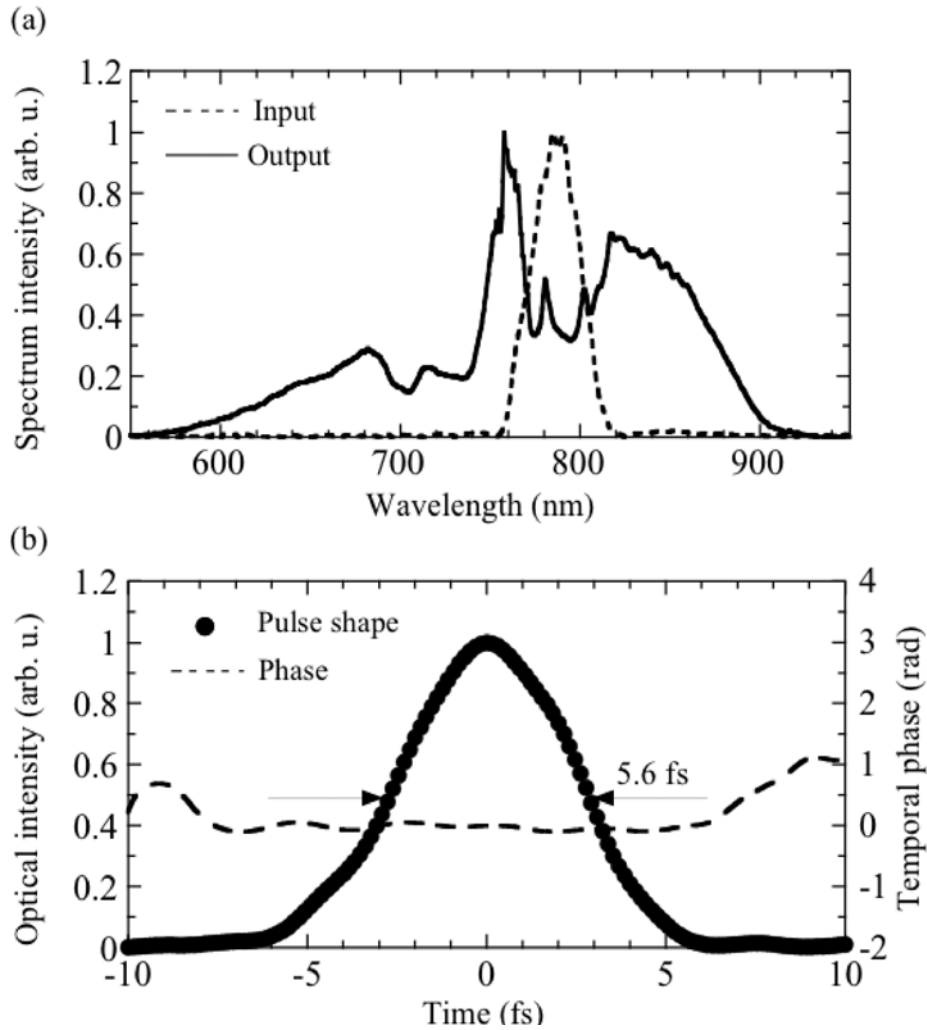


**Figure 7.2 Top: Input and output spectra. Bottom: Measured pulse duration.**

The pulses from the fiber had energy of 1.2 mJ, which was measured by a power meter placed after the fiber. The power meter was also used to measure the power stability of the few-cycle pulses.

An  $f$ -to- $2f$  interferometer was placed after the fiber to measure the CE phase stability of the pulses. In the first measurement, the CE phase of the pulses before the fiber was measured and stabilized. Also, the power locking system was engaged, giving a power stability of 0.6% before the fiber and 1.4% after the fiber. The larger fluctuation after the fiber was due to beam pointing jitter at the input of the fiber. The CE phase was locked to 189 mrad rms error before the fiber. After the fiber, the measured CE phase error was 370 mrad rms. The results are shown in Figure 7.3

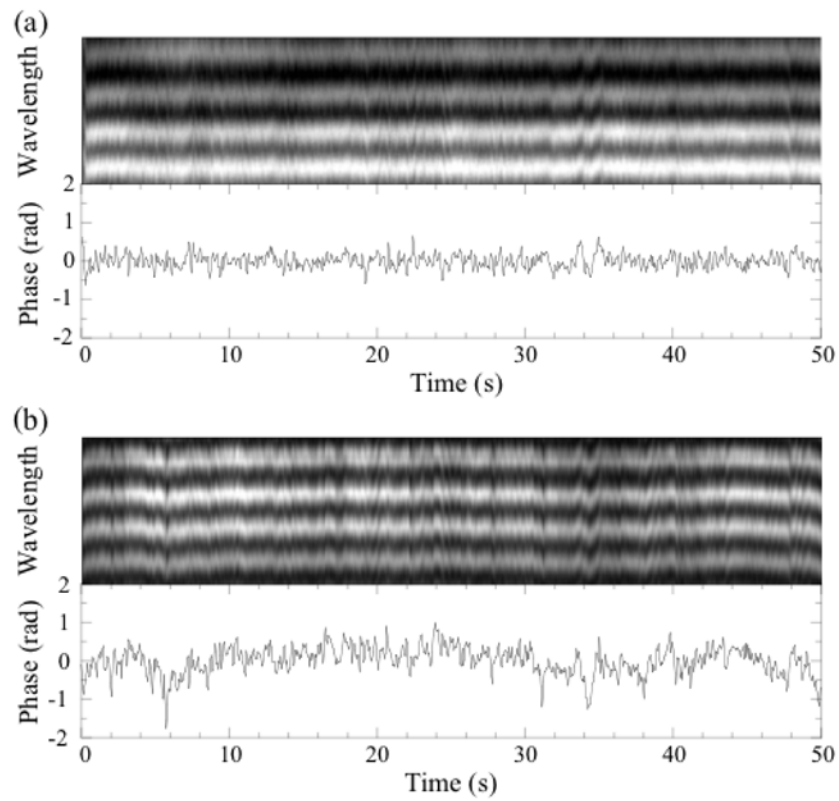


**Figure 7.3 a) CE phase fringes and phase drift of the pulses before the fiber. b) CE phase fringes and phase drift of the pulses after the fiber. The power was locked to 0.6% before the fiber.**

Alternately, the CE phase stability was measured when the power locking was disengaged. The results are shown in Figure 7.4.

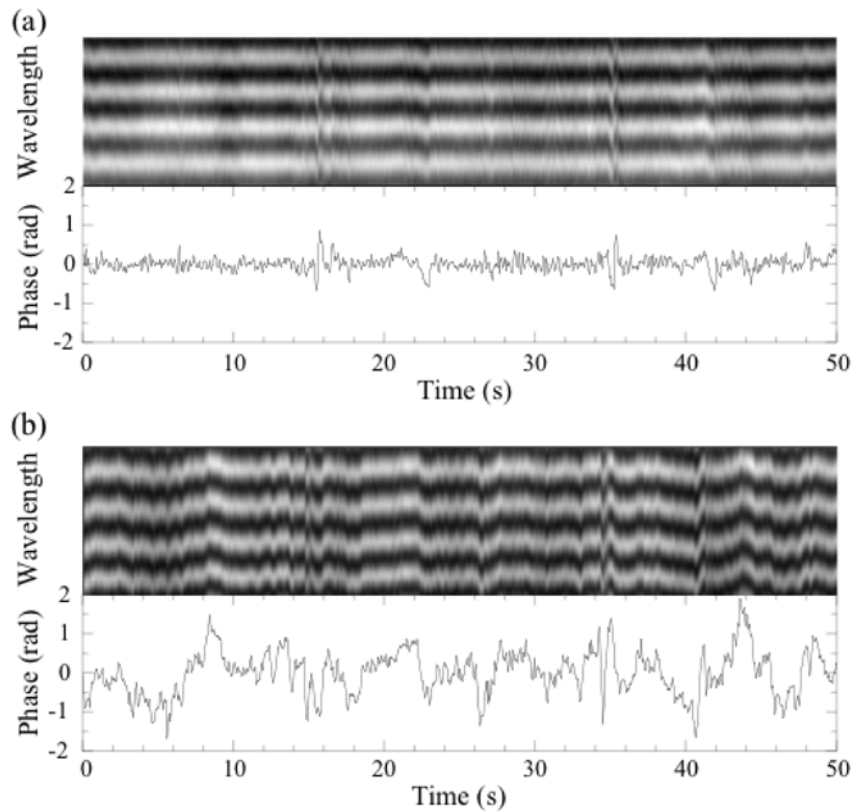


**Figure 7.4 a) CE phase fringes and phase drift of the pulses before the fiber. b) CE phase fringes and phase drift of the pulses after the fiber. The power stability was 1.5% before the fiber.**

In this result, the power stability was 1.5% before the fiber and 2.5% after the fiber. The CE phase was locked to 195 mrad rms error before the fiber. After the fiber, though, the CE phase error was 567 mrad rms. The higher error after the fiber was due to the 2.5% fluctuation of the power. Since the  $f$ -to- $2f$  interferometer was using a sapphire plate to spectrally broaden the pulses from the fiber over an octave, the power fluctuation significantly affected the CE phase measurement.

In order to estimate the CE phase fluctuation from the nonlinear interaction in the fiber, the fiber was pumped down to vacuum. Also, the power was locked, giving a 0.6% fluctuation before the fiber and a 1.2% fluctuation after the fiber. The results are shown Figure 7.5.

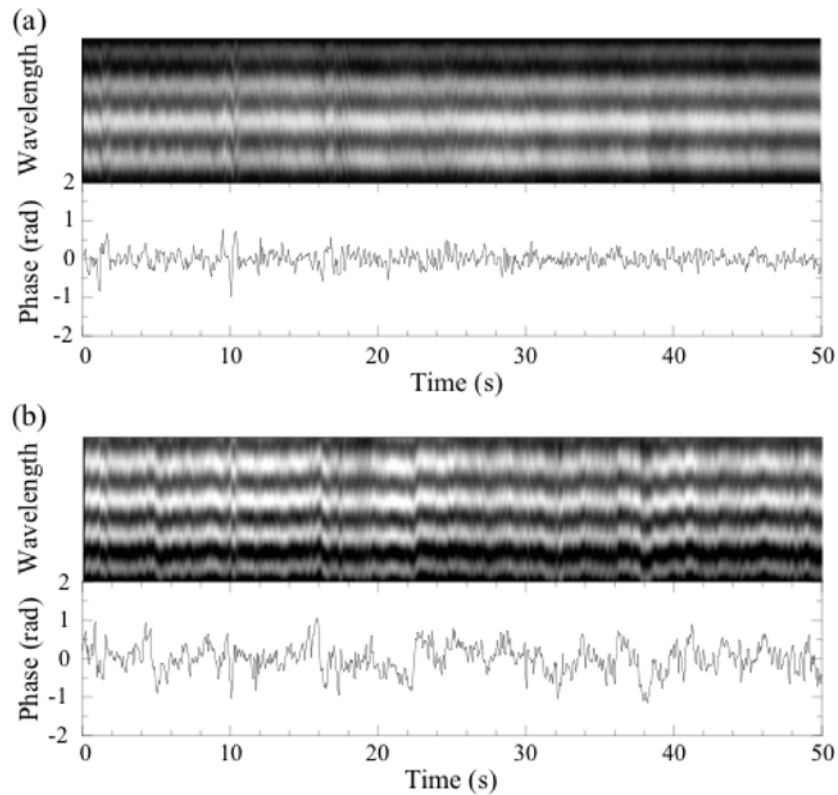


**Figure 7.5 a) CE phase fringes and phase drift of the pulses before the fiber. b) CE phase fringes and phase drift of the pulses after the fiber. The power stability was 0.6% before the fiber.**

The CE phase stability of the pulses before the fiber was 195 mrad rms. After the fiber, the CE phase stability was 372 mrad rms. The results with the fiber operating at vacuum were comparable to the results when the fiber was filled with neon gas and the power was locked. This indicated that the nonlinear interaction in the fiber did not contribute much to the CE phase instability.

Thus, it was shown that the power fluctuation of the few-cycle pulses from the hollow-core fiber was the major source of noise on the CE phase measurement. The power fluctuation could be improved by improving the beam pointing stability on the input side of the fiber. The limitation of this work, though, was that the contribution from the nonlinear interaction in the fiber could not be thoroughly investigated due to power fluctuations during the CE phase measurement.

## 7.2 Measurement of CE Phase Error from the Fiber

In order to measure the CE phase error that is due to the nonlinear interaction in the fiber, an octave-spanning spectrum was generated directly from the fiber. An  $f$ -to- $2f$  measurement was then performed using the octave-spanning spectrum. [65] Since the spectrum after the fiber was already very broad, the sapphire plate was removed from the interferometer. CE phase error due to power fluctuations was avoided in the measurement. [66]

In the experiment, 2.2 mJ energy, 1 kHz, ~35 fs pulses from the KLS amplifier were focused into a hollow-core fiber filled with neon gas at a pressure of 2 bars. A fused silica plate was placed before the fiber to pick off a portion of the beam for monitoring the input power to the fiber. Also, 10% of the beam before the fiber was split off and sent to an  $f$ -to- $2f$  interferometer using a sapphire plate to broaden the spectrum of the pulses. The interferometer was used to measure the CE phase stability of the pulses before the fiber. The power was locked to within 0.5% rms before the fiber.

The pulses from the fiber were focused into a 100 $\mu$ m thick BBO crystal, where the wavelengths around 900 nm were frequency doubled. Since the pulses from the fiber were not temporally compressed, the large group delay between the wavelength centered at 450 nm and the frequency doubled components centered at 900 nm produced fringes in the wavelength domain. A spectrometer recorded the fringes for measurement of the CE phase. A BG3 filter was used to block the components of the spectrum above 500 nm in order to prevent saturation of the spectrometer.

The CE phase before the fiber was locked to 98 mrad. After the fiber, the drift had increased to 137 mrad. Previously, the CE phase stability of the pulses after the fiber had been measured to a value of 370 mrad using a sapphire plate based  $f$ -to- $2f$ . By removing the sapphire plate, the measurement error had been reduced by almost a factor of 2. Errors from power fluctuations did not affect the measurement.

In the second experiment, the measured CE phase error of the pulses from the fiber was used to feedback control to the stretcher. The sapphire plate based  $f$ -to- $2f$  was used to measure any added CE phase instability from the fiber.

The results show that the CE phase was locked to an in-loop accuracy of 94 mrad rms. The out-loop measurement showed that the CE phase was locked to 134 mrad rms. This

indicated that the fiber did not introduce a significant amount of CE phase error when the power of the input pulses was locked to 0.5% rms.

For the sapphire plate, it was shown that a 1% power fluctuation caused a 160 mrad error, which is larger than that for the hollow-core fiber. This can be explained by the fact that the nonlinear interaction in the fiber occurs over a long distance ( $\sim 1$  m); whereas, the self-focusing and filamentation in the sapphire plate occur over 2.3 mm. CE phase measurement error is more susceptible to the strong self-focusing than to the long interaction length in the fiber.



## CHAPTER 8 - Applications

### 8.1 Stereo-Above-Threshold Ionization Detection of the CE Phase

CE phase stabilized few-cycle pulses were used to study CE phase effects in stereo-above threshold ionization (ATI) and in high-harmonic generation (HHG). The results with the stereo-ATI setup were obtained using laser pulses from a grating-based amplifier. [18] This was the first demonstration of CE phase effects in a strong field atomic physics experiment using such an amplifier.

The experimental setup for the ATI study is shown in Figure 8.1

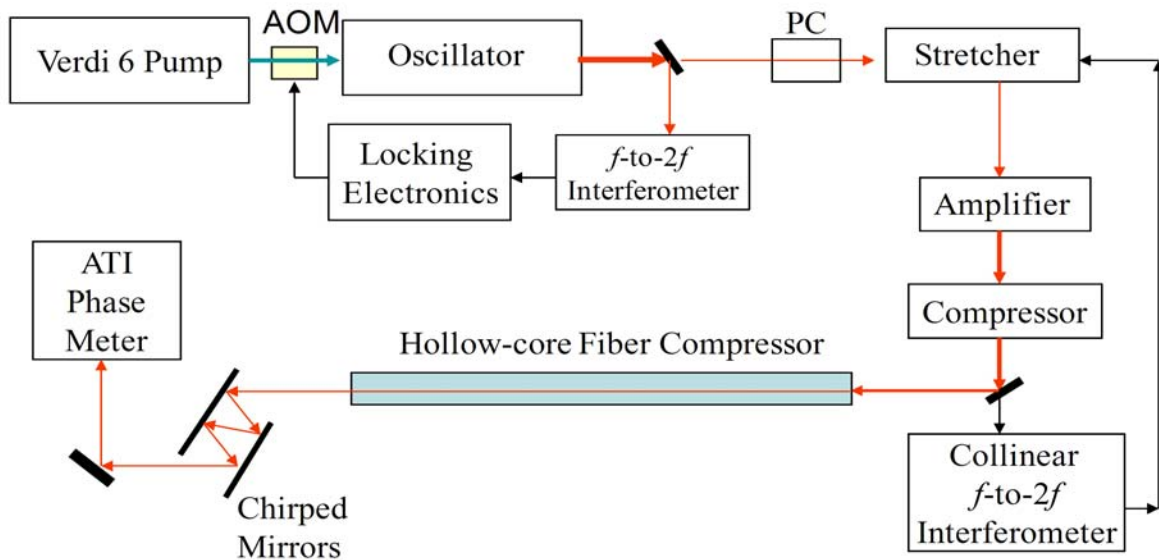


**Figure 8.1** Experimental setup for determining the CE phase of few-cycle pulses.

In the experiment, the pulses from the hollow-core fiber were temporally compressed to 6 fs in duration by a set of chirped mirrors. A small portion (5%) was rotated to horizontal polarization by a half-waveplate and focused into a chamber filled with Xe gas. A pair of microchannel plates (MCP) was placed on opposite sides of the chamber. The MCP's detected the counts of photoionized electrons. [1]

The direction the electron was emitted depended on the value of the CE phase of the ionizing laser pulse. A pair of thin fused-silica wedges was placed before the chamber to change the CE phase of the incident laser pulses. The ratio of electron yields detected by the right and left MCP's was used to measure the CE phase. This particular setup was called a stereo-ATI phase meter.

During the experiment, the CE phase before the fiber was stabilized to 174 mrad rms over a 10 minute period. The results for the phase meter are shown in Figure 8.2.

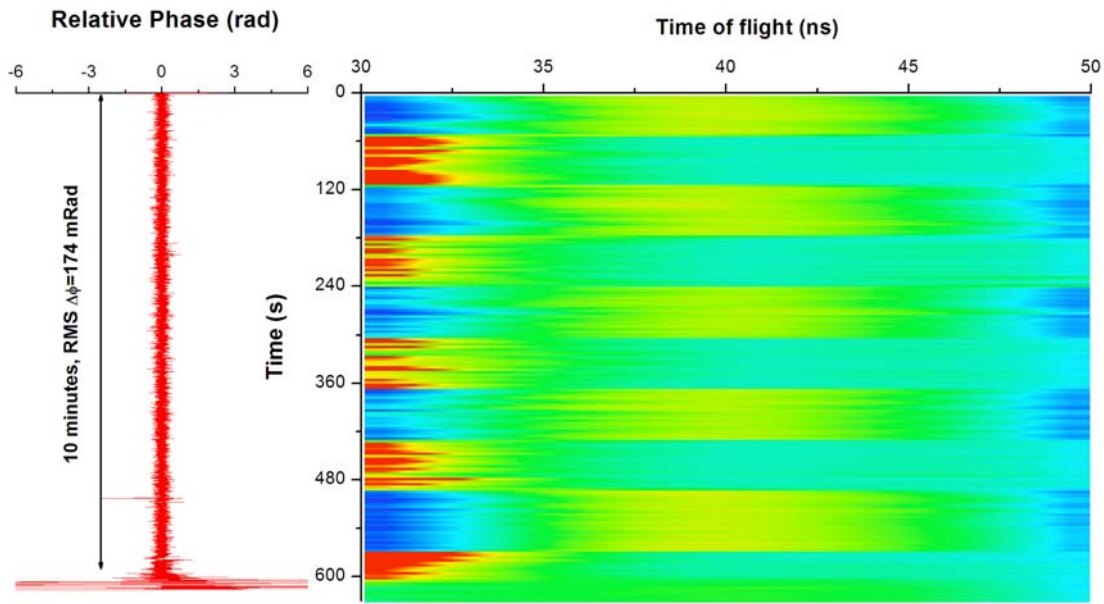


**Figure 8.2 Left) CE phase drift before the hollow-core fiber. Right) Phase meter results**

The phase meter result is shown in the time-of-flight spectrum. In the plot, the ratio of right (R) and left (L) electron yields  $(L-R)/(L+R)$  is plotted. Every 60 seconds, the laser pulse CE phase was changed by  $\pi$  by moving the wedge pair. Since the yield of high energy electrons was more sensitive than that of the low energy electrons to the CE phase, the time-of-flight spectrum shows a higher contrast for the short time-of-flight (30-34 ns) than in the long range.

The data shows the dependence of the ATI process on the CE phase as the yield changed as the CE phase was changed by  $\pi$ . The data also displays the good CE phase stability of the laser system.

## 8.2 XUV Attosecond Pulses

Attosecond XUV pulses can be generated by focusing a linearly polarized, high intensity ( $\sim 4 \times 10^{16} \text{ W/cm}^2$ ) laser pulses into a noble gas. When this occurs, odd harmonics, up to hundreds, of the driving laser field emerge in the output beam. [67,68] The process is called high-harmonic generation. For driving laser pulses approaching a single-cycle, the harmonic peaks in the cutoff region merge into a continuum. For multi-cycle lasers, the HHG process produces a train of attosecond pulses. [69]

A technique was developed for generating isolated attosecond pulses using multi-cycle lasers. The technique was called double-optical gating (DOG). [70] Using the DOG process, the effects of CE phase on the high harmonic spectrum were studied. CE phase stabilized  $\sim 9$  fs pulses were used to generate high-harmonic spectra and the grating separation in the KLS stretcher was varied to change the CE phase.

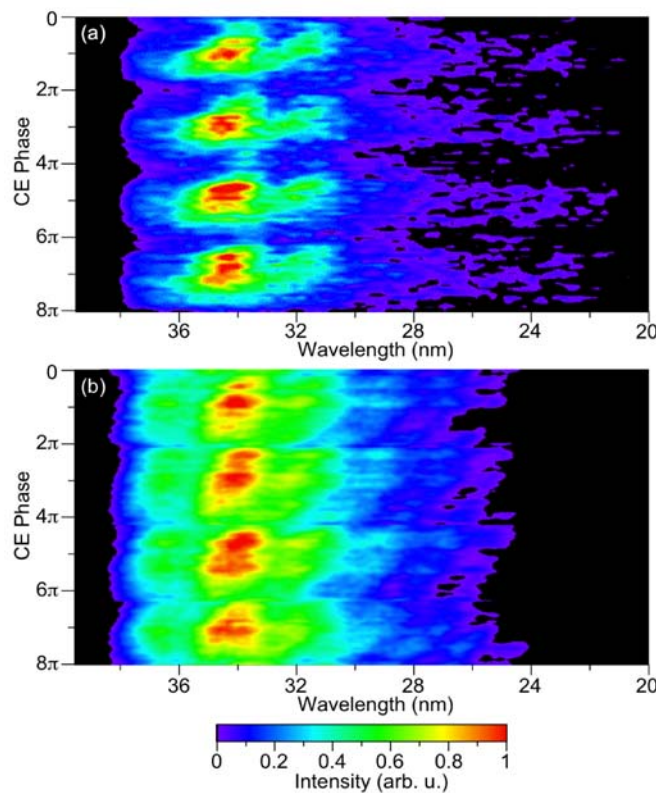


**Figure 8.3** Effects of CE phase on HHG spectra obtained using DOG.

The top plot was obtained by using a collinear DOG setup and the bottom plot was obtained using an interferometer DOG. As the CE phase was changed, the individual harmonics merged into a continuum. Since the attosecond XUV bursts were generated during a single-cycle or less of the driving field, the CE phase dependence exhibits strong features. Due to the asymmetry of the driving laser field, which consisted of an IR pulse and a second-harmonic pulse, the XUV emission exhibited a  $2\pi$  CE phase dependence. [22]

The important result is that CE phase dependence in the HHG process was studied by varying the grating separation of the laser amplifier. The result also displays the high CE phase stability of the laser system.

## CHAPTER 9 - Conclusions

In summary, a powerful tool for studying ultrafast processes was developed in this research. The CE phase evolution of the pulse train from a Ti:Sapphire laser oscillator was stabilized. Previously, the CE phase noise introduced by the path length drift in the  $f$ -to- $2f$  interferometer used to obtain the offset frequency was not addressed. In this research, the noise was quantitatively characterized. A HeNe laser was copropagated in the interferometer and the interference signal was used to measure the path length fluctuation and to stabilize the path length drift. The noise was found to be suppressed by several orders of magnitude.

The CE phase stable pulses from that oscillator were amplified to 2.5 mJ in a grating-based chirped-pulse amplifier. By measuring the CE phase drift of the amplified laser pulses, the drift was able to be corrected by changing the grating separation in the stretcher. Previous research used material-based CPA systems and precompensated the CE phase drift of the amplified laser pulses using the oscillator locking electronics. It was also found that by changing the grating separation to a set value, the CE phase could be shifted to any point within a  $2\pi$  range. If the stretcher optics are inadequate for mounting on a PZT stage, the compressor can be used. Using the KLSII amplifier, the CE phase was shown to be stabilized by changing the grating separation in the compressor. Furthermore, stabilization of the path length drift of the interferometer for the oscillator CE phase stabilization reduced the fast ( $>3$  Hz) CE phase drift of the amplified laser pulses by 40%. The grating stretcher or compressor control would not be able to reduce the fast drift. Stabilization of the path length drift increased the CE phase stability of the system. Future research might focus on other sources of fast CE phase drift either at the oscillator CE phase stabilization stage or in the amplifier.

CE phase measurement error in the sapphire-plate based  $f$ -to- $2f$  interferometer was found to be significant. With the addition of a power-locking scheme and an out-loop interferometer, the energy fluctuation of the amplified laser pulses was found to be a significant source of error. By modulating the power to the in-loop interferometer with the power locked and measuring the CE phase drift with the out-loop, the phase-energy coupling coefficient was measured to be 160

mrad per 1% change in laser energy. Previously, other groups assumed the  $f$ -to- $2f$  measurement was sufficient enough for stabilizing the phase. However, the research in this thesis showed that the error from laser energy fluctuation was very significant. A two-step model explaining the coupling between the energy and the CE phase was proposed. The model accounts for the self-focusing in the sapphire plate and the subsequent propagation of the filament. Originally, the variation of the group delay with laser energy was thought to be the main source of error in the CE phase measurement. However, the model showed that the CE phase error was not sensitive to the delay change. The nonlinear dispersion, the nonlinear phase shift, phase delay between the IR and SHG pulses, and the delay of the input pulse were found to contribute to the CE phase error.

Similarly, the CE phase stability of few-cycle pulses from a hollow-core fiber chirped mirror compressor was studied. In the first case, the 5.6 fs pulses from the fiber were sent to a sapphire plate based interferometer. The pulses from the fiber had a large spectrum, but not an octave-spanning spectrum. The sapphire plate was used to obtain the octave-spanning spectrum. The power fluctuation of the pulses from the fiber was 1.5% when the amplifier power was locked. This led to a large CE phase error. In the second case, an octave-spanning spectrum was obtained directly from the fiber. The sapphire plate was then removed since no further spectral broadening was needed. The CE phase stability was found to be significantly improved. This was due to the removal of the sapphire plate. Future research might involve splitting a portion of the beam from the fiber for CE phase stabilization. Also, a model for the coupling mechanism in the fiber, similar to that for the sapphire plate, could be developed.

Finally, CE phase stabilized few-cycle pulses were used to perform stereo-ATI, which gave a measure of the CE phase stability of the laser system. The results indicated, qualitatively, that the CE phase of the laser system was very stable. This was also the first measurement of a CE phase sensitive strong field process using pulses from a CE phase stabilized grating-based amplifier. By changing the CE phase using the grating separation in the stretcher, the effects of CE phase on HHG were studied. As the CE phase was changed, the individual harmonics merged into a continuum. The results further showed the CE phase stability of the laser system.

## References

- [1] G.G. Paulus, F. Grasbon, H. Walther, P. Villoresi, M. Nisoli, S. Stagira, E. Priori, and S. De Silvestri, *Nature (London)* **414**, 182 (2001).
- [2] C. A. Haworth, L. E. Chipperfield, J. S. Robinson, P. L. Knight, J. P. Marangos and J. W. G. Tisch, *Nature Physics* **3**, 52 (2007).
- [3] G. Sansone, C. Vozzi, S. Stagira, M. Pascolini, L. Poletto, P. Villoresi, G. Tondello, S. De Silvestri, and M. Nisoli, *Phys. Rev. Lett.* **92**, 113904 (2004).
- [4] V. Roudnev, B.D. Esry, and I. Ben-Itzhak, *Phys. Rev. Lett.* **93**, 163601 (2004).
- [5] C. Lemell, X.-M. Tong, F. Krausz, and J. Burgdörfer, *Phys. Rev. Lett.* **90**, 076403 (2003).
- [6] M. Kriebel, T. Löffler, M.D. Thomson, R. Dörner, H. Gimpel, K. Zrost, T. Ergler, R. Mashhammer, U. Morgner, J. Ullrich, and H.G. Roskos, *Nat. Phys.* **2**, 327 (2006).
- [7] T. M. Fortier, P.A. Roos, D.J. Jones, S.T. Cundiff, R.D.R. Bhat, and J.E. Sipe, *Phys. Rev. Lett.* **92**, 147403 (2004).
- [8] W.-J. Chen, Z.-M. Hsieh, S.W. Huang, H.-Y. Su, C.-J. Lai, T.-T. Tang, C.-H. Lin, C.-K. Lee, R.-P. Pan, C.-L. Pan, and A.H. Kung, *Phys. Rev. Lett.* **100**, 163906 (2008).
- [9] Femtolasers FEMTOSOURCE™ RAINBOW™ at [www.femtolasers.com](http://www.femtolasers.com)
- [10] M. Nisoli, S. De Silvestri, O. Svelto, R. Szipöcs, K. Ferencz, Ch. Spielmann, S. Sartania, and F. Krausz, *Opt. Lett.* **22**, 522 (1997).
- [11] H. Mashiko, C.M. Nakamura, C. Li, E. Moon, H. Wang, J. Tackett, and Z. Chang, *Appl. Phys. Lett.* **90**, 161114 (2007).
- [12] J. H. Sung, J. Y. Park, T. Imran, Y.S. Lee, C. H. Nam, *Appl. Phys. B: Laser Opt.* **82**, 5 (2006).

- [13] A. Couairon, J. Biegert, C. P. Hauri, W. Kornelis, F. W. Helbing, U. Keller, and A. Mysyrowicz, *Journ. Mod. Opt.* **53**, 75 (2006).
- [14] G. Stibenz, N. Zhavoronkov, and G. Steinmeyer, *Opt. Lett.* **31**, 274 (2006).
- [15] H. Wang, Y. Wu, C. Li, H. Mashiko, S. Gilbertson, and Z. Chang, *Opt. Express* **16**, 14449 (2008).
- [16] A. Baltuška, M. Uiberacker, E. Goulielmakis, R. Kienberger, V.S. Yakovlev, T. Udem, T.W. Hänsch, and F. Krausz, *IEEE J. Quantum Electron.* **9**, 972 (2003).
- [17] E. Moon, C. Li, Z. Duan, J. Tackett, K.L. Corwin, B.R. Washburn, and Z. Chang, *Opt. Express* **14**, 9758 (2006).
- [18] C. Li, E. Moon, H. Mashiko, C.M. Nakamura, P. Ranitovic, C.M. Maharjan, C.L. Cocke, Z. Chang, and G.G. Paulus, *Opt. Express* **14**, 11468 (2006).
- [19] C. Li, H. Mashiko, H. Wang, E. Moon, S. Gilbertson, and Z. Chang, *Appl. Phys. Lett.* **92**, 191114 (2008).
- [20] H. Wang, C. Li, J. Tackett, H. Mashiko, C.M. Nakamura, E. Moon, and Z. Chang, *Appl. Phys. B: Lasers Opt.* **89**, 275 (2007).
- [21] C. Li, E. Moon, H. Mashiko, H. Wang, C.M. Nakamura, J. Tackett, and Z. Chang, *Appl. Opt.* (submitted).
- [22] S. Gilbertson, H. Mashiko, C. Li, S.D. Kahn, M.M. Shakya, E. Moon, and Z. Chang, *Appl. Phys. Lett.* **92**, 071109 (2008).
- [23] A. Ducasse, C. Rullière, and B. Couillaud, “Methods for the Generation of Ultrashort Laser Pulses: Mode-Locking,” in *Femtosecond Laser Pulses*, 2<sup>nd</sup> ed., (Springer 2005), pp. 57-85.
- [24] S.T. Cundiff, J. Ye, and J.L. Hall, *Rev. Sci. Instrum.* **72**, 3749 (2001).



- [25] J.-C. Diels, W. Rudolph, “Ultrashort Sources II: Examples,” in *Ultrashort Laser Pulse Phenomena: Fundamentals, Techniques, and Applications on a Femtosecond Time Scale*, 2<sup>nd</sup> ed., (Elsevier 2006), pp. 360.
- [26] A.E. Siegman, *Lasers*, 2<sup>nd</sup> ed., (University Science Books 1986), pp. 1041-1050.
- [27] S.T. Cundiff, *J. Phys. D: Appl. Phys.* **35** R43 (2002).
- [28] L. Xu, Ch. Spielmann, A. Poppe, T. Brabec, F. Krausz, and T.W. Hänsch, *Opt. Lett.* **21**, 2008 (1996).
- [29] H.R. Telle, G. Steinmeyer, A.E. Dunlop, J. Stenger, D.H. Sutter, and U. Keller, *Appl. Phys. B: Lasers Opt.* **69**, 327 (1999).
- [30] J.K. Ranka, R.S. Windeler, and A.J. Stentz, *Opt. Lett.* **25**, 25 (2000).
- [31] A. Apolonski, A. Poppe, G. Tempea, Ch. Spielmann, Th. Udem, R. Holtzwarth, T.W. Hänsch, and F. Krausz, *Phys. Rev. Lett.* **85**, 740 (2000).
- [32] D.J. Jones, S.A. Diddams, J.K. Ranka, A. Stentz, R.S. Windeler, J.L. Hall, and S.T. Cundiff, *Science* **288**, 635 (2000).
- [33] S. Rausch, T. Binhammer, A. Harth, J. Kim, R. Ell, F.X. Kärtner, and U. Morgner, *Opt. Express* **16**, 9739 (2008).
- [34] J. Ye, S.T. Cundiff, S. Foreman, T.M. Fortier, J.L. Hall, K.W. Holman, D.J. Jones, J.D. Jost, H.C. Kapetyan, K.A.H. V. Leeuwen, L.S. Ma, M.M. Murnane, J.L. Peng, and R.K. Shelton, *Appl. Phys. B: Lasers Opt.* **74**, S27 (2002).
- [35] Y.S. Lee, J.H. Sung, C.H. Nam, T.J. Yu, and K.-H. Hong, *Opt. Express* **13**, 2969 (2005).
- [36] T.M. Fortier, D.J. Jones, J. Ye, and S.T. Cundiff, *IEEE J. Quantum Electron.* **9**, 1002 (2003).
- [37] F.W. Helbing, G. Steinmeyer, and U. Keller, *IEEE J. Quantum Electron.* **9**, 1030 (2003).

- [38] K.W. Holman, R.J. Jones, A. Marian, S.T. Cundiff, and J. Ye, *IEEE J. Quantum Electron.* **9**, 1018 (2003).
- [39] A. Rundquist, C. Durfee, Z. Chang, G. Taft, E. Zeek, S. Backus, M.M. Murnane, H.C. Kapetyan, I. Christov, and V. Stoev, *Appl. Phys. B: Lasers Opt.* **65**, 161 (1997).
- [40] A. Apolonski, B. Povazay, A. Unterhuber, W. Drexler, W.J. Wadsworth, J.C. Knight, and P. St. J. Russell, *J. Opt. Soc. Am. B*, **19**, 2165 (2002).
- [41] Menlosystems XPS 800 Locking Electronics Manual.
- [42] IntraAction Corp. Acousto-Optic Modulator Manual.
- [43] R. Paschotta, *Appl. Phys. B: Lasers Opt.* **79**, 153-162 (2004).
- [44] T.M. Fortier, D.J. Jones, J. Ye, S.T. Cundiff, and R.S. Windeler, *Opt. Lett.* **27**, 1436 (2002).
- [45] M. Kakehata, H. Takada, Y. Kobayashi, K. Torizuka, H. Takamiya, K. Nishijima, T. Homma, H. Takahashi, K. Okubo, S. Nakamura, and Y. Koyamada, *Opt. Express* **12**, 2070 (2004).
- [46] M. Mehendale, S.A. Mitchell, J.-P. Likforman, D.M. Villeneuve, and P.B. Corkum, *Opt. Lett.* **25**, 1672 (2000).
- [47] M. Kakehata, H. Takada, Y. Kobayashi, K. Torizuka, Y. Fujihira, T. Homma, and H. Takahashi, *Opt. Lett.* **26**, 1436 (2001).
- [48] M. Kakehata, Y. Fujihira, H. Takada, Y. Kobayashi, K. Torizuka, T. Homma, and H. Takahashi, *Appl. Phys. B: Lasers Opt.* **74**, S43 (2002).
- [49] G.G. Paulus, F. Lindner, H. Walther, A. Baltuška, E. Goulielmakis, M. Lezius, and F. Krausz, *Phys. Rev. Lett.* **91**, 253004 (2003).
- [50] D. Strickland and G. Mourou, *Opt. Commun.* **62**, 419 (1985).

- [51] F. Salin. “How to Manipulate and Change the Characteristics of Laser Pulses,” in *Femtosecond Laser Pulses*, 2<sup>nd</sup> ed., (Springer 2005), pp. 181-183.
- [52] A.E. Siegman, *Lasers*, 2<sup>nd</sup> ed., (University Science Books 1986), pp. 384.
- [53] A.W. Albrecht, J.D. Hybl, S.M.G. Faeder, and D.M. Jonas, *J. Chem. Phys.* **111**, 10934 (1999).
- [54] L. Lepetit, G. Cheriaux, and M. Joffre, *J. Opt. Soc. Am. B* **12**, 2467 (1995).
- [55] B. Shan, C. Wang, and Z. Chang, U.S. Patent No. 7,050,474 (23 May 2006).
- [56] Z. Chang, *Appl. Opt.* **45**, 8350 (2006).
- [57] C. Li, E. Moon, and Z. Chang, *Opt. Lett.* **31**, 3113 (2006).
- [58] E. Gagnon, I. Thomann, A. Paul, A.L. Lytle, S. Backus, M.M. Murnane, H.C. Kapetyan, and A.S. Sandhu, *Opt. Lett.* **31**, 1866 (2006).
- [59] C. Li, E. Moon, H. Wang, H. Mashiko, C.M. Nakamura, J. Tackett, and Z. Chang, *Opt. Lett.* **32**, 796 (2007).
- [60] T.M. Fortier, J. Ye, S.T. Cundiff, R.S. Windeler, *Opt. Lett.* **27**, 445 (2002).
- [61] S.L. Chin, S.A. Hosseini, W. Liu, Q. Luo, F. Théberge, N. Aközbek, A. Becker, V.P. Kandidov, O.G. Kosareva and H. Schroeder, *Can. Journ. Phys.* **83**, 863 (2005).
- [62] R. W. Boyd, *Nonlinear Optics* (Academic Press, 2003).
- [63] G. P. Agrawal, *Nonlinear Fiber Optics*, Third Edition (Academic Press, 2001).
- [64] R. Trebino and D.J. Kane, *J. Opt. Soc. Am. A* **10**, 1101 (1993).
- [65] H. Wang, E. Moon, M. Chini, H. Mashiko, C. Li, and Z. Chang, *Appl. Phys. Lett.* (Submitted).
- [66] A. Ishizawa and H. Nakano, *Jpn. J. Appl. Phys.* **44**, 6039 (2005).
- [67] P. B. Corkum, *Phys. Rev. Lett.* **71**, 1994 (1993).

- [68] K. C. Kulander, K. J. Schafer, and J. L. Krause, *Super-Intense Laser-Atom Physics*, NATO ASI, Ser. B, Vol. **316**, Page 95, Plenum: New York (1993).
- [69] P. M. Paul, E. S. Toma, P. Breger, G. Mullot, F. Audebert, Ph. Balcou, H. G. Muller, and P. Agostini, *Science* **292**, 1689 (2001).
- [70] H. Mashiko, S. Gilbertson, C. Li, S.D. Kahn, M.M. Shakya, E. Moon, and Z. Chang, *Phys. Rev. Lett.* **100**, 103906 (2008).

## Appendix A - Code for Stabilizing the Amplifier CE Phase

The code used to calculate the measured CE phase drift was written in Labview 6.2. For confidentiality reasons, the entirety of the code cannot be published here. However, the basic function of the code will be outlined.

First, the front panel of the Labview program is shown.

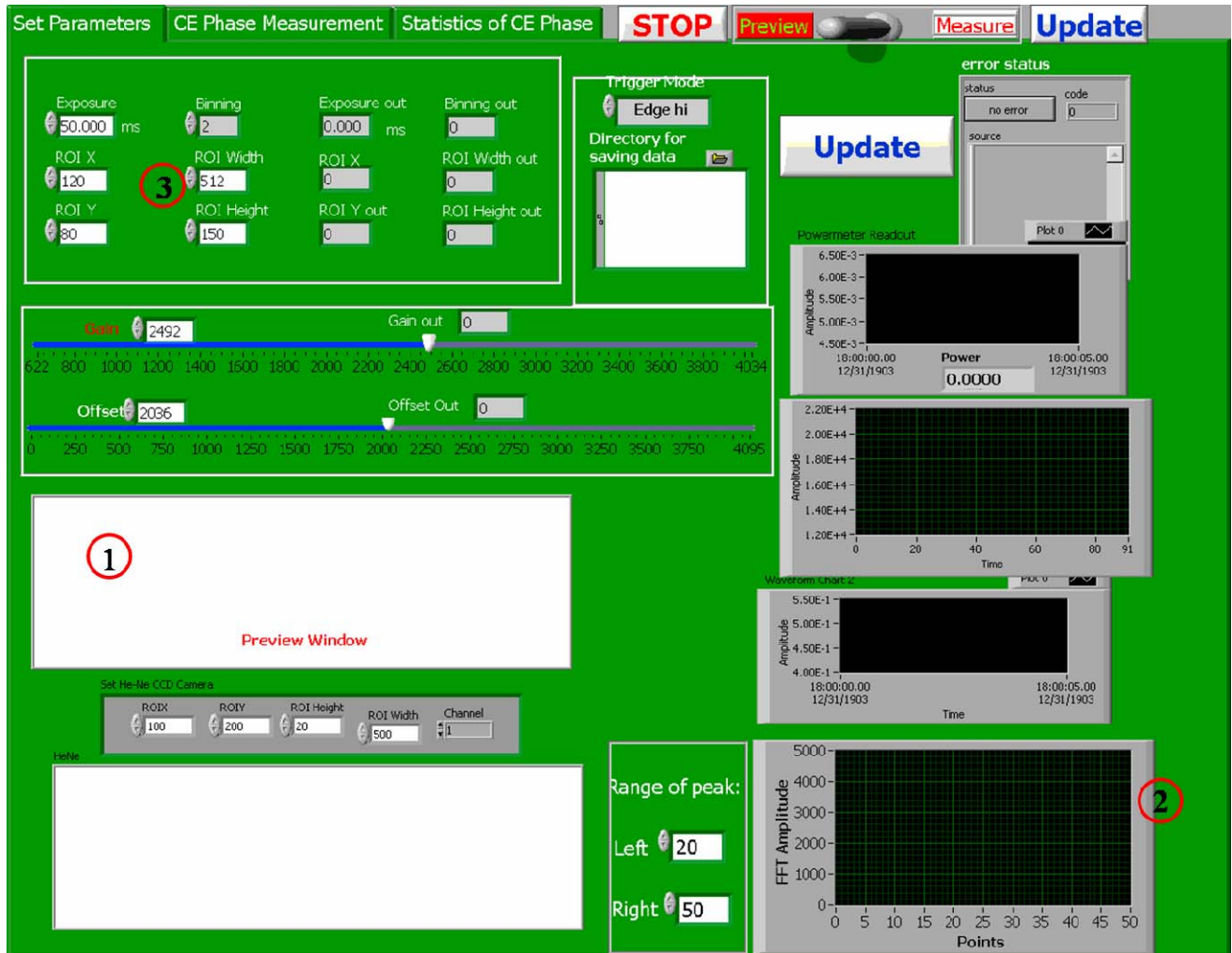
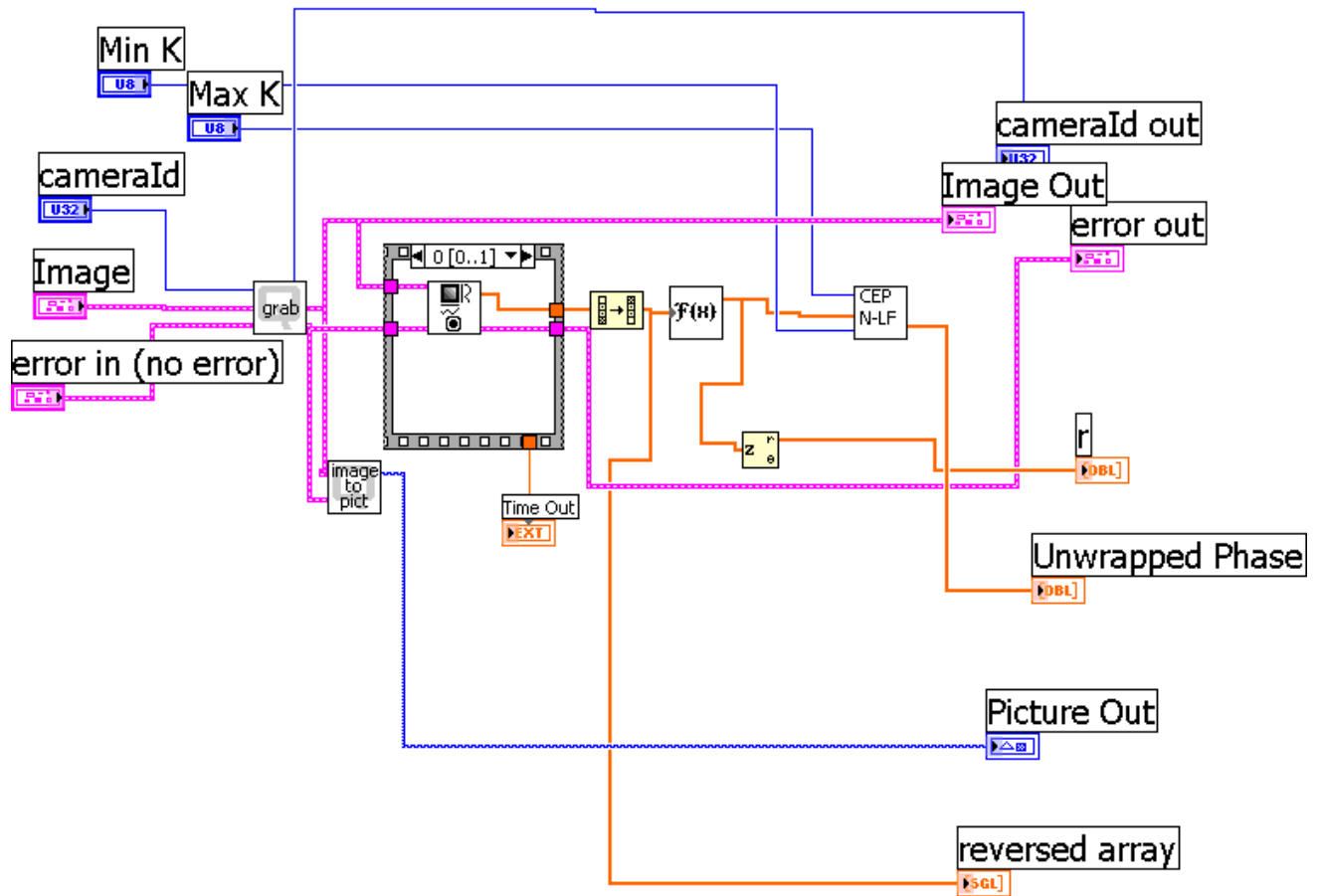


Figure A.1 Front Panel. 1) The fringe pattern, 2) the FFT peak obtained from the fringe pattern, 3) the range of integration of the fringe pattern and the integration time.

On the front panel, the fringe pattern obtained from the  $f$ -to- $2f$  is shown in the preview window, denoted by 1. A small, high contrast portion of the fringe pattern is selected by

adjusting the parameters at 3. The peak obtained from performing an FFT across the image lineout from 1 is shown at 2. The range of the peak is chosen.

The code performing that function is shown in the next figure.



**Figure A.2 Code for obtaining the FFT peak.**

In the code, an image of the fringe pattern is obtained and an average over the intensity at each pixel is taken, which gives a one dimensional average of the pixel intensity. The FFT of that one-dimensional average is taken and the amplitude is output to the front panel. The FFT is also sent to the CEP N-LF sub VI (virtual instrument). The sub VI selects the positive peak of the FFT and then performs the inverse FFT to retrieve the unwrapped CE phase. A portion of the code is shown in the next figure.

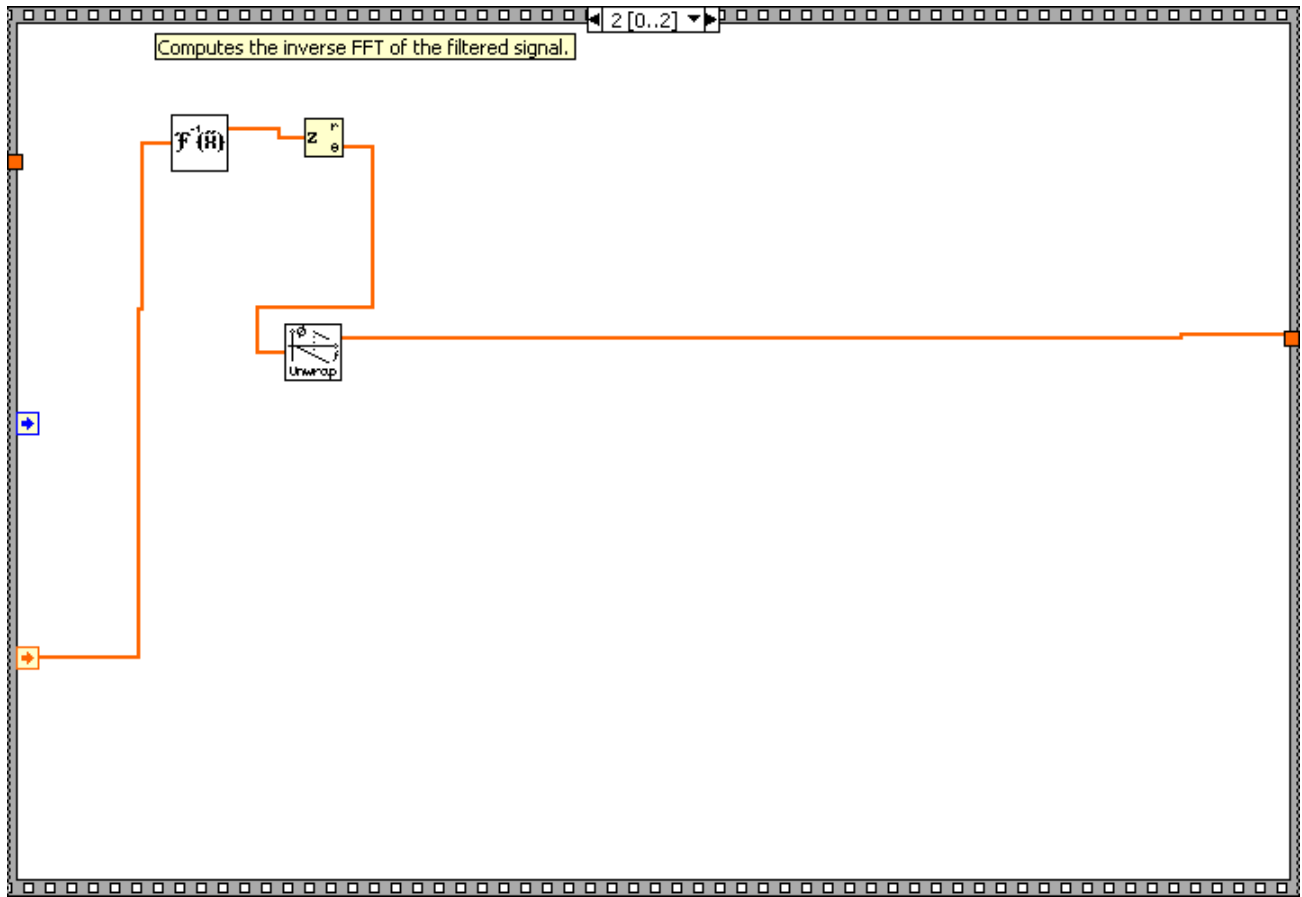


**Figure A.3 Sub VI for calculating the unwrapped CE phase.**

Once the unwrapped CE phase is obtained, the program begins to calculate the CE phase shift. The CE phase calculation is shown schematically in the following figure.

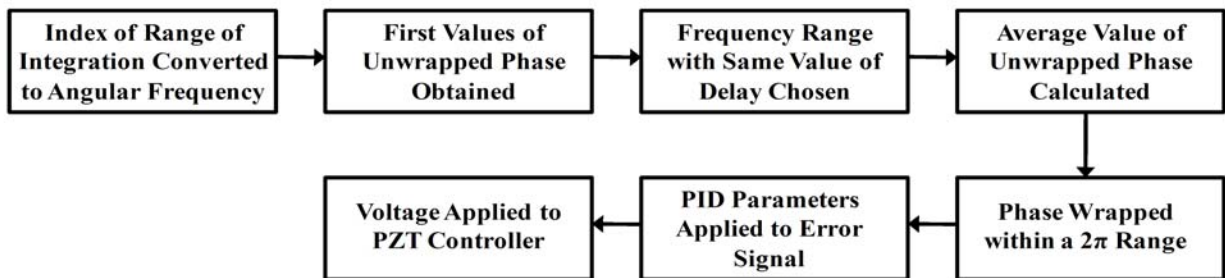


**Figure A.4 CE Phase code schematic.**

The user inputs the range over which the relative delay of the fringe pattern is zero. The code then computes the average value of the unwrapped phase over that frequency range. The

phase is then wrapped with  $2\pi$ . The PID parameters are chosen as to facilitate the best locking conditions. The error signal is derived from comparing the current phase to the previous phase calculated by the iteration. If the error is too large, then the PID code outputs a zero voltage. The control loop tries to make the CE phase shift zero. In the code, the D parameter is set to zero since the CE phase shifts quickly. Finally, a voltage is output by the program and sent to the PZT.

The CE phase program using the Ocean Optics spectrometer in the out-loop  $f$ -to- $2f$  follows the same basic format. The difference is in the collection of the spectra from the spectrometer.